Stony Brook University

Probing Topological Magnetism with Transmission Electron Microscopy

A Dissertation Presented

by

Shawn Pollard

to

The Graduate School

in Partial Fulfillment of the

Requirements

for the Degree of

Doctor of Philosophy

in

Physics

Stony Brook University

August 2015

Stony Brook University

The Graduate School

Shawn Pollard

We, the dissertation committee for the above candidate for the

Doctor of Philosophy degree, hereby recommend

acceptance of this dissertation.

Yimei Zhu – Dissertation Advisor
Senior Scientist, CMPMSD, Brookhaven National Laboratory
Adjunct Professor, Department of Physics and Astronomy

Matthew Dawber - Chairperson of Defense
Associate Professor, Department of Physics and Astronomy

Alan Calder
Associate Professor, Department of Physics and Astronomy

Elio Vescovo
Physicist, NSLS-II, Brookhaven National Laboratory

This dissertation is accepted by the Graduate School

Charles Taber
Dean of the Graduate School

Abstract of the Dissertation

Understanding Ordering and Dynamics of Topological Magnetism with Transmission Electron Microscopy

by

Shawn Pollard

Doctor of Philosophy

in

Physics

Stony Brook University

2015

With recent advances in phase imaging techniques and the development of new, novel specimen holders in which a variety of stimuli can be applied to magnetic samples in situ, the transmission electron microscope (TEM) has become a useful tool in studying the properties of magnetic materials at nanoscale. The resolution afforded by electron microscopy techniques allows for subtle changes to spin textures to be observed. Here, work on understanding the dynamic motion of spin-torque and magnetic field driven resonant vortex motion is presented, as well as experiments in regards to the role of defects in the ordering processes of artificial spin ices.

First, the role that defects and charge ordering play in the ordering processes in artificial spin ice lattices will be discussed. Experimentally, we find that reversal along the (11) symmetry axis results in local ground state ordering but long range frustration. Furthermore, defect interactions ultimately limit their maximum density within the lattice.

Next, while essential to understanding current driven domain wall motion, non-adiabatic spin-torque effects are poorly understood. In spin-torque driven magnetic vortices, subtle changes to the magnitude of the resonant orbits with varying chirality allow for the separation of adiabatic, non-adiabatic, and Oersted field contributions to the motion, as well as for the direct measurement of the non-adiabatic parameter with the greatest precision to date. Off-resonance effects are also probed for the first time. Additionally, despite field-driven dynamics of single vortices near equilibrium being well understood, far-from-equilibrium and coupled dynamics are significantly more complex, and due to experimental constraints, poorly understood. The dynamic response in both interlayer exchange coupled vortices in a stack geometry and direct exchange coupled vortices in a lateral geometry will be explored, and far-from-equilibrium results will be presented.

Table of Contents

Table of Figures

Acknowledgments

First, I would like to thank my advisor, Prof. Yimei Zhu, for his support and guidance during my graduate work. His passion for science and work ethic have helped to inspire my time here, and his tireless efforts towards supporting his research group made it possible to accomplish what I have. I would also like to acknowledge the support and guidance of all the current and former group members and scientists at Brookhaven National Laboratory that have supported me, taught me, and inspired me, including Dr. Dario Arena, Dr. Jing Tao, Dr. Lijun Wu, Dr. Myung-Geun Han, Dr. Steve Volkov, Dr. Qingping Meng, Dr. Binghui Ge, Dr. Zhen Wang, Joe Garlow, Lei Huang, and Tatiana Konstantinova. Furthermore, I am forever grateful to Kim Kisslinger, Dr. Fernando Camino, and Dr. Aaron Stein for their guidance in sample preparation methods. A special thank you goes to Dr. Javier Pulecio, who over the last four years has provided guidance and a helpful hand, in all aspects of work, and helping to keep me grounded. I would also like to acknowledge the US Department of Energy, Basic Energy Sciences, under Contract No. DE-AC02-98CH10886, for supporting this work.

I would also like to thank my classmates and friends who have lent me their support over the last seven years. A special mention must be given to Dr. Karin Gilje, Dr. Joshua Hignight, Dr. Betul Pamuk, Dr. John Elgin, Rahul Patel, Omer Rahman, Muhammed Yusuf, and Ashley Cohen, for not killing me during the years that they have lived with me.

Finally, but most importantly, I would not be where I am today without the trust, love, encouragement, and unconditional support of my mom, grandma, and brothers.

Publications

J. F. Pulecio, ***S.D. Pollard***, P. Warnicke, D. A. Arena, Y. Zhu, "Symmetry breaking of magnetic vortices before annihilation," *Applied Physics Letters* 105, 132402 (2014).

J. F. Pulecio, P. Warnicke, ***S. D. Pollard***, D. A. Arena, Y. Zhu, "Coherence and modality of driven interlayer coupled magnetic vortices," *Nature Communications* 5, 3760 (2014).

J. L. Hockel, ***S. D. Pollard***, K. P. Wetzlar, T. Wu, Y. Zhu, G. P. Carman, "Electrically controlled reversible and hysteretic domain wall evolution in nickel thin film/$Pb(Mg_{1/3}Nb_{2/3})O_3]_{0.68}$-$[PbTiO_3]_{0.32}$ (011) heterostructures observed by Lorentz TEM," *Applied Physics Letters* 102, 242901 (2013).

S. D. Pollard, M. Malac, M. Beleggia, Y. Zhu, M. Kawasaki, "Magnetic fields imaged using a Zernike-type phase plate in a TEM", *Applied Physics Letters* 102, 192401 (2013).

S. D. Pollard, Y. Zhu, "The Aharonov-Bohm effect, magnetic monopoles, and reversal in spin-ice lattices," *Microscopy* 62, S55-64 (2013), special issue: "Tribute to Akira Tonomura," T. Tanji, N. Osakabe, and T. Hirayama, *ed*.

S. D. Pollard, L. Huang, K. S. Buchanan, D. A. Arena, Y. Zhu, "Direct dynamic imaging of non-adiabatic spin torque effects," *Nature Communications* 3, 1028 (2012).

S. D. Pollard, V. Volkov, Y. Zhu, "Propogation of magnetic charge monopoles and Dirac flux strings in an artificial spin-ice lattice", *Physical Review B* 85, 180402(R) (2012).

Chapter 1. Introduction

1.1 Context of current work

With the observation of spin injection across the interface of a ferromagnetic and non-magnetic metal in 1985, and the discovery of a gigantic magneto-resistance (GMR) in multilayer magnetic structures by Fert [1] and Grünberg [2] in 1988, the field of spintronics was born. Spintronics, short for spin electronics, has seen rapid development as a research field due to both the intriguing fundamental phenomena that lies at the foundation of coupling between spin and electronic degrees of freedom in condensed matter systems as well as for its potential in overcoming significant technological hurdles in a variety of device systems ranging from magnetic logic and memory to sensors, antennae and more.

There has already been wide scale adoption of some spintronic technologies in the memory and logic sectors. Most of this is based on the GMR effect, which forms the basic operating principle in the standard magnetic based hard drive read head, and has allowed for the continuation of Moore's Law in the memory sector to this current day (Figure 1.1). Fert and Grünberg were recently awarded the Nobel Prize in physics for their seminal work in this area. Further developments have also led to GMR based logic devices that have recently seen commercial development, and signal processing and microwave frequency sources are currently under investigation. Interest in devices based on the magnetic properties of materials is driven by many factors ranging from radiation hardness, scalability, spectral purity, and the possibility of ultra-fast switching times and high densities in three dimensional architectures. However, new methods of controlling the local magnetic structure, essential to accessing the functionalities

of the previously listed devices, as well as methods to miniaturize the magnetic building blocks that form their basis, are needed in order to continue to increase device density without compromising stability or speed.

One avenue under current investigation as a solution to some of these issues is to design magnetic nanostructures in such a way that the competing energetics of the systems lead to new spin textures that allow for the ability to control their structure not only with magnetic fields, but also via the application of spin currents (either pure or charge-mediated). Furthermore, geometric control can lead to stability of magnetic structures far from equilibrium, increasing device reliability. The spin configuration of any magnetic structure is determined by the interplay of multiple energetic contributions. These include, and but are not limited to, the direct exchange interaction between neighboring atoms, the demagnetization energy associated with free charges at the boundaries of the sample, Zeeman energies from interactions with external fields, as well as spin-orbit effects such as magneto-crystalline anisotropy and anti-symmetric exchange interactions. For soft magnetic materials, in which there is no intrinsically preferred magnetization direction, at a remnant field, the dominant energies that determine the local magnetic structure are the demagnetization energies and exchange energies.

To minimize the existence of free edge charges in thin films, the magnetization tends to be confined to in-plane, although for large anisotropy materials or materials with perpendicular magnetic anisotropy, this may not be the case. When these thin films are further microstrucured (e.g. through lithographic techniques), small changes in shape can result in large changes to the magnetic structure. In order to minimize demagnetization energies, the sample will tend to break into various magnetic domains with spins at domain boundaries being at various angles while the exchange interaction tends to favor parallel alignment of neighboring spins. Because the

conditions for minimizing each of these energies are often mutually exclusive, they are termed as competing energies.

For certain geometries, the competing energetics result in novel spin configurations. Often, these spin textures can be described in terms of a topological charge, or quasiparticle, which is conserved and highly stable to energetic perturbations and can be quantified by the symmetry of the system. These charges, which include magnetic vortices, merons, and skyrmions, are now studied extensively due to their stability and intriguing dynamic properties, with topological magnetism being one of the most highly studied subfields of nanomagnetism at the current time. The magnetic vortex is described by both the circularity of the magnetization, which curls about a central point, as well as the direction of the magnetization at the central part of the vortex that cants out of plane [3]. These two independent degrees of freedom can be controlled via dynamic displacement, are stable to large perturbations, and may be densely packed with minimal crosstalk due to a lack of a generated stray field. For these reasons, they have generated interest as the basic building blocks of future logic devices as well as microwave frequency sources. The goal of this thesis is to better understand the role of magnetic quasiparticles, and the spin textures associated with them, in magnetic ordering as well as their dynamic properties while perturbed by excitations tuned to their resonance modes.

With these specific goals in mind, the transmission electron microscope (TEM) makes for an ideal tool to study such systems. While common techniques such as vibrating sample magnetometry (VSM) and measurements using superconducting quantum interference devices (SQUIDs) provide excellent quantitative information on the magnetization, they only give information of the weighted average of the magnetic distribution of either a large array of nanoscale magnetic elements or a single, large bulk sample. In nanostructures, changes in the

spin textures of interest due to external stimulus can be subtle, with effects that can be on the nanometer scale, beyond the scope of these measurements. Other techniques, based on direct imaging of the magnetic structure such as magnetic force microscopy (MFM) or photon based techniques such as MOKE microscopy or X-ray magnetic circular dichroism (XMCD) still lack the spatial resolution to probe the more subtle changes, although are much more local in scope than bulk measurements. TEM, however, is unique in that it may afford magnetic spatial resolution below 5 nm, with new techniques pushing ever closer to single nanometer precision. Beyond the spatial resolution afforded to magnetic imaging, the real space resolution has been pushed to below the angstrom scale, allowing for imaging of individual atomic locations within a system, and the ability to link magnetic behavior to that of local structural defects at the atomic scale. Furthermore, diffraction techniques allow for structural characterization while chemical mapping capabilities of techniques such as electron energy loss spectroscopy (EELS) and energy dispersive X-ray spectroscopy (EDX) allow for the elemental composition to be probed. The combination of these techniques allows for magnetic properties to be directly linked to the local micro- and nanostructure.

Finally, the modern TEM also can function as a workhorse machine where a variety of stimuli may be applied *in situ* by appropriate use of various sample holders. Among current capabilities, temperature gradients, electric currents, magnetic fields, strain, and photonic excitations may all be applied to the specimen region. Combined with modern fabrication techniques, many of these stimuli may be controlled at the single micron scale, allowing TEM to probe very local properties, in real space, in combination with electrical or other characterization methods. All of these capabilities make the TEM a full research platform where structure-

property measurements can be studied near the atomic scale in real time and, as such, is ideal for the systems studied in this work.

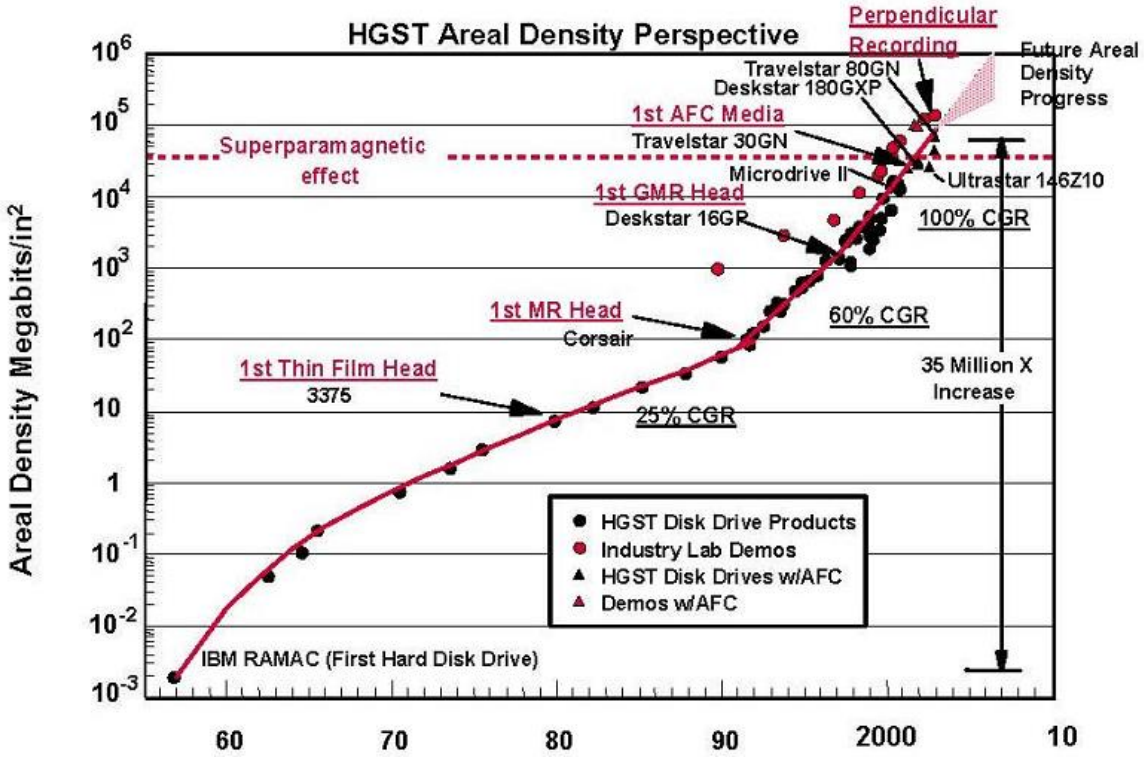

Figure 1.1 - Areal density as a function of year in commercial hard disc drives. The first GMR head was introduced in the late 1990's, and has allowed for the large increases in area density that we have seen to this day. CGR stands for compounded growth rate.

1.2 Outline of this dissertation

This dissertation is structured as follows.

Chapter 2 introduces the general experimental and theoretical methods used in the majority of the work shown in this dissertation. First, the basics of TEM instrumentation and magnetic imaging are discussed, including the fundamental principles of Lorentz imaging, the transport of intensity approach for phase retrieval, and magnetic imaging through the use of phase plates. Further discussion covers the sample preparation methods used, including electron beam evaporation and electron beam lithography. Finally, an overview of magnetism and the theory of micromagnetism are introduced, including discussion of relevant energies associated with magnetic ordering and the Landau-Lifshitz-Gilbert equations.

Chapter 3 covers studies on the ordering governing the reversal process in an artificial square spin ice lattice. In this system, a large array of nanoscale magnetic islands are arranged such that frustration effects arise, and defect nucleation, propagation, and mutual interactions are shown to play a dominant role in the reversal. Using a combination of imaging techniques as well as numerical modelling of the system, we show how these interactions place limits on defect densities and result in a state with short range ordering, but frustrated long-range ordering.

Chapter 4 focuses on the in-plane gyrotropic mode of a magnetic vortex excited by a spin polarized current. Specifically, this section shows the effect of this current on the properties of the vortex motion and the variations that are dependent on the circularity of the magnetization. These variations are subtle, and electron microscopy is used to determine off-resonance effects for the first time and compare with pre-existing analytical models. Furthermore, using differences in orbit trajectories, we measure the heavily debated non-adiabatic spin torque

parameter with the greatest precision to date, which further provides clues to the origin of non-adiabatic effects associated with spin excitations driven by spin polarized currents.

Chapter 5 presents measurements on the effect of modifications to the local confining potential in exchange coupled multi-vortex systems. In this section, the separation between two vortices of opposite circularity is modified by application of an in-situ DC magnetic field, while simultaneously excited at its resonant frequency by an AC magnetic field. The vortex motion is divided into two regimes, one in which the vortex response to the DC field is linear, as well as a non-linear regime. It is found that a sharp potential exists at the boundary between these regimes, causing large distortions in the resonant vortex orbit. Beyond the linear field, the interactions lead to two degenerate ground states, and the vortex can be driven between them through application of a resonant current. This allows for amplification of the vortex orbit along the direction parallel to the DC field.

Finally, chapter 6 concludes the dissertation. In this section, the outlook and future directions for the manipulation of magnetic quasiparticles and spin textures are discussed, as well as new applications that are in their infancy. The current limitations of TEM for magnetic imaging and the ongoing efforts to push beyond these limitations are also discussed.

Chapter 2. Experimental and theoretical methods

2.1 Basics of TEM

In a Transmission Electron Microscope (TEM), images are formed as a result of the modified wave function of incident high velocity electrons transmitted through a thin sample. The electrons are provided by an electron gun, which is composed of a biasing circuit, a Wehnelt cap, an extraction anode, and a filament which serves as the source of electrons. Typical filaments currently used are typically thermal (LaB6 or Tungsten), in which a filament is resistively heated to the point where electrons are no longer bound to the surface of the material, or field emission, in which a strong electric field is applied to a near point source, creating a potential well for electrons to tunnel through (Fowler-Nordheim tunneling). From this latter method, a highly coherent electron beam may be produced.

The electrons are then accelerated in a multi-stage process to a final relativistic energy of typically a few hundred keV. The ultimate value will depend on the specifics of the microscope and the goal of the experiment. The electron beam is then shaped by series of lenses and apertures. A condenser lens and aperture, placed above the sample, define the illuminated area and limits the beam current, as well as attenuates high angle incident electrons.

The sample is inserted into the beam column using a specimen holder suited to the desired experiment. A variety of sample holders are commercially available. Uses range from standard holders, which allow for tilt along one or two axes, as well as holders allowing for *in situ* measurements of electrical properties, photonic excitations, heating, and cooling. In order for the sample to be viewed in TEM, it must be electron transparent, and as such is limited in

thickness to approximately 200nm, although this will vary from material to material. The higher the atomic number of the sample element, the greater the electron beam attenuation. The planar dimensions of the sample also must fit into the column, and are limited to approximately 3mm. The holder is loaded into the column through a vacuum sealed load lock and controlled electronically through the use of a high precision goniometer. This is used to align the sample to a suitable imaging condition, as well as move the desired area of the specimen into the beam area. The goniometer allows for the sample to be moved along all three axes, as well as for tilt along the x-axis. The maximum tilt is limited by the pole piece of the microscope, but is typically between 20-40 degrees.

Further lensing is performed by the objective lens. This is the closest lens to the specimen. Due to small separation between the objective lens and specimen, it is common for a 2T or higher magnetic field out of the sample plane to be present in the sample area, making it poorly suited for magnetic imaging as it will strongly effect the magnetic configuration of any material. For this reason, many microscopes dedicated to magnetic imaging will make use of a Lorentz lens. Although it has a much more limited resolution than a fully excited objective lens, only a small magnetic field will be present in the specimen area, while still being capable of magnification of a few thousand times. The details of magnetic imaging using this lens will be discussed in further sections. Furthermore, another approach, implemented at BNL, was to design a long focal length microscope, in which the separation of the sample and the objective lens is increased by modifying the pole piece in order to remove it from the strong field. While resolution is not as good as in a typical TEM with a fully excited objective lens, it still is about two orders of magnitude larger than that of a typical Lorentz lens. The remaining lenses (intermediate and projector) serve to further increase the magnification of the image. Images are

typically captured with charge-couple devices (CCDs), as opposed to the previous photographic image plates, and can be used for fast quantitative analysis. The schematic lens diagram of a JEOL-2100F TEM, similar to the microscope used in this thesis, is shown in figure 2.1. Figure 2.2 shows both a typical objective pole piece taken from a JEOL-3000F TEM as well as the modified pole piece from the JEOL-2100F Lorentz TEM at BNL.

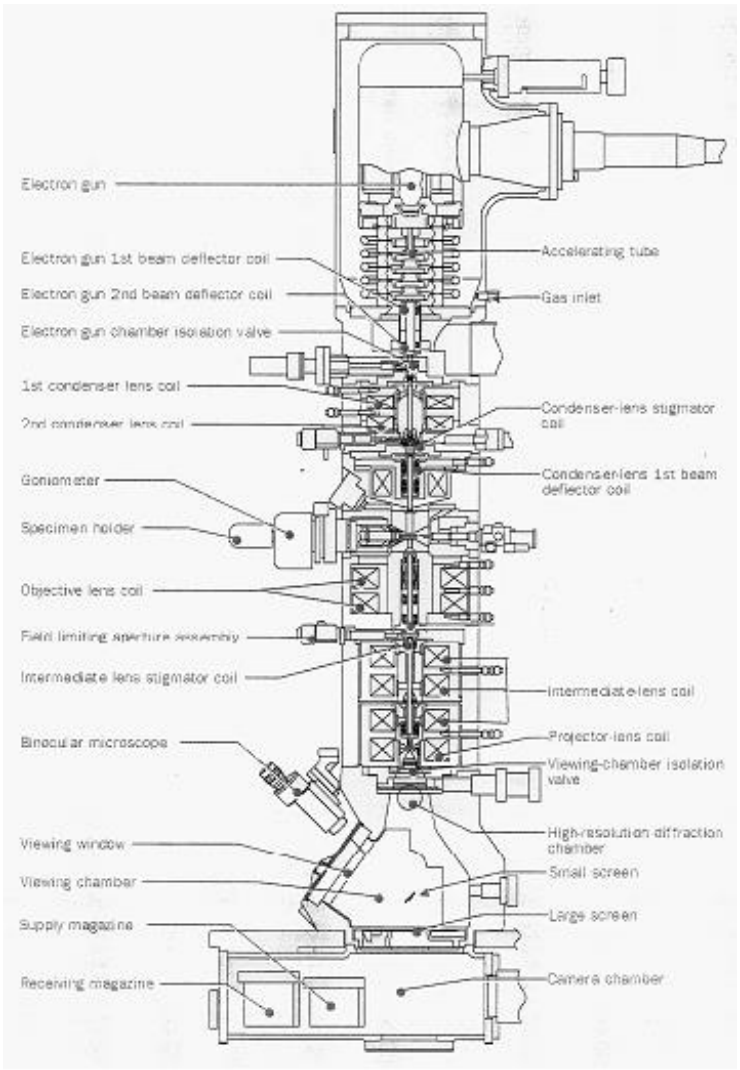

Figure 2.1 - Schematic overview of a JEOL 2100F TEM, showing the general location of the various lenses and apertures composing a typical TEM.

Figure 2.2 - Photographs of the objective pole pieces of a JEOL 3000F and JEOL 2100F Lorentz TEM. The 3000F consists of a symmetric pole piece design with a small gap, while the 2100F Lorentz TEM is composed of a mu-metal cage with a side entry port, creating a near field free specimen region.

2.2 TEM based magnetic imaging techniques

In a TEM, only the intensity (amplitude squared) of the transmitted electron wave function incident on a CCD is recorded. However, an electron wave contains both an amplitude and a phase, described by their quantum mechanical wave function. From the Aharanov-Bohm equation, an electron passing through an electric or magnetic field undergoes a phase shift relative to a reference wave that is passed through vacuum and hence does not experience a phase shift. The phase shift experienced by the electron wave passing through the sample is given by

$$\Delta\phi = C_e \int V dz - \frac{2\pi e}{h} \oint B dS \,, \qquad (2\text{-}1)$$

where C_e is a constant that is related to the energy of the incident electron, V is the electronic potential of the material, e and h are the usual fundamental constants, and B is the local magnetic field [4].

Under conventional TEM imaging conditions, magnetic structure is not readily visible due to the high out of plane field that tends to saturate magnetization along the beam direction. Contrast due to the phase shift of the electron beam only results from magnetization perpendicular to the beam direction and therefore magnetic imaging is typically done without the objective lens on, or only weakly excited. This limits the highest attainable resolution of the microscope, but since changes in magnetization typically occur over larger than single nanometer length scales, this does not pose a significant issue for most measurements in the modern TEM. The specific methods of magnetic imaging will be discussed below.

2.2.1 Lorentz microscopy

Lorentz microscopy, while not quantitative in terms of measuring phase shift, is the simplest method of magnetic domain imaging available in TEM [5,6]. The contrast mechanism is typically naively explained as the classical deflection of electrons resulting from a Lorentz force. In this model, electrons passing through a magnetic sample are deflected with the angle of deflection determined by the strength and direction of the magnetization within the sample. At areas where the magnetization changes, such as at domain walls or sample edges, this deflection leads to either enhanced or decreased contrast (Figure 2.3). However, this naïve model does not tell the entire picture, as the true nature of the effect is quantum mechanical in origin, and is fully described by the phase shift induced on the electron wave function by the magnetization. The full treatment requires this to be taken into account.

Most often Lorentz microscopy is performed in the Fresnel mode. By under- or over-focusing the beam, a higher or lower intensity will occur owing to the converging or diverging beams, respectively. In Fresnel imaging, it is the change in the magnetic induction that is measured, not the magnetic induction itself, and therefore contrast is only obtained at areas where the magnetization varies rapidly (i.e. at a domain wall). Furthermore, the defocus used to obtain a Fresnel image adds to delocalization of the beam, obscuring detail at the nanoscale (i.e. individual grains or other microstructure), and limiting the use as a quantitative tool. Other, more quantitative techniques such as electron holography, transport of intensity, and hole-free phase plate imaging do not have this limitation, but are experimentally much more difficult. The following sections will discuss both the transport of intensity approach and hole-free phase plate imaging.

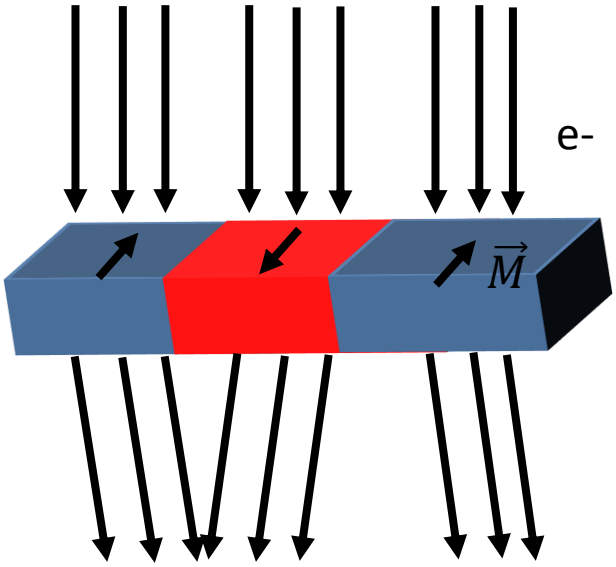

Figure 2.3 - A naïve illustration of the image formation process in Lorentz imaging. The charged electron beam is deflected by a Lorentz force when passing through a magnetic material. At domain boundaries, this leads to enhanced or decreased contrast, depending on the relative alignment of the domains and the defocus condition.

2.2.2 Transport of intensity

The transport of intensity (TIE) approach is based on the conservation of electron flux within the electron beam, and is typically performed by aligning two images of the same area at two defocuses, with a third, in-focus image used as a reference to normalize intensity. From the change in intensity between the images, it is possible to reconstruct a phase map of the sample. The continuity equation for a paraxial beam may be written as:

$$\nabla_{\perp}[\mathrm{I_n}\,\nabla_{\perp}\varphi_{\mathrm{n}}] = -k_z\frac{dI}{dz} = -\frac{k_z(I_n - I_o)}{dz}, \qquad (2\text{-}2)$$

where k_z is a scaling constant related to the electron wavelength by $k_z = \frac{2\pi}{\lambda}$, dz is equal to the defocus, and dI is the change in intensity [7]. I_n refers to the intensity of the defocused image, while I_o refers to the infocus, or object, image. It is apparent that if these values are known, the

phase shift can be determined. Figure 2.4 shows a sample phase reconstructed image of a continuous 40nm thick cobalt thin film.

Limiting the utility of the TIE technique is the difficulty associated with the alignment of the microscope, as single pixel misalignments between the necessary images can lead to significant artifacts that can appear as contrast resulting from non-existent magnetic fields, making this technique challenging from a technical standpoint. Part of this results from changes in the beam condition resulting from the change of defocus. Furthermore, depending on the reconstruction process, artifacts can emerge that make interpretation difficult. A recently developed technique based on the TIE method, known as differential TIE (D-TIE) can overcome some of these issues in which the information of interest is not the magnetic phase information itself, but instead the relative phase difference between two magnetic states [8].

With D-TIE, the change in flux between two images taken at the same defocus is measured after some stimulus has been applied to the system. This can be seen as follows - if we have two images taken at the same defocus in different magnetic states a and b, with intensities I_a and I_b, the continuity equation for each can be written as previously for each. For small dz, $I \gg dI$, and subtracting the continuity equations for the images taken with different magnetic states results in:

$$\nabla_{\perp}[\mathrm{I_n}\,\nabla_{\perp}(\varphi_{\mathrm{a}} - \varphi_{\mathrm{b}})] = -\frac{k_z(I_a - I_b)}{dz}. \qquad (2\text{-}3)$$

Therefore D-TIE links the relative phase shift between the two magnetic states to the differences in the images taken at the same defocus. This allows for the quantification and visualization of the difference in magnetic flux between two states, and only requires two images at the same focus condition - one reference and one after some stimulus has been applied.

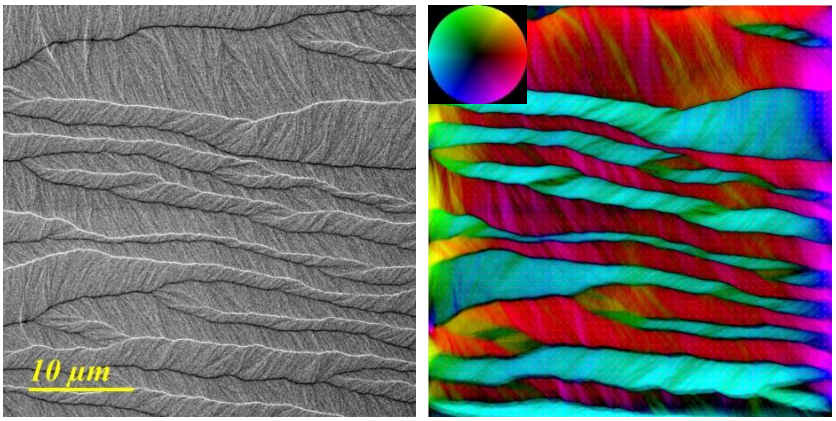

Figure 2.4 - Left: Typical underfocused Lorentz image of a 40nm cobalt thin film showing magnetic domain walls and magnetic ripple contrast. Right: TIE phase reconstructed image of the same region. The color corresponds to the direction and magnitude of the magnetization, as indicated by the color wheel in the upper left corner.

2.2.3 Magnetic imaging with a hole-free carbon phase plate

The use of a hole-free carbon phase plate (HFCPP) for magnetic imaging has only recently been developed at Brookhaven National Laboratory. Previously, phase plates have been used primarily to increase phase contrast resulting from variations in the electrostatic potential in beam sensitive samples [9]. Through the use of a phase plate, it is possible to obtain significant contrast with low beam doses, important for many biological samples as well as some thin film samples that can be quickly damaged by the electrons involved in the imaging process [10]. While similar effects can be achieved with defocused images, this results in distortions and loss of nanoscale structural information.

We have shown that it is also experimentally possible to use a HFCPP to image local magnetic ordering in both the bulk of a magnetic sample as well as stray magnetic fields in vacuum for the first time [11]. In order to compare the resulting contrast obtained via in-focus imaging with a HFCPP and the standard defocused Lorentz imaging, we modified a JEOL

2100F-LM TEM by mounting a 10nm thick carbon film in the back focal plane of the objective lens. The electron beam introduces a local electronic potential, and hence a phase shift in the electron beam that is spatially varying and is dependent on the beam profile. While this phase shift is unable to be quantitatively determined, its convolution with a phase shift due to the sample results in phase contrast, and can be used to obtain qualitative information on the local magnetic potential. A reference sample of $(Pr,Dy)_2Fe_{14}B$, a hard magnet with Ms = 1.4T exhibiting a magnetic stripe domain configuration, was used during initial testing.

Figure 2.5 shows both (a) Fresnel and (b) HFCPP images of the $(Pr,Dy)_2Fe_{14}B$ in a wedge geometry with an approximately 11 degree apex angle, determined via the contrast variations in the bright field image shown in the inset of figure 2.4b. Line scans from various identified sections of the sample are also shown to compare the contrast generated by the HFCPP and Fresnel image. In the HFCPP, as opposed to the Fresnel image, contrast varies considerably depending on the distance from vacuum, and this behavior is compared to simulated HFCPP intensities in Fig 2.6. Contrast variations in the HFCPP image coincide with the locations of domain walls in the Fresnel image, and thickness effects lead to an additional spread of the domain contrast in the HFCPP. Additionally, the HFCPP shows clear edge contrast as well as contrast variations in vacuum. These are identified as the result of fringing demagnetization fields present at the sample boundary. While direct measurement of the phase shift generated by the magnetic field is unable to be determined quantitatively using the HFCPP scheme, it is apparent that this method is promising for enhancing magnetic contrast at domain walls without the delocalization associated with Fresnel imaging, and merits further consideration as an imaging technique.

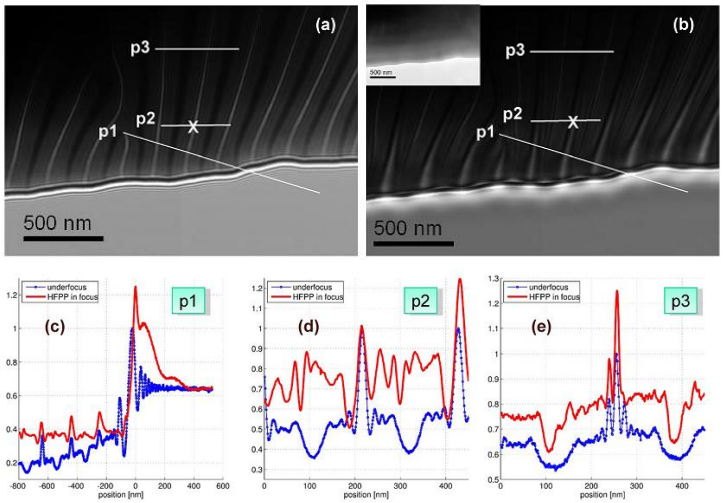

Figure 2.5 - Phase contrast images of the $(Pr,Dy)_2Fe_{14}B$ used as a test sample. (a) Fresnel image taken at approximately 120μm underfocus. (b) Infocus HFCPP image of the same area showing identical domain locations as well as contrast in vacuum, a result of the phase shift induced by the fringing magnetic field near the sample edge. The inset shows the same area with no phase plate inserted. (c-e) Normalized line profiles taken at the positions marked in (a,b). An offset of 0.25 is added for clarity. Reprinted with permission from Appl. Phys Lett. 102, 192401 (2013). Copyright 2013, AIP Publishing LLC.

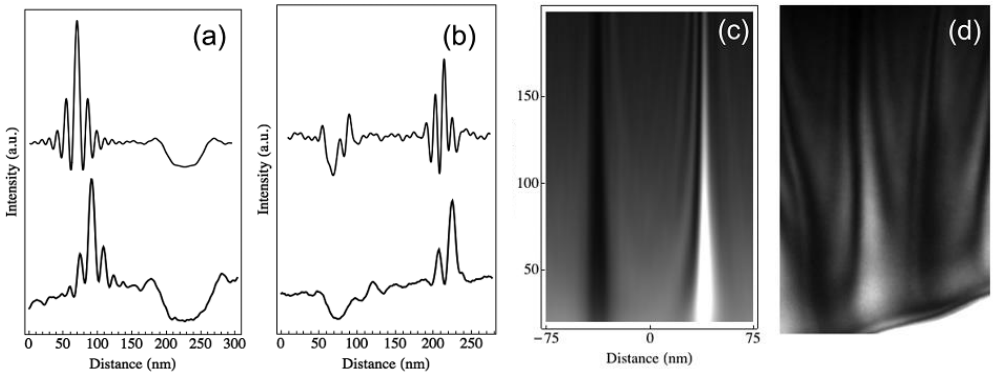

Figure 2.6 - Left: Comparison between experimental (upper) and simulated (lower) intensity profiles taken about 800nm from the sample edge, where the thickness is approximately 200nm thick, for Fresnel (a) and HFCPP images. Right: (c) Intensity profile for a simulated HFCPP charge profile corresponding to a constant $\frac{\pi}{10}$ phase shift for different thicknesses. (d) Experimental results for a sloped $(Pr,Dy)_2Fe_{14}B$ sample showing qualitatively similar contrast as the simulated profile, including more diffuse contrast for lower thicknesses near the sample edge. Reprinted with permission from Appl. Phys Lett. 102, 192401 (2013). Copyright 2013, AIP Publishing LLC.

2.2.4 Application of magnetic fields and spin excitations in TEM

To truly study spin textures within the TEM, it is necessary to have the ability to apply a controllable field within the specimen area. Due to the geometry of most thin film samples and the relevant energies which will be discussed further on, an in-plane field is of particular importance. The methods used in this dissertation are discussed here.

Most commonly, when fields on the order of 100 Oe or more are necessary, the field generated through weak excitation of microscope's objective lens. In a typical electron microscope, the objective lens generates a field of around 20 kOe in the specimen area directed along the vertical axis of the microscope column and perpendicular to the sample plane. For typical magnetic imaging, it is desirable to minimize this field to prevent them from causing undesirable changes to the magnetic structure, and hence a low-field Lorentz lens is commonly used for low field applications. However, by weakly exciting the objective lens that generates a calibrated field and tilting the sample in the out-of-plane field, it is simple to generate a controllable in plane field. As long as the objective excitation is well below the threshold required to tilt the magnetization of the sample out-of-plane, in plane fields of more than 1 kOe may be applied to the specimen. The magnitude of in-plane field is typically set by using a fixed objective lens excitation and changing the tilt of the specimen holder, which can be accurately controlled to within 0.1 degrees up to a maximum angle of approximately 20 degrees. For the work done in this thesis in which fields greater than 100 Oe were necessary, we utilized a JEOL-3000F TEM with a calibrated magnetic field [12]. Calibration was performed by inserting a hall probe on the end of a TEM specimen holder and measuring the magnetic field as the objective lens current was varied. This information is shown in figure 2.7.

Another method, when small fields are all that is required, is to place the element of interest on the surface of a thin (<50 nm thick), electron transparent stripline. By applying a known current through the wire, it is possible to generate a well-defined magnetic field in the plane of the sample without a residual out-of-plane field. These fields are typically limited to < 10 Oe, and therefore are only useful when small fields are necessary. However, for resonant excitations, only a few Oe are necessary to generate large changes in the magnetic structure as any effect is amplified near resonance frequency, and this makes for an ideal method in cases where resonance phenomena is being studied.

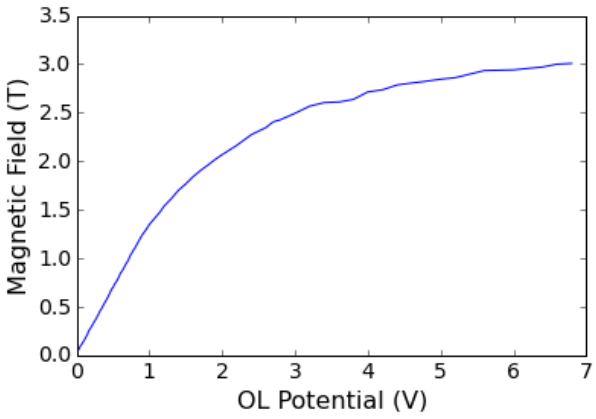

Figure 2.7 - Magnetic field calibration curve for the JEOL 3000F microscope at Brookhaven National Laboratory.

2.3 Sample preparation

2.3.1 Sample requirements

For quality imaging within TEM, stringent sample specifications must be met, and this is one of the primary drawbacks of the use of TEM as a research instrument. Limitations on the planar size of a sample are usually restricted to less than 3mm in order to fit on the endpiece of a typical sample holder, although various methods can be used to slightly increase this size. The sample also must be electron transparent. While the total thickness depends on the Z-number of the material under consideration, a general rule of thumb is that the thickness should be less than 100nm, but in some cases can be extended to 200nm or more, depending on the material and accelerating voltage of the microscope. Furthermore, the sample must be stable under electron beam irradiation (i.e. without charging or de-gassing).

For the work shown in the following sections, commercially available silicon nitride (Si_3N_4) self-supporting membranes were used as substrates during sample preparation (figure 2.8). These membranes consist of a 0.5mm x 0.5mm electron transparent square window of silicon nitride, surrounded by a 200μm thick silicon frame for support. The windows themselves are square, with dimensions of 3mm x 3mm, designed to fit in a standard TEM specimen holder. The window is flat (variations of less than 50pm out-of-plane), low stress, and robust against mechanical and thermal stresses. The thickness of the electron transparent region can be varied, with typical commercially available thicknesses of 50nm, 100nm, and 200nm. Due to the low average Z-number of Si_3N_4, despite its thickness, the window itself results in only limited attenuation of the electron beam.

There are, however, several limitations to the silicon nitride membranes. First, while thin, the thickness of the silicon nitride does attenuate the electron beam. This is more noticeable for thick windows, and the reason why 200nm thick windows are rarely used. A primary concern when using Si_3N_4 membranes is charging. Silicon nitride is a highly insulating material, and hence electrons from the beam may accumulate on the window. The resulting charge will then cause deflections and instabilities of the beam, and may cause changes to the material being studied. In some cases, this may limit or even prevent proper images from being obtained. To remedy this situation, it is common practice to coat the membrane with a thin (< 5nm) conductive layer, usually a low atomic weight material such as carbon or chromium. In order to prevent unwanted effects from this coating layer (such as shorting of electrodes on the top surface or interactions with the material being studied), this is usually done on the reverse side of the window.

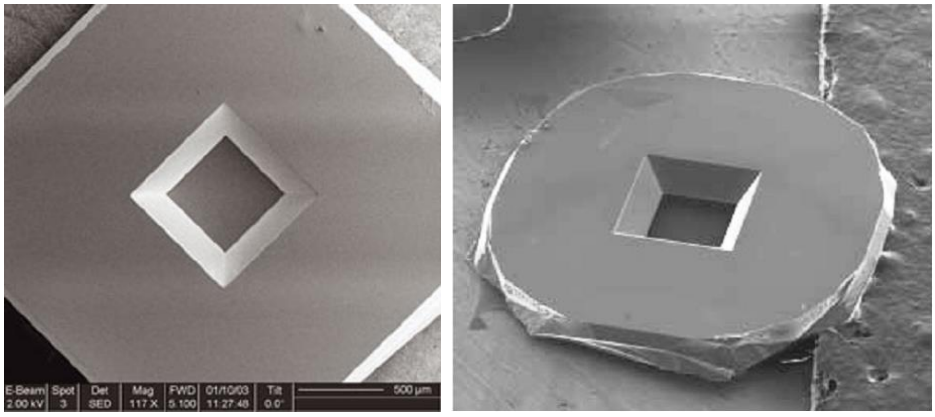

Figure 2.8 - SEM micrographs showing a typical Si_3N_4 TEM window. The center area is etched to approximately 100nm thickness in order to ensure good transmission of electron beam.

2.3.2 Thin film deposition

Many different methods exist in which to create a thin film TEM sample. For the experiments detailed in this thesis, we utilized a home-made ultra-high vacuum (UHV) electron beam evaporator (Figure 2.9). The evaporator is a dual gun (3kW), six target (3x2) co-evaporation system, such that two source materials may be deposited simultaneously. The vacuum system consists of two main sections, a medium vacuum sample load lock, and the primary UHV evaporation chamber.

The load lock consists of a small volume for rapid pumping speeds, isolated by a valve from the main chamber. The sample arm, used to move the sample between load lock and main chamber, when retracted, is easily accessible from a simple window which is clamped shut then vacuum sealed while pumping is in process. The load lock vacuum is achieved through a two stage pumping process, with a dry roughing pump providing vacuum up to 10^{-3} torr, and a turbo-molecular pump that can be used to achieve vacuum of 10^{-7} torr. Before opening the valve to the main chamber, the load lock is typically in the 10^{-6}-10^{-7} vacuum range.

The main chamber is pumped by a large ion pump, and further reduction in pressure can be obtained through utilization of a titanium sublimation pump within the main chamber. A cold trap is also available. Typical base pressure prior to evaporation processes is in the low 10^{-9} torr range. Residual trace gases may be monitored via a residual gas analyzer. Within the chamber there are also two quartz crystal thickness monitors, one for two rows of deposition material sources. The sample holder within the main chamber can also be heated in excess of 1100ºC in order to control the crystallinity of thin film materials, and is also used for post-evaporation annealing.

The electron gun system consists of two 3kW guns, each with three crucible targets. Permanent magnets are used to shape and direct the beam path, which directs the beam into the

general vicinity of the crucible targets. For fine control of the beam, the x and y position, as well as the size of the beam raster is controlled by a Thermionics 100-0030 beam sweep. Both guns operate at 4kV, and the current can be varied from 0-200mA. Typical currents used ranged from <10 mA for Cr, to 180mA for Au, although this varies depending on the amount of material in the crucible, the crucible material, and the amount of thermal contact between the crucible and the crucible holder, as well as the desired evaporation rate. Depending on desired thickness and film quality, evaporation rates ranged from between 0.05Å/s for thin Cu layers to 0.3 Å/s for Au electrodes.

While evaporating, the electron gun's tungsten filament is heated such that it begins to thermionically emit electrons. The beam is accelerated at 4kV and deflected towards the target by the magnetic field near the filament. Further shaping and directing of the beam is done using the beam sweep. The impact of the high velocity electrons results in local heating of the target. For large enough currents, a gas is generated which then solidifies on the substrate. The beam sweep amplitude can be used to spread or shrink the beam, and either a higher current density at a point on the target, or a more uniform heat distribution can be used. In most cases, a large beam spread is desired, as this allows for more uniform evaporation of the target and results in less wasted material. The target sources are contained within graphite, metallic, or intermetallic crucibles, which are then cooled via chilled water lines to prevent evaporation and mixing of the source and crucible. A schematic of the process is shown in figure 2.10.

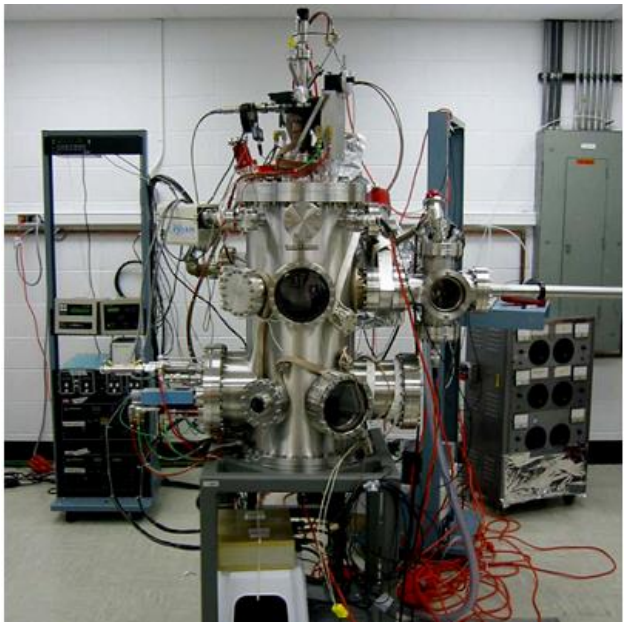

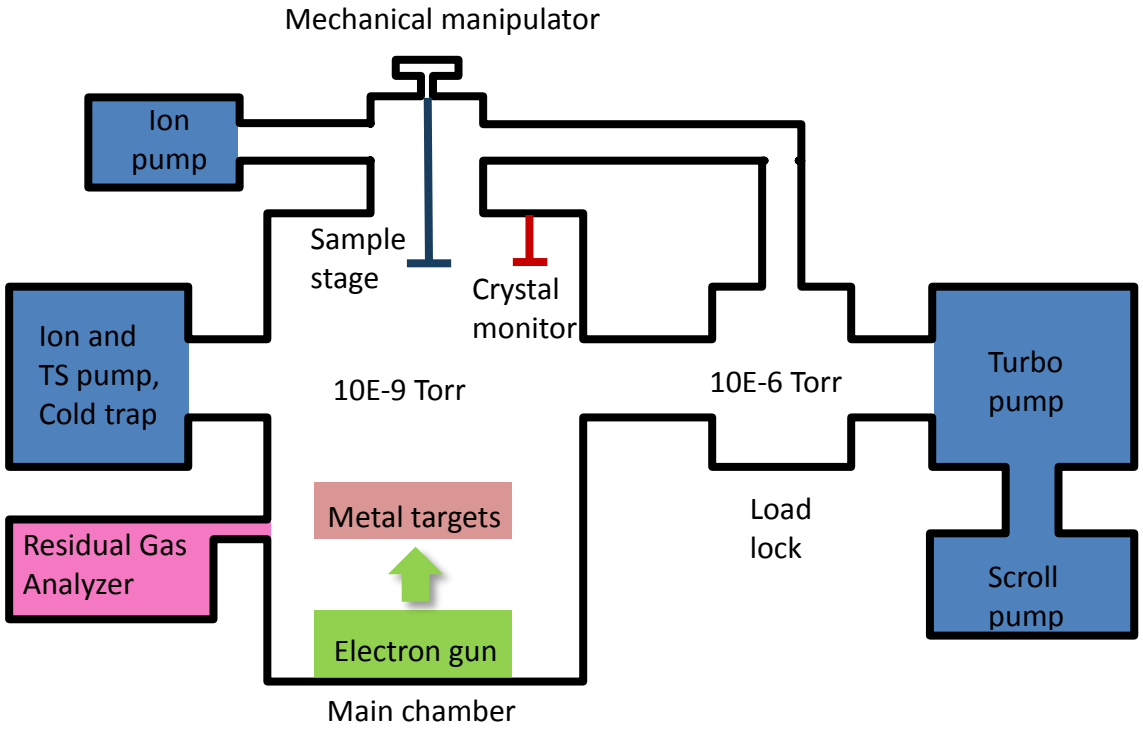

Figure 2.9 - Top: Image of the evaporation chamber. Bottom: Schematic diagram of the electron beam evaporation system showing the pumping system and system logic.

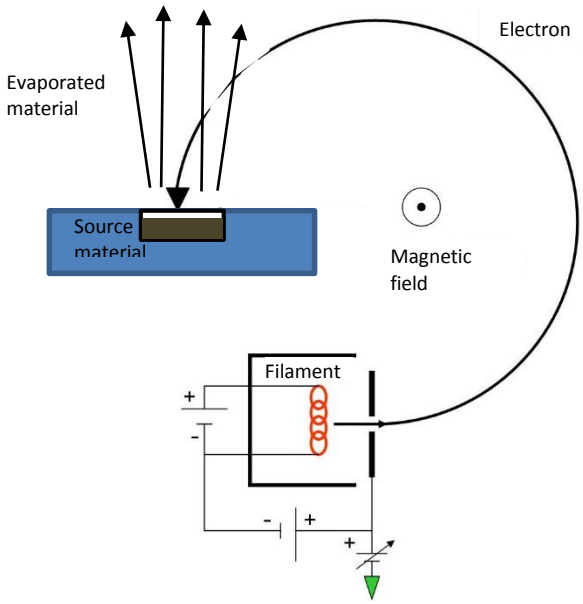

Figure 2.10 - Schematic of the evaporation process in a standard electron beam evaporation system.

2.3.3 Electron beam lithography

In many situations, more is needed than just the deposition of an unstructured thin film. One typical method used in order to create structure out with an evaporated material is lithography [13]. While masks can be used for many applications, and are ideal for high throughput processes, in many situations the minimum feature size is too large, and edges typically lack sharp definition. To overcome these limitations, we utilize lithographic processes, which has the added bonus of allowing for simple modification of desired designs. Lithography techniques can generally be broken into two categories – additive and subtractive lithography. In additive processes, lithography is used to define a pattern in a resist that has been spun onto a substrate. After film is deposited, the resist is lifted off, leaving only the areas exposed by the lithographic process. In subtractive techniques, a film is deposited, and then resist added,

followed by an etching process to transfer the pattern to the film. While many different lithographic techniques exist, including photo-lithography, the resolution needed for sub-micron scale patterning is typically done through electron beam (e-beam) lithography, and that is the method used in this dissertation. An additive technique is used due to its simplicity. As less steps are necessary, and the Si_3N_4 viewing window is fragile, this reduces the risk of breaking the membrane when compared to subtractive techniques. Lithography work shown in this dissertation was carried out using the facilities at the Center for Functional Nanomaterials, at Brookhaven National Laboratory.

In e-beam lithography, it is necessary for the resist to be sensitive to the electron beam. Typical resists consist of a polymer in a solvent. The resist is transferred to the sample area, which must be flat, using a pipette. The solvent is then spun at high speed in order to create a uniform coating. The spun resist is baked to evaporate the solvent material, leaving the polymer layer. When exposed to the electron beam, the bonds of the polymer resist are broken, leaving lower molecular weight pieces. With the appropriate solvent developer, only these lower molecular weight polymer fragments can be washed away, leaving the remaining mask of resist. Following deposition of material, another solvent is used to remove the remaining resist as well as deposited material on the remaining resist, leaving only material on the substrate in the designated pattern. The details of the specific steps used in our fabrication process are given below. A schematic overview of the entire process is given in figure 2.11.

First, a layer of resist is spread on a silicon piece. This piece serves as the base for the silicon nitride window. The silicon nitride is placed on this silicon, and then heated to 110ºC. The resist, in this case, acts to glue the window to the base silicon layer. Resist is then spin coated onto the silicon nitride window. Usually a bi-layer resist is used. First, copolymer

methyl methacrylate (MMA, 9% solids) in ethyl lactate is spun at 3000 rpm for 30s. This layer is then baked at 180ºC for 90s to remove the solvent material. Then polymethyl methacrylate (PMMA, 950 k molecular weight, 4% solids) in chlorobenzene is spun at 3000 rpm for 90s. This is then also baked at 180ºC for 90s. While a single PMMA layer is commonly used in e-beam lithography processes, a bi-layer facilitates the final lift-off process, and can be used to improve device yield, although it has the drawback of ultimately limiting lateral resolution. Because MMA has a higher sensitivity to the e-beam than the PMMA layer, it will be overexposed and forms a wider mask than the PMMA layer. This forms what is known as an undercut profile. After deposition, the narrower PMMA layer defines the mask, while the MMA layer is not in contact with the deposited material, allowing a greater interaction area for the final solvent, hence increasing the success rate of the lift-off.

Now the sample is ready for patterning. The pattern for lithographic writing is designed using DesignCAD, a commercially available computer aided vector drawing program. This is done by specifying the size, and shape of either predesigned common structures (circles, rectangles, arcs), or by drawing a custom figure of arbitrary shape. Structures that will be exposed to different electron beam currents or with different alignment magnifications are given different layers. The file is saved in a format accessible by an interfacing program called Nanometer Pattern Generation System (NPGS). This program controls the electron beam in writing mode. After setting the write current and doses in an NPGS run file, the pattern is read and the electron beam is rastered such that only the designated area is exposed to the electron beam. The current and dose is determined by the resist thickness and the required resolution of specific patterned elements belonging to each layer. For the bilayer system, doses ranged from 550$\mu C/m^2$ to 800$\mu C/m^2$, and is usually optimized by performing a dose test, in which a variety of

identical elements are written with a varied dose on the same window, and then the best dose is selected for future writing processes. All lithography work done in this thesis was done utilizing a FEI Helios Dual Beam Nanolab SEM/FIB operated at 20kV.

After exposure to the electron beam, the resist must be developed. During development, the exposed resist is removed so that the substrate is exposed only along the desired pattern. The sample is developed first in a 3:1 solution of isopropyl alcohol (IPA) : methyl isobutyl ketone (MIBK) for 60s. Afterwards, it is rinsed with IPA for 30 s, then dried with a nitrogen gas flow. This stops the development process and prevents scumming. The sample is then baked at 110ºC for 60s to completely dry the substrate.

Post-development, the substrate is ready for material deposition. A variety of methods exist, such as thermal evaporation, sputtering, and e-beam evaporation. For the purposes of this work, e-beam evaporation represents the best technique, due to the ability to grow a very high quality film at a reasonable material/time cost. However, special attention must be given when using e-beam evaporation. If the temperature is too high, the resist can melt, leading to flow and obstruction of the pattern. This can result in distortions or a loss of sharpness to the pattern, and if it is too bad, it can prevent lift-off later. For this reason, the substrate is cooled through a chilled water line. Furthermore, for most metallic elements used in our work (Cr, Au, Py, Co, and Cu), this is not a problem. However, certain high melting point materials such as graphite can present a problem.

Following deposition, the sample must be promptly soaked in a polar solvent, which dissolves the remaining resist. During this process, deposited material on the surface of the resist is also removed. Typically, N-Methylpyrrolidone (NMP) is used as the solvent, however acetone may also be used. While soaking, the temperature is elevated to 70-90ºC and mixed using a

magnetic stirrer in order to facilitate lift-off. This process takes approximately 2 hours. After lift-off, an IPA rinse is performed, then blow dried with nitrogen gas, and baked at 110ºC for 90s to facilitate evaporation of any remaining IPA. If another writing step is required, this process is repeated. After all lithographic and deposition processes are completed, a Cr layer may be deposited on the opposite side of the Si_3N_4 membrane to prevent charging.

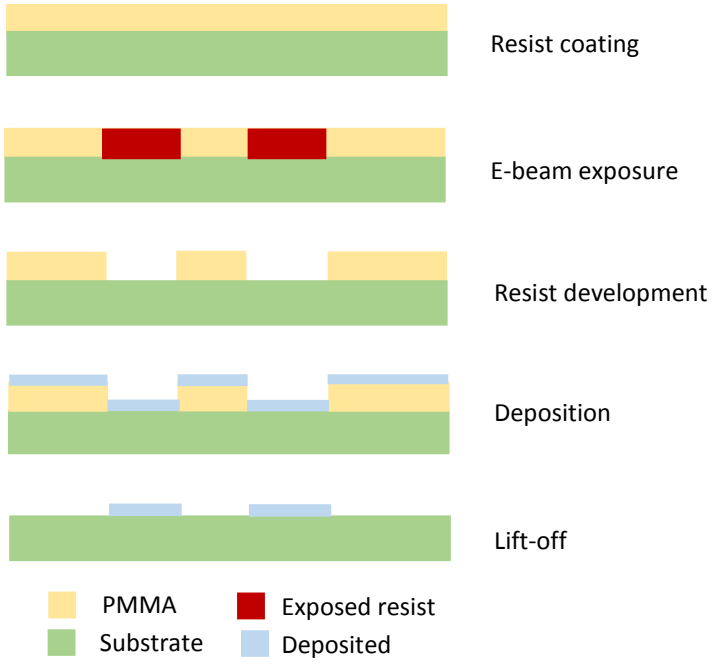

Figure 2.11 - Schematic of single resist sample processing showing the process from resist coating to lift-off.

2.4 Magnetism Overview

Magnetism, in most materials, is the result of the angular moment of the electron. This can be broken down into orbital ($\vec{L}$) and spin ($\vec{S}$) contributions, with the net angular momenta, $\vec{J}$, being $\vec{J} = \vec{L} + \vec{S}$. The orbital magnetic moment, $\vec{\mu}_L$, is given by $\vec{\mu}_L = \mu_B \vec{L}$ while the spin magnetic moment, $\vec{\mu}_S$, is given by $\vec{\mu}_S = 2\mu_B \vec{S}$, where μ_B is the standard Bohr magneton. Therefore, the net magnetic moment of an electron with a given $\vec{L}$ and $\vec{S}$ is $\vec{\mu}_{tot} = \mu_B(2\vec{S} + \vec{L}) = g\mu_B J$ where g is the standard Lande g-factor. The possible values of $\vec{L}$ and $\vec{S}$ is, in general, governed by the well-known Hund's rules, and due to this, it is possible for an atom to exhibit a net magnetic dipole moment. Depending on the electronic states occupied in a given configuration of atoms with magnetic dipole moments, this can result in a variety of magnetic categories. These are diamagnetic, paramagnetic, ferrimagnetic, and ferro- or antiferromagnetic.

Diamagnetism is a result in the change in electronic orbitals due to an applied field, and results in a negative magnetic susceptibility, i.e. $\chi < 0$, where χ is the magnetic susceptibility. In any material, the macroscopic response to an applied field can be given as $\vec{M} = \chi\vec{H}$, where $\vec{M}$ is the magnetization and $\vec{H}$ the applied field. It is apparent that a negative susceptibility indicates the magnetic response opposes an applied field. Diamagnetic effects are observed in all materials. However, they are typically very weak and, in materials where other forms of magnetism are present, may be effectively neglected. An exception to the weak diamagnetism case is in superconductors, where the primary effect is driven by free conduction electrons, and not electron orbitals.

On the other hand, paramagnetism is related to the spin angular momenta of the electron. Typically, within orbitals, electrons with opposite spin angular momenta will pair such that the

net spin component is zero. In systems where such pairing cannot occur, i.e. systems with unpaired electrons, there exists a weak net magnetic moment. When an ensemble of such paramagnetic atoms are placed in a lattice, they do not tend to align and the net magnetization is zero within the system. However, when a magnetic field is applied to a sample, the magnetic moments resulting from the spin contribution will tend to align along the direction of the magnetic field, and a net magnetization will emerge. Removal of the field results in the system returning to a randomized state with no net moment. This is indicative of the positive magnetic susceptibility present in paramagnetic systems. While diamagnetic effects still occur due to the orbital angular momenta, paramagnetic effects are typically 1-2 orders of magnitude stronger in most materials.

Ferromagnetism and antiferromagnetism are related in that they are the result of exchange interactions between neighboring (or near-neighboring) magnetic moments within a crystalline lattice. While many types of exchange interactions exist, the one discussed presently will be limited to direct Heisenberg exchange. Heisenberg exchange is a result of a combination of Coulomb interactions and the Pauli Exclusion Principle, and is the dominant mechanism for ferromagnetic and antiferromagnetic ordering in transition metals and alloys. Functionally, the energy resulting from this exchange can be written as $\boldsymbol{E_{ex} = -J(S_1 \cdot S_2)}$, where $\boldsymbol{J}$ is the exchange constant, and $\boldsymbol{S_1}$ and $\boldsymbol{S_2}$ are the interacting spins. The coupling term will vary in different material systems. In ferromagnetic materials, $\boldsymbol{J > 0}$ and in the antiferromagnetic case $\boldsymbol{J < 0}$. For transition metals, the Bethe-Slater curve, shown in figure 2.12, is a graphical representation of the exchange energy vs. the ratio of interatomic distance and radius of the 3d electron orbital, showing the transition from antiferromagnetic to ferromagnetic. Above a critical temperature, the magnetic ordering disappears, and this is known as the Neel temperature

for antiferromagnets and the Curie temperature for ferromagnets. Antiferromagnets exhibit a slightly positive magnetic susceptibility, similar to paramagnets, while ferromagnetic susceptibilities are significantly stronger.

Ferrimagnetism appears in systems in which the lattice is composed of inequivalent sublattices. Each sublattice has a different preferred magnetization direction. This often occurs when the sublattices are composed of different materials or ions. However, as the magnetization in each sublattice is inequivalent, a net magnetization persists. In this case, the magnetic susceptibility is still positive. Similarly, the transition temperature in which ordering is lost is also known as the Curie temperature.

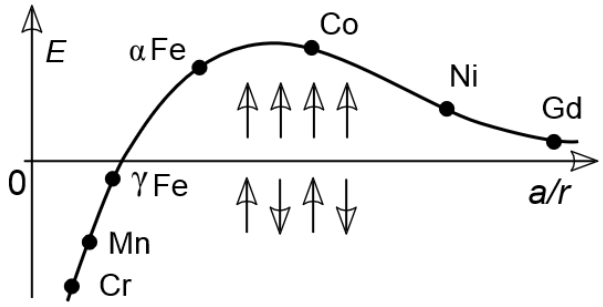

Figure 2.12 - The Bethe-Slater curve for transition metals, showing the exchange energy, E as a function of interatomic spacing.

2.5 Micromagnetism

Micromagnetism is a phenomenological model developed in the 1930's through 1940's in order to bridge the gap between Maxwell's theory of electromagnetism, which described the macroscopic properties of magnetic systems, and quantum theory, based on individual atomic spins described in the previous section. The approach is based on the minimization of the magnetic energy within the system. The fundamental assumption underlying this approach is that the volume averaged magnetization density, $\vec{M}(\vec{r})$, is constant in magnitude, but not direction. The magnitude, M_s, is the magnetization saturation per unit volume of the given object. By breaking $\vec{M}(\vec{r})$ into its individual Cartesian coordinate representation, it may then be expressed as

$$\vec{M}(\vec{r}) = \left(M_x(\vec{r}), M_y(\vec{r}), M_z(\vec{r})\right) = M_s(\alpha(\vec{r}), \beta(\vec{r}), \gamma(\vec{r})). \qquad (2\text{-}4)$$

In most magnetic systems, the Gibbs free energy can be expressed as the sum of four primary terms,

$$E_{tot} = E_{ex} + E_{an} + E_H + E_{demag}, \qquad (2\text{-}5)$$

where $\boldsymbol{E_{ex}}$ is the total Heisenberg exchange energy, $\boldsymbol{E_{an}}$ is the magneto-crystalline anisotropy energy, $\boldsymbol{E_H}$ is the energy resulting from interactions with an externally applied field, and $\boldsymbol{E_{demag}}$ is the energy associated with the demagnetizing dipolar interactions. Further energy terms, such as that which results from the Dzyaloshinkii-Moriya interaction, may be added as necessary, but typically are small compared to the four energies listed above, and will be ignored in this thesis.

2.5.1 Energies in ferromagnetic materials

The Exchange Energy

In ferro- and antiferromagnets, the exchange energy is a result of the strong but short-range Heisenberg exchange interaction. For two macrospins, $\overrightarrow{S_1}$ and $\overrightarrow{S_2}$, this is typically expressed as $E_{ex} = -J(\overrightarrow{S_1} \cdot \overrightarrow{S_2})$, where J is the coupling constant and is material specific. The sign of J determines the coupling between neighboring spins. If $J > 0$, parallel spin alignment is preferred, as is the case in ferromagnetism. If $J < 0$, the coupling is antiferromagnetic. In the continuum limit, E_{ex} may be expressed as

$$E_{ex} = A \int_V ((\nabla\alpha)^2 + (\nabla\beta)^2 + (\nabla\gamma)^2) dV, \qquad (2\text{-}6)$$

where A is the exchange stiffness constant for the given material, and the integral is taken over the volume of the magnetic material. When $J > 0$, the energy is minimized if the local magnetization lies parallel to neighboring magnetic regions.

Magneto-crystalline anisotropy energies

The magneto-crystalline anisotropy energy, E_{an} arises due to coupling between spin and orbital moments, typically referred to as L-S coupling. Due to this coupling, different crystal structures will have different preferential magnetization axis depending on their symmetry. The preferred magnetization axis is known as the crystalline easy axis. For hexagonally closed packed (hcp) lattices (such as Co), the c-axis represents the easy axis, while it is the <111>- axis for cubic lattices (such as Ni and Py). Furthermore, the electronic structure plays a vital role in determining the strength of this anisotropy. For example, for 4f materials, the enhanced L-S coupling results in strong anisotropies. The energy associated with the magneto-crystalline anisotropy is usually expressed as a Taylor series. For uniaxial anisotropy, this energy is given by

$$E_{an} = K_1 V sin^2\theta + K_2 V sin^4\theta + \cdots, \qquad (2\text{-}7)$$

where E_{an} is the anisotropy energy, K_1 and K_2 are the first and second order anisotropy constants, respectively, V is the magnetization volume, and θ is the angle by which the magnetization deviates from the crystalline easy axis. For most materials, higher order terms can be neglected.

Zeeman Energies

The energy from external fields, E_H, is also known as the Zeeman energy. It is a result of the interactions of a material's magnetic moments with an externally applied magnetic field, and is given by

$$E_H = -\int_V (\vec{M}(\vec{r}) \cdot \vec{H}_{ex}(\vec{r}))\, dV, \qquad (2\text{-}8)$$

where $\vec{H}_{ex}(\vec{r})$ is the external magnetic field. This energy is minimized when $\vec{M}(\vec{r})$ and $\vec{H}_{ex}(\vec{r})$ lie parallel to one another, and is the reason why a magnet will align along the magnetic field direction.

Demagnetization Energies

Finally, the demagnetization or dipole energy, E_{demag}, is the energy resulting from the interaction of magnetic moments with the magnetic fields resulting from discontinuous magnetization distributions. This term has contributions from both surface and bulk. The potential, $U(\vec{r})$, related to these contributions is

$$U(\vec{r}) = \frac{1}{4\pi}\left(\int_V \frac{\rho(\vec{r'})}{|\vec{r}-\vec{r'}|} dV' + \int_S \frac{\sigma(\vec{r'})}{|\vec{r}-\vec{r'}|} dS'\right) \qquad (2\text{-}9)$$

where $\rho(\vec{r}) = -\nabla \cdot \vec{M}(\vec{r})$ is the volume charge density and $\sigma(\vec{r}) = \vec{M}(\vec{r}) \cdot \vec{n}$ is the surface charge density. From the potential $U(\vec{r})$,the demagnetization field $\vec{H}_{demag}(\vec{r})$ may be derived as

$$\vec{H}_{demag}(\vec{r}) = -\nabla U(\vec{r}). \qquad (2\text{-}10)$$

The demagnetization energy, E_{demag}, is therefore given by

$$E_{demag} = -\frac{1}{2}\int_V \vec{M}(\vec{r}) \cdot \vec{H}_{demag}(\vec{r}). \qquad (2\text{-}11)$$

The dipole energy is long range in nature, and is heavily influenced by the boundary conditions of a finite structure, and for this reason is sometimes referred to as shape anisotropy energy for nanostructured materials. From the previously described energy terms, an effective field experienced by a macrospin may be determined by $H_{eff} = \frac{dE_{tot}}{d\vec{M}} E_{tot}$.

Other Energies

It should be noted here that specific energy terms have been omitted as they are not relevant to the work discussed in this thesis, and only play significant roles in a small subset of materials or systems. These include indirect exchange energies, which results from RKKY (Ruderman-Kittel-Kasuya-Yosida) coupling between two ferromagnetic materials separated by a metallic spacer, and energy resulting from anti-symmetric exchange, present only in certain materials with strong spin-orbit coupling. In many ferromagnetic patterned structures, it is the interplay between the demagnetization and exchange energies that lead to the formation of magnetic domains – the domain structure decreasing the total demagnetization energy, while the presence of sharp changes in magnetization at domain walls result an increase of the exchange energy.

2.5.2 The Landau-Lifshitz-Gilbert Equation

The Landau-Lifshitz-Gilbert (LLG) equations, initially described by Landau and Lifshitz in 1935, and modified by Gilbert in 1954 to include a more accurate damping term, is a highly non-linear ordinary differential equation used to solve the dynamics of macrospins within a bulk material. Typically, these equations are used to determine possible domain configurations in micron and submicron sized thin films, observe dynamic properties, or determine resonance frequencies and spin-wave spectra.

From the standard equation for the torque exerted on a magnetic object with magnetization of $\overrightarrow{M_s}$, $\vec{L} = -\overrightarrow{M_s} \times \vec{H}$, where $\vec{H}$ is a magnetic field, and $\vec{L}$ the magnetic torque acting on the body. Substituting $\gamma\vec{L} = \frac{d\overrightarrow{M_s}}{dt}$ gives the equation for the motion of an undamped macrospin, $\frac{d\overrightarrow{M_s}}{dt} = -\gamma\overrightarrow{M_s} \times \vec{H}$, where γ is the gyromagnetic ration. Including a phenomenological damping term, the full expression for the damped precessional motion of a macrospin influenced by an effective field may be written as:

$$\frac{d\vec{M}}{dt} = -\gamma\vec{M} \times \vec{H}_{eff} + \frac{\alpha}{M_s}\vec{M} \times \frac{d\vec{M}}{dt}, \qquad (2\text{-}12)$$

where α is the standard damping constant. The first term describes a precessional motion of $\vec{M}$ about the effective field, while the second term describes the relaxation of $\vec{M}$ towards the effective field (figure 2.13).

Later, the above model was expanded by Slonczewski to include the effects of spin transfer torque, by which spin angular momentum carried by electrons within an electric current could impart angular momentum to a macrospins within a magnetic material and will be discussed later in this thesis. Most commonly, this equations is solved with the publicly available software package OOMMF, available from the National Institute of Standards and

Technology, in which a given magnetic element is discretized into rectangular cells determined by the user. For thin films composed of a single material, the thickness is typically neglected, and the lateral cell sizes should be less than the exchange length of the magnetic material. To determine a static magnetization distribution, the cells are relaxed iteratively until a convergence criteria, given by the user, is reached. This is typically set to when $\vec{M} \times \vec{H}_{eff}$ is below a specified value. Furthermore, dynamic responses to time varying magnetic fields may also be simulated. It must be noted that, in cases where the dynamics of the system are important, the damping parameter plays a key role, and determines how fast and in what manner the magnetization, when perturbed, relaxes to its new equilibrium state. If the temporal dynamics are not essential, damping is commonly set to 0.5 or faster so that the system relaxes much more rapidly, decreasing the total simulation time.

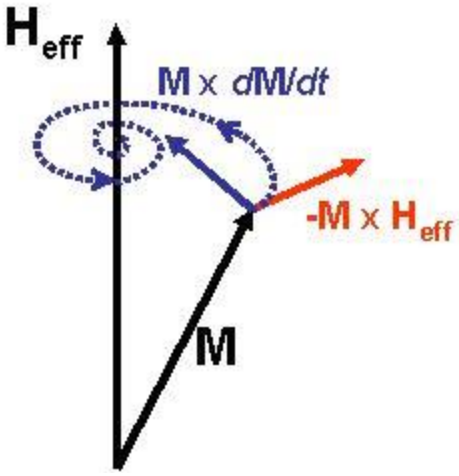

Figure 2.13 - Diagram showing the directions of both the precessional and damping terms in the LLG equation introduced above. The path of the magnetization is also shown (blue dashed line).

2.5.3 Magnetic domains and the role of shape anisotropy

The magnetization distribution of in any magnet is determined via the minimization of total free energy, which originates from the previously mentioned contributions – exchange, magneto-crystalline, Zeeman, and demagnetization. The importance of each term depends heavily on both intrinsic material parameters as well as extrinsic properties such as shape and externally applied fields. For the majority of the work performed in this thesis, the material of interest was permalloy ($Ni_{81}Fe_{19}$), a soft magnetic material with an exchange energy $A = 13 \times 10^{-12} J/m$ and a magnetization saturation of $M_s = 800 \times 10^3 A/m$. In this material, a damping coefficient of $\alpha = 0.01$ is typically used, although measurements have shown a range of values dependent on shape and microstructure of the film. The magneto-crystalline anisotropy is approximately zero, and can be completely neglected due to the polycrystalline nature of the films under study.

In general, any large ferromagnetic material at remnance will break into magnetic domains. These domains are regions within the material in which the magnetic moments lie in approximately the same direction. For a demagnetized sample, these domains will be randomly arranged such that the average net magnetization is zero, and is the reason for which many magnetic materials that are commonly available commercially do no exhibit macroscopic magnetism. As the dimensions of the magnet shrink, the number of domains present decreases as well.

At the micron and sub-micron scale, for zero applied field and no magneto-crystalline anisotropy, the magnetic domain structure is controlled largely via the interplay between exchange and demagnetization energies. The energetic anisotropies introduced by the shape is simply known as shape anisotropy. In these thin film structures, the magnetization will lie

predominantly in-plane in order to minimize charges on the surface of the film, which would result in large increases in the demagnetization energy.

Furthermore, in highly symmetric structures such as patterned discs and rectangles, in order to minimize charges at the edge, will result in the magnetization circulating about a central point. In the center, the magnetization will cant out-of-plane to avoid generation of a singularity in which the exchange penalty would be significant. This structure is known as a magnetic vortex, and the central point is the vortex core. The circulating magnetization can rotate either clockwise or counterclockwise (CW/CCW) and this is known as the chirality of the vortex, while the central point can cant either direction perpendicular to the film plane (±1), and this is known as the polarity (figure 2.14). In other elongated structures, such as nanowires or ellipses with large aspect ratios, this can result in single domain states where the magnetization points along the long axis of the element. Single domain magnets may also be generated by decreasing the element size beyond a critical size limit. In this case, the exchange energy associated with the creation of a domain wall is prohibitively high, so despite the presence of edge charges, a single domain structure is maintained. In other shapes, much more complex domain configurations can be controllably generated via modulations of the physical structure. As the elements increase in lateral dimensions, multiple domain shapes can be generated. With proper tuning of the in-plane dimensions of a magnetic thin film, a predefined domain state can be formed in order to further the understanding of domain dynamics in a controlled fashion.

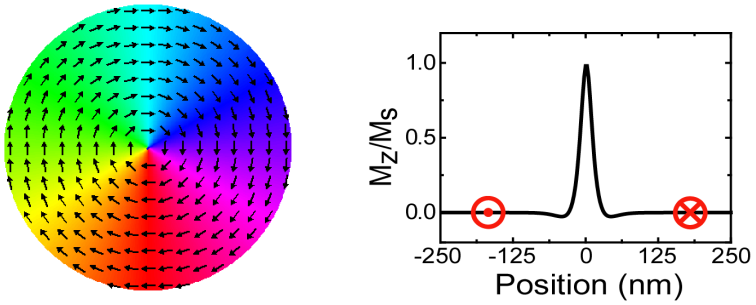

Figure 2.14 - Left: In-plane magnetization of a magnetic vortex structure in a circular disc. Right. Line scan showing the out-of-plane magnetization in the same disc. The core width is approximately of 20nm.

Chapter 3. Ordering in artificial spin ice lattices

3.1 Introduction to artificial spin ices

3.1.1 The magnetic vector potential

First introduced in the 1800's by Maxwell, the meaning of magnetic vector potential, $\vec{A}$, and whether it represented a meaningful quantity, was a controversial subject. It was soon discarded by Heaviside and Hertz as being physically meaningless [14]. However, in the 20th century vector potentials came in vogue again. Starting with Weyl's failed attempts to unify gravity and electromagnetism through the use of a vector potential, eventually Yang and Mills made use of them in the initial steps towards unifying the nuclear and electromagnetic forces [15]. In this context, the vector potentials are known as gauge fields, and are now viewed as fundamental in a variety of settings such as particle and high energy physics. The potential is related to the phase factor of the electron's wave function by

$$\exp[-\frac{ie}{\hbar}\left(\oint \vec{A}d\vec{s} - \oint Vdt\right)] \qquad (3\text{-}1)$$

where e is the electron charge, $\hbar$ is the reduced Plank constant, $\vec{A}$ is the vector potential, and V is the scalar potential. The Aharonov-Bohm effect, described in the next section, offers the first and most complete experimental evidence of the theory of gauge fields.

3.1.2 The Aharanov-Bohm effect and magnetic monopoles

The ability to directly measure and image the magnetic and electronic structure of materials in real space has proven to be invaluable in understanding the fundamental properties of a variety of systems, ranging from ferromagnets and ferroelectrics to superconductors [16]. In electron microscopy, a variety of phase imaging techniques exist, ranging from the less quantitative Fresnel mode [17], to more quantitative methods such as electron holography and the transport-of-intensity approach [18]. At the root of all of these methods lies the Aharanov-Bohm (AB) effect, a counterintuitive and fundamentally quantum mechanical phenomenon [4,19]. It is well known that an electron wave passing through a sample acquires a phase shift. The phase shift is given by

$$\varphi = C_e V t - \frac{e}{\hbar} \oint \vec{A}\, d\vec{s}, \qquad (3\text{-}2)$$

where C_e is a constant determined by the accelerating voltage of the electron beam, V is the average potential across the specimen thickness, t is the thickness, and $\vec{A}$ is the vector potential [16]. Of note, this is the same as the phase factor described in Yang and Mills gauge theories, and is also the same used in electron interference experiments such as holography. Commonly, the second term is written in regards to the magnetic field, $\vec{B}$, as

$$\varphi = C_e V t - \frac{e}{\hbar} \int \vec{B}\, d\vec{S}. \qquad (3\text{-}3)$$

However, this form of the equation disregards a fact realized by the individuals for which the effect is named. In space where $\vec{B} = 0$, $\vec{A}$ may still have a nonzero value and result in a phase shift of an electron, which can then be measured via an interference experiment. The typical description of such an experiment consists of an electron source, a detector, and, in-between, a solenoidal field that is shielded from the electron wave-front. In theory, the solenoid should be infinite to eliminate the leakage field, however this is difficult to achieve in practice [20]. Contrary to intuition, the electrons can experience a phase shift despite

experiencing no magnetic field, and, if real, the detector should record an interference pattern (Fig. 3.1a). Whether this effect was purely mathematical or if it was corresponding to a physically observable phenomena was heavily debated for many years [21–23], and remained elusive to experimental verification due to difficulties associated with the measurement. The AB effect was finally proven by Dr. Tonomura in an experimental tour-de-force using a toroidal permalloy magnet grown on SiO substrate coated by a niobium superconducting film (Fig. 3.1b, c) [24]. This layer of superconductor not only shielded the toroidal magnet from the incident electron beam, but the Meissner effect precluded leakage of stray magnetic flux to the surrounding vacuum. Use of a toroidal magnet also avoided the inherent difficulties in working with an infinite solenoid, which is experimentally unattainable. While the toroidal magnet itself was not electron transparent, the beam still passed through vacuum external the toroid and internally in the circular gap, and the relative phase shift in the gap and external to it could be measured. In this set-up, the phase shift should be quantized in multiples of π. Electron interference measured with electron holography showed a clear phase shift of exactly 0 or π. Not only did this solve a problem in physics that had stood for over 30 years, it also provided evidence for the theory of gauge fields by demonstrating that the gauge itself, not the magnetic field, was responsible for the observed phase shift.

Of further importance is the AB effect's roll in understanding the properties of magnetic monopoles. Since their prediction by Dirac in 1931 [25,26], the Dirac monopole and Dirac string have been sought after by physicists in a variety of settings, from the Relativistic Heavy Ion Collider at Brookhaven National Laboratory to the Large Hadron Collider, to detectors meant for monopoles produced not by colliders, but as relics from the early universe [27,28]. This special interest is primarily a result of their relation to the quantization of the electric

charge. In Dirac's formulation, the vector potential is that of a standard monopole charge, producing a field which is the magnetic equivalent to a Coulomb charge. However, to reconcile quantum mechanics with electromagnetism, Dirac added a line singularity, the Dirac string, carrying a flux *4πm* opposite the monopole flux, preserving $\nabla \cdot \vec{B} = 0$ (Fig. 3.1d). Gauge invariance of the string under rotations then implies that $m = \frac{\hbar c}{2|e|}$, where m is the magnetic charge, and e is the electron charge. This implies that if a Dirac monopole were to be found, it would imply the quantization of the electric charge. As we know, electric charges are indeed quantized. However, despite the intense interest, to this date all studies related to high energy or particle physics have given a null result with no evidence for a fundamental magnetic charge.

At first glance, the AB effect seems like a useful technique to observe monopole charges and Dirac strings. While the monopole itself would be observable to the AB effect and give the correct flux distribution, the Dirac string itself is invisible. By noting that $\varphi = \frac{e}{\hbar c} \oint \vec{A}\, d\vec{s} = \frac{e}{\hbar c}(4\pi m) = 2\pi n$, with *n* being an integer, after replacing *m* using the quantization condition, because phase differences of multiples of 2π are invisible to the AB effect, and hence the monopole itself would, in fact, be unobservable.

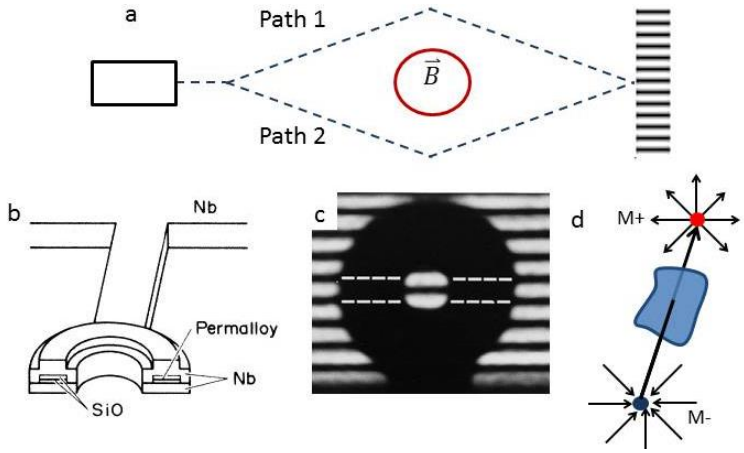

Figure 3.1 - (a) A sketch of a classic experiment demonstrating the AB effect. The magnetic field is zero outside of the cylinder at the center. However, electrons travelling outside of the field are still phase shifted, a result of a non-zero potential. The beam will exhibit a typical interference pattern. (b) Sketch of the toroidal magnet used by Tonomura to experimentally prove the AB effect. The outer layer is a superconducting Nb film, which prevents stray magnetic field from leaking into vacuum, as well as being thick enough to prevent electron penetration into the Permalloy magnetic layer. (c) Hologram taken of the toroidal magnet showing a π phase shift. Figures (b) and (c) are from ref. [14]. (d) Sketch of a pair of monopoles and Dirac string connecting them. The monopoles appear as sources (red) and sinks (blue) of magnetic field. Classical electromagnetism is preserved in the presence of monopoles by the tensionless Dirac string, acting as a solenoid carrying magnetic flux. Reprinted from "The Aharanov–Bohm effect, magnetic monopoles and reversal in spin-ice lattices," S.D. Pollard and Y. Zhu, *Microscopy* 62 (suppl. 1), S55-S64 with permission from Oxford University Press.

3.1.3 Introduction to spin ices

A new area garnering intense interest has arisen in recent years in the condensed matter setting of pyrochlore oxides ($A_2B_2O_7$, where A=Dy,Ho, B=Ti) in which quasi-particles which behave similar to the Dirac monopole and string and can be experimentally accessed and studied with phase retrieval techniques [29–33]. Spin ices are an intriguing system in which the lattice topology gives rise to an emergent gauge field as well as fractionalized magnetic charges. In the pyrochlore spin ices, magnetic moments within the pyrochlore lattice point along their Ising axis. This is similar to the dipole moments in water ice, and hence the name, spin ice. The low energy state at each vertex, in which four moments are arranged as with two moments pointing

into, and two out of, the vertex (Fig. 3.2a). In such a situation the ice rules are satisfied (2in/2out). Defects arise when a moment is switched, resulting in 3 moments into one vertex, and 3 out of another, violating the ice rules. These charges are then separated by switching subsequent adjacent magnetic moments. It was realized by Castelnova, *et. al* [31] that these defects would interact via a coulomb-like interaction and furthermore could be separated without any tension between them, behaving as free charges. In this situation, the defects could behave similar to the Dirac monopole and Dirac string, and hence, the ice-rule violating vertices have been termed monopole defects. These predictions were confirmed experimentally in neutron scattering, muon spin relaxation, and heat capacity measurements in $Dy_2Ti_2O_7$ and $Ho_2Ti_2O_7$ [30,33]. It should be noted that there are key differences between these emergent monopoles and flux channels and the Dirac monopole and strings proposed by Dirac himself. The monopoles that arise in spin ices are unquantized, and therefore observable to the Aharonov-Bohm effect, provided that the initial and final magnetic configurations of the lattice are known before and after application of some stimulus that leads to defects (i.e. reversal by a magnetic field) [34]. Despite the divergence between the emergent monopoles in spin-ices and the fundamental monopole, their existence in condensed matter systems has opened up a new field in which magnetic charges interacting via coulombic forces can be studied, as well as the behavior of flux tubes which are reminiscent of the Dirac string.

In atomic spin ices, these studies are limited due to the inability to use direct imaging techniques due to the need for atomic scale phase imaging techniques. However, a new approach has recently been implemented – simulating these atomic scale magnetic moments using micron-scale magnetic islands which act as analogs to the atomic scale spins of true spin ices [35]. These micron-scaled islands, when placed in either a square or kagome lattice [36],

form the basis for artificial spin ices. In these islands, the shape anisotropy leads to the magnetization lying along their long axis, and effectively behaving as Ising spins. All islands point into a vertex, with three elements forming the vertex in the kagome lattice, and four in the square lattice (Fig. 3.2b). The relative ease of the fabrication process has opened up a wide variety of parameter space, where coupling at vertices can be varied, disorder controlled, or even the ice rules can be modified (2 in/1 out or 1 in/2 out in Kagome, 2 in/2 out in the square [36–40]. Great interest has been devoted to the ordering of these systems, either through the use of a magnetic field or by thermal excitation [40–43]. Additional studies have focused on how the excitation and subsequent propagation of the macroscopic analogs to atomic scale spin-ice monopoles effect the ordering, of which real space imaging can give new insights [44–47]. Beginning with a known initial state, it is relatively straightforward to determine the location of not only the monopole defects, but also to determine the path that they have taken through the lattice. It is observed that the monopole defects are connected by chains of switched islands, which act as magnetic flux tubes. These flux tubes are similar in appearance to the solenoid field within a Dirac string, but macroscopic, observable, and unquantized. This makes electron microscopy an ideal tool to study these systems, due to both the scale of the islands and the change in phase of the electron being observable with the AB effect.

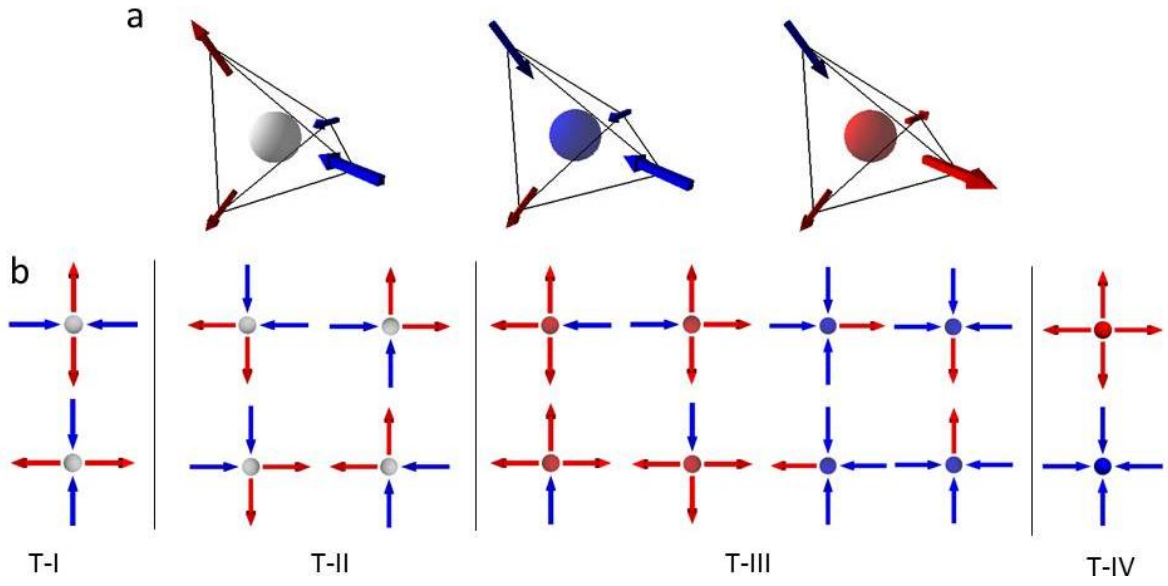

Figure 3.2 - (a) Schematic of possible magnetic moment configurations of a tetrahedron in the pyrochlore spin ice. Where the ice rules are satisfied (top left), there is no net moment (grey). Where the ice rules are violated, a net moment exists, either negative (blue) when 3 moments point into a vertex (middle), or positive (red) where 3 moments point out of a vertex. These vertices behave as magnetic monopoles. (b) Possible vertex combinations in a square artificial spin ice lattice showing four vertex types with different energies. T-I and T-II vertices satisfy the 2-in/2-out ice rules while the two others violate them. Vertex types are labeled in terms of increasing energy.

3.2 Reversal in artificial spin ice lattices

3.2.1 Experimental set-up

To directly observe ice rule violating defects, the associated connective flux channels, and related ordering during magnetic reversal, we perform an experiment on artificial square spin ice that is analogous to that performed on the pyrochlore spin ice in the work by Morris, *et. al* [33]. In that case, a field was applied along the (001) axis leading to saturation. It is apparent that in this configuration the ice rules are satisfied, and no monopole type defects are present. The system is then removed from saturation by decreasing the field, and the energy is minimized by the creation of monopole-antimonopole defect pairs connected by chains of switched elements – "Dirac strings (Fig. 3.3a)." We study a 14x14 vertex array of 100 nm wide, 300 nm long, and 30 nm thick Permalloy islands arranged in a "square" array by saturating the 2d lattice shown in figure 3.3b along the (11) axis. Following saturation, a field is applied in either the (01) direction or the (11) direction until the reordering process is complete. In the intermediate regime, we track the creation and propagation of monopole type defects in real space as they traverse the lattice. This behavior is what governs the reversal in these highly frustrated lattices. It must be noted that the analogy between this artificial spin ice and the pyrochlores is incomplete. The asymmetry in nearest-neighbor and next-nearest neighbor coupling results in a non-zero string tension. This can only be removed by adding a height offset between the different axes of the array [48], which is extremely challenging from an experimental standpoint and to date has not been achieved.

The array considered was created with standard electron beam lithography and evaporation techniques. Elements were fabricated such that the center to center spacing of

neighboring elements along the same axis was 450nm. Studies were performed in-situ using a JEOL3000F transmission electron microscope as well as dedicated JEOL2100F-LM Lorentz microscope. To image local moment configurations, we utilize phase retrieval electron microscopy – both with Lorentz imaging (Fig. 3.4a-c) and differential transport of intensity (D-TIE, Fig. 3.4d). As monopole type defects and the connecting strings are defined only by their excitations above the initial ground state, D-TIE represents a unique technique in which these excitations may be imaged directly, without convolution of extraneous background fields that complicate the identification of individual defects. These real space imaging techniques further allowed for vertex fractions, remnant magnetization, and correlations between individual islands to be quantified throughout the reversal cycle.

We also link our experimental measurements to numerical results in order to obtain further insights. In the artificial system, various methods have been used to simulate the system under different situations, most commonly a simple point dipole model [38,49]. In this method, used in this work, each individual element of the array is modeled as a point dipole with a critical switching field. The critical switching field is varied from element to element using a random Gaussian distribution centered at the critical field, which is determined from experiment. Switching occurs when the critical switching field ($H_{c,i}$) of the *i-th element* is exceeded by the sum of the external field plus the dipole fields of all other elements within the array, i.e. $H_{ext} + \sum H_{ij} > H_{c,i}$, where H_{ext} is the external magnetic field component along the (x,y) axes of the *i*-th element. The summation is performed over dipolar fields from all *j*-th elements relative to *i*-th element of interest, assuming that i ≠ j.

The vertices in the square array consist of four types, labeled as TI to TIV, in order of increasing energy (Fig. 3.2b). TI and TII obey the 2in/2out ice rules with a net vertex charge Q =

0, TIII and TIV do not, with Q = ±2 and Q = ±4 respectively, and are energetically unfavorable. In this geometry, the asymmetric nature of the four elements composing a vertex results in TI and TII vertices having different energies despite both following the ice rules, which results in the nonzero string tension. The ground state of this system consists of a tiling of the lattice with TI vertices, and due to the frustrated nature of such a system, has been difficult to obtain in experiment but of great interest for studying frustration physics in real space. A variety of methods have been used to achieve a pseudo-ground state - most commonly AC demagnetization protocols in which the sample is spun in a decaying AC magnetic field [35,46,49]. Additionally, thermal ordering processes during growth appear to show promise in achieving a low energy ground state [40,42]. To reveal the nature of the switching process in the square ice lattice studied here, the sample was subjected to magnetic fields along its (01) and (11) and symmetry axes, respectively, by tilting the sample within the magnetic field generated by the JEOL3000F microscope's objective lens [12], and the static state after field application was imaged.

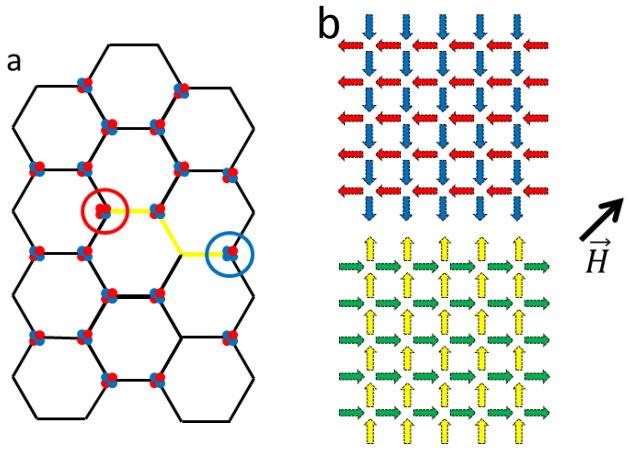

Figure 3.3 - (a) Projection of a pyrochlore spin ice along the [001] axis. Red (blue) indicates a magnetic moment pointing out of (into) a vertex. At vertices where the moments are unbalanced (red and blue large circles), monopole-like quasiparticles have been found to exist in ice-rule breaking points on the lattice. These quasiparticles are connected via flux channel reminiscent of the quantum mechanical Dirac string (yellow). Due to the system topology, the channel may be moved without additional energy cost, making them tensionless, resulting in free monopole-like defects. (b) Schematic of the experiment. The initial state (left) is polarized along the [-1 -1] direction, and then a field is applied as shown along the opposite direction, leading to a final polarization along the [11] direction (right). The local magnetization is determined for the intermediate field regimes to give insights into the switching process. Reprinted from "The Aharanov–Bohm effect, magnetic monopoles and reversal in spin-ice lattices," S.D. Pollard and Y. Zhu, Microscopy 62 (suppl. 1), S55-S64 with permission from Oxford University Press.

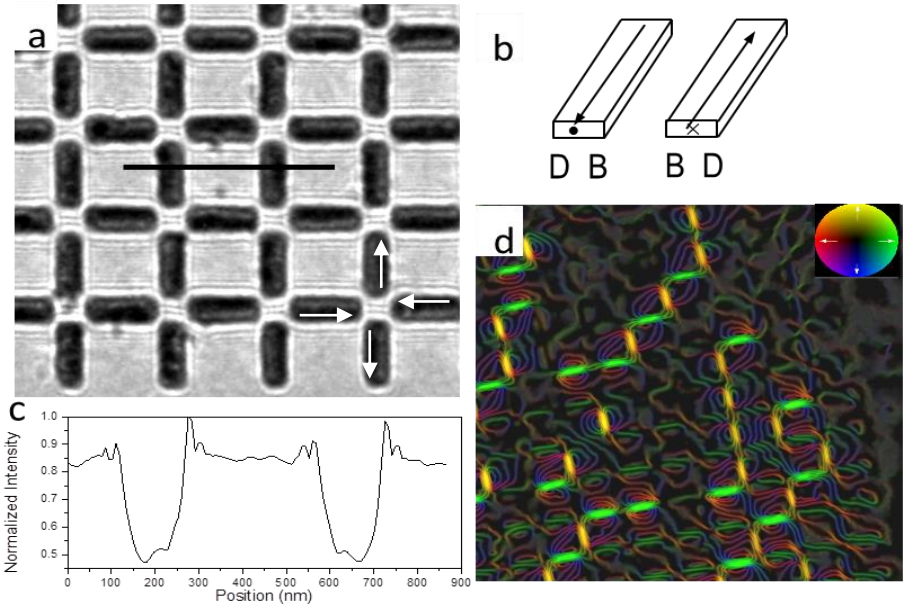

Figure 3.4 - (a) Lorentz TEM image of the square spin ice lattice of the Permalloy specimen. The arrows indicate the direction of the magnetization of each island. (b) Schematic of two oppositely magnetized bar elements in Lorentz imaging mode, showing the principle of the contrast asymmetry of bright(B) and dark(D) depending on the magnetization. (c) Linescan of the area shown in (a) demonstrating the contrast asymmetry for two oppositely magnetized elements. This asymmetry (or the location of the white contrast) can be used to determine the magnetization of each individual element, as marked by the arrows. (d) D-TIE image of the array, showing only flux associated with the switched elements. The ends of the chains correspond to the locations of ice rule breaking vertices, with the chains acting as flux channels between them. Reprinted from "The Aharanov–Bohm effect, magnetic monopoles and reversal in spin-ice lattices," S.D. Pollard and Y. Zhu, Microscopy 62 (suppl. 1), S55-S64 with permission from Oxford University Press.

3.2.2 Reversal along the (01)-axis

When a field was applied along the (01) direction, only elements oriented along that axis are reversed. Here, the different axes can be viewed as uncoupled. The only effect of the other axis present is to contribute a position dependent offset to the field required for switching. Switching occurs through the excitation of a defect pair, which propagates along the applied field direction. Defects with a charge of -2q (+2q) move opposite (along) the direction of the applied

field. In the case of the field being applied along the (01) axis, these chains are limited to the line of elements in which they nucleated. Nucleation typically, although not always, originates along edges, where pinning fields from neighboring elements are reduced. Two chains join when a +2q and a -2q defect come together and annihilate, forming a T-II vertex with no net charge, and a reduced vertex energy. Low energy T-I vertices and high energy T-IV vertices were never observed.

3.2.3 Reversal along the (11)-axis

The (11) axis fundamentally differs from the (01) axis due to the nature of its symmetry, allowing for the formation of low energy vertices which is not possible in the (10) or (01) reversal. Interactions and correlations between neighboring elements were studied by observing the in-plane component of the fringing fields of the individual magnetic islands as well as the local magnetization direction from Lorentz images (Fig. 3.4). This ability to image the field, unique from other common magnetic imaging techniques such as magnetic force microscopy or various X-ray techniques, allows for new insights in the physical processes governing to the frustration to be obtained.

The reversal initiates with the switching of single elements, creating a pair of defects with opposite charge. As the field is subsequently ramped, these defects propagate through the lattice in opposite directions, depending on their charge, and leaving behind a tail of switched elements (Fig. 3.5). These strings act as the channels of magnetic flux between the charges at the ends (Fig. 3.4d), similar to the solenoidal Dirac string in the classical monopole description. Initially, there is a marked increase in T-III vertex populations (monopole defects), at the expense of the

lower energy T-II vertices. As the field is further increased, T-I populations dramatically grow as defects propagate through the lattice. This is due to the asymmetric coupling between neighboring elements, which causes the defects to propagate predominantly along alternating axis and leaving behind a majority T-I vertices (seen in Fig. 3.4d as the step-like pattern). The highest degree of ground state ordering (as well as largest T-I populations) exist at low net magnetizations (Fig. 3.6a,b). To quantify the degree of ordering, we further examine correlations between neighboring elements, similar to those in previous works [35,47] in which correlations are +1 for ground state interactions and -1 otherwise. The correlation values shown in figure 3.6c.are averaged over each element in the lattice. Definitions for the three types of correlations in this work are given in the inset of figure 3.6c. As the net magnetization decreases, these correlations increase significantly. This, coupled with the large T-I populations, indicates significant but not complete ground state ordering. Furthermore, longer range correlations were approximately 0 at low net magnetizations, indicating a short range ordered yet highly frustrated magnetic state is achieved.

One interesting detail obtained from these results is seen in the saturation of monopole densities observed when populations are plotted against net magnetization. Below $M/M_s = 0.6$, T-III populations cease to grow (Fig. 3.6b), and are well below what would be expected in a non-interacting case. This can be explained through charge interactions. When defects of opposite charge occupy adjacent lattice sites, there is an attractive interaction. By looking at sequential Lorentz images, we see that in this case, neighboring charges annihilate more than 70% of the time that this transition is topologically allowable, significantly larger than the probability that this would occur randomly. Furthermore, high energy T-IV vertices (corresponding to two charges of the same sign occupying the same lattice site) never appear, a result of their repulsive

interaction. Evidence for these interactions can be further observed in real space with the bending of the magnetic flux lines near adjacent defects seen in the D-TIE images in Fig. 4d. Our simulations further show that they do not exist as transient states, which could be missed considering the slow acquisition time of the electron microscope. These observations hint at the strong role that magnetic charge ordering plays in enforcing the ice rules in these frustrated systems.

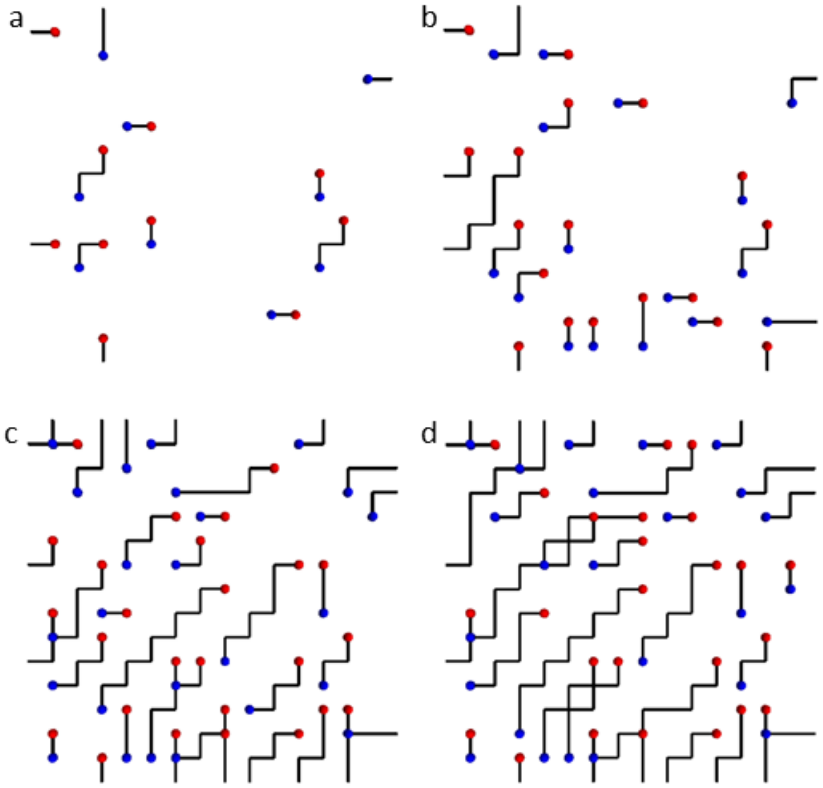

Figure 3.5 - Diagram of the switching process in the square spin-ice lattice. The field was applied along the [11] direction. The switching was reconstructed from consecutive Lorentz images recorded for applied magnetic field of 337 (a), 363 (b), 388 (c), and 413 Oe (d), respectively. Switched elements are shown in black, while unswitched elements are removed for clarity. Positive (negative) charges are denoted by red (blue) circles. The growth of density and chain length is clearly visible from (a) to (d). The step-like pattern that emerges is a result of the asymmetric coupling by flux channels between paired vertices or monopoles, and indicates large T-I vertex populations. All chains terminate at the lattice edges. Reprinted with permission from S. D. Pollard, V. Volkov, and Y. Zhu, Physical Review B 85, 180402(R) (2012). Copyright 2012 by the American Physics Society.

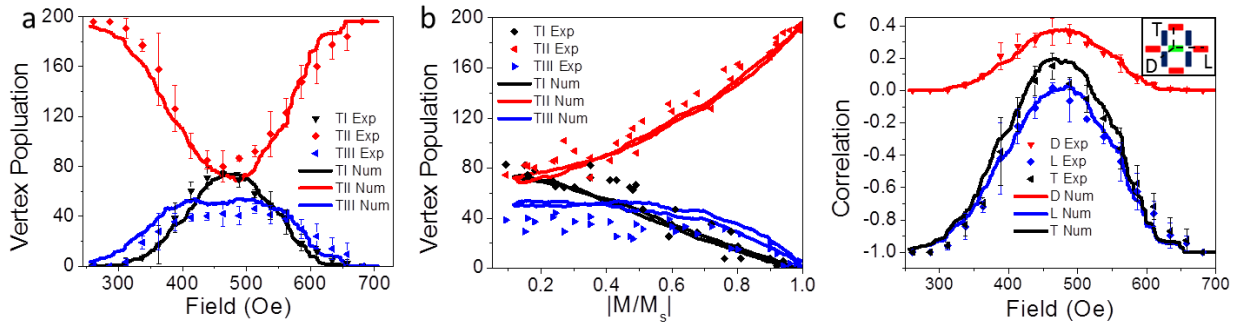

Figure 3.6 - (a) Vertex populations as a function of applied field. (b) Vertex populations as a function of normalized net magnetization (M/M_s). Data points are shown for four different samples during a reversal cycle. In both experimental and numerical results, T-III populations saturate below a net magnetization of about 0.5. (c) Correlation effects as a function of applied field. In all plots experimental data are shown by discrete symbols, while theoretical calculations are shown by solid lines of the appropriate color. Reprinted with permission from S. D. Pollard, V. Volkov, and Y. Zhu, Physical Review B 85, 180402(R) (2012). Copyright 2012 by the American Physics Society.

3.3 Demagnetization cycling

Due to the high degree of ordering that we have observed during a single reversal cycle along the (11) axis, comparable to that achieved by a more complicated AC demagnetization cycle, we use simulations to study how a decaying AC field applied along the (11) axis further orders the frustrated system. Here we discuss the results of these simulations. Following each semi-cycle of the hysteresis loop, the maximal field is decreased. The demagnetization using a (11) cycling is distinctly different from the mechanism that drives the more common AC demagnetization protocol. Whereas the standard AC demagnetization protocol alternatingly switches the (10) and (01) axis for different angles during the sample rotation [49], the (11) cycling simultaneously switches both axis, exploiting the asymmetric coupling of the vertices along with the symmetry of the (11) axis to achieve local ground state ordering. During successive cycles, low energy T-I vertices become frozen for subsequent field steps. Meanwhile, TII vertex links between monopoles can "break", separating the string into two sets of defect pairs that then may propagate through the lattice to form more T-I vertices (Fig. 3.7). At the end of the cycling, the majority of T-III vertices remaining are the results of trapped defects, in which their motion is only possible through the destruction of a low energy T-I vertex or the creation of high energy T-IV vertices. This results in the low T-II and T-III populations, while achieving large populations of T-I vertices as well as large ground state correlations. For the case we simulated in this work, we used parameters identical to the (11) reversal - a 300Oe switching field with 60Oe variation with the same misalignment from the (11) axis. The field cycles such that the maximal amplitude decreases by 20 Oe each half-cycle (Fig. 3.7c). Initial iterations show no change in correlations of vertex populations from the single cycle reversal, as the applied field is too large, leaving all T-I vertices unfrozen. However, for intermediate regions,

T-I vertices become frozen, and do not change for subsequent cycling. This results in much larger final T-I populations and correlations at the end of the ordering process as compared to the simple reversal (Fig, 3.7d, e). Using the (11) AC cycling procedure, we are able to achieve a near zero net magnetization, along with TI vertex fractions of approximately 62%, with T-III populations minimized at less than 10% of the total vertex populations. Furthermore, correlations rise to about 0.60 for D, 0.32 for L, and 0.42 for T, suggesting a high degree of ground state ordering and a suppression of frustration. This opens up a new method for achieving a quasi-ground state in which the behavior of emergent monopoles, and their relation to frustration physics, can be studied on the macroscale.

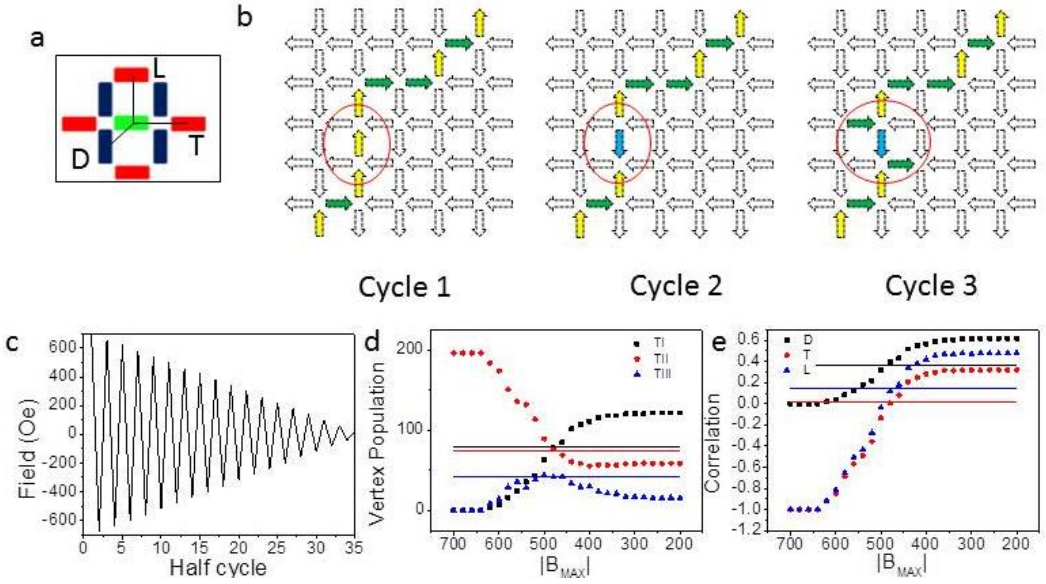

Figure 3.7 - (a) Definitions for diagonal (D), transverse (T), and Longitudinal (L) correlations in the square spin-ice lattice. (b) Schematic of the multiple step switching in a (11) demagnetization. A chain is broken by switching an unfrozen T-II vertex. This creates two new defects which may propagate, creating new T-I vertices. (c) The demagnetization field cycle protocol. Each half cycle the field is decreased by 2 mT until it falls below the field required to switch elements. (d) Vertex population vs. the amplitude of the field for each cycle. (e) Correlations vs. Field. It is apparent that the end of the cycling results in a high degree of ground state ordering, but complete ordering is blocked due to frustration effects. Lines in (d) and (c) correspond to vertex populations and correlations, respectively, at maximal ordering during a single experimental cycle as reference. Reprinted from "The Aharanov–Bohm effect, magnetic monopoles and reversal in spin-ice lattices," S.D. Pollard and Y. Zhu, Microscopy 62 (suppl. 1), S55-S64 with permission from Oxford University Press.

3.4 Summary

In this section, we presented results that give insight into ordering processes in artificial square spin ice lattices. Specifically, the reversal was tracked using a combination of Lorentz imaging and D-TIE. This allowed for vertex populations and correlations to be tracked as a function of field and net magnetization. Short range interactions between defects limit the overall population of defects within the lattice, as attractive interactions between defects of opposite charge tend to lead to annihilation of defect pairs for neighboring vertices. Furthermore, we found that by proper selection of applied field direction, a high degree of local ground state ordering could be achieved, although long ordering was still blocked due to frustration effects. With this in mind, we have proposed a simple method in which an even larger degree of ground state ordering could be achieved, and tested this using a numerical model based on treating the elements as Ising spins that interact solely through dipole-dipole interactions.

Chapter 4. Spin torque driven magnetic vortex dynamics

4.1 Motivation

In ferromagnets, imbalances between spin populations of conduction electrons result in the spin polarization of an electrical current that flows through a ferromagnet. This spin polarized current imparts spin angular momenta, in addition to the charge current, to the local magnetic moments composing the ferromagnet, and as such can cause changes in the local spin texture. In the LLG equations, this is accounted for via the introduction of two new phenomenological terms representing adiabatic and non-adiabatic contributions, respectively. The modified LLG equation is formally written as

$$\dot{\vec{m}} = \gamma\vec{H} \times \vec{m} + \alpha\vec{m} \times \dot{\vec{m}} - [\vec{u} \cdot \vec{\nabla}]\vec{m} + \beta\vec{m} \times ([\vec{u} \cdot \vec{\nabla}]\vec{m}), \quad (4\text{-}1)$$

where $\vec{m}$ is the magnetization, γ is the gyromagnetic ration, $\vec{H}$ the effective field, α the viscous damping parameter, $\vec{u}$ a velocity term related to the spin current, and β the non-adiabatic parameter [50,51]. The first two terms were introduced in Chapter 2 of this thesis and describe the standard response of the magnetization to an effective field, while the last two describe the effect of a spin polarized current. While the third term is well understood, the non-adiabatic effects, including its origin and magnitude, have not been clearly determined.

Filling the gap in knowledge of the non-adiabatic spin torque is of particular importance for a variety of spintronic device applications. This is because, in current driven magnetic domain dynamics, the speed at which a domain wall will propagate scales linearly with β below the Walker breakdown [52–54]. Above the Walker breakdown threshold, the domain wall

begins to experience turbulent motion and deformations, and domain wall mobility is greatly reduced, imposing limits on the speed at which spintronic devices based on domain walls can operate. Thus, a better understanding of the origins and magnitude of the non-adiabatic spin torque in various materials will facilitate the development of future spintronic devices [55].

One of the primary reasons for the lack of understanding of the non-adiabatic effects is that experimental constraints make its measurement exceedingly difficult. In nanowires, for instance, local structural variations and differing assumptions have led to a range of reported values of β, ranging from $\beta \approx \alpha$ to $\beta > 18\alpha$ [56,57]. One cause for concern in utilizing nanowires for these measurements is that the dynamic domain wall motion here can lead to continuous domain wall transformations for moderate defect densities. These transformations will result in measurements for non-adiabatic spin torques to incorrectly converge to being equal to α [58–60].

Furthermore, in these prior works, to determine the relevant ratio of β/α, the value of α was assumed, although it can vary greatly depending on the both the shape and microstructure in these patterned films. Other attempts have been made utilizing highly symmetric structures exhibiting a magnetic vortex state. The symmetry of these structures has led to ways to circumvent many of the issues that arise in nanowire geometries. In highly symmetric discs in which there is little or no magneto-crystalline anisotropy, the magnetization can rotate about a central point, minimizing the Zeeman energy, at the cost of increasing exchange energy. In order to prevent an energetically unfavorable singularity at this central point, the magnetization may cant out of plane. The rotational direction of the magnetization is known as the chirality, and may be either clockwise (CW) or counterclockwise (CCW), while the out of plane component is

known as the polarity, and may point in either of the two normal directions of the discs surface (+,-).

The vortex core has generated intense interest due to the many possible spintronic applications that it holds, ranging from use as a magnetic memory or logic element, to microwave signal generating and processing applications [61–63]. This is in large part due to its stability with large displacements and core velocities, which allows for the core to be treated as a topological soliton [64]. From a magnetic logic and memory perspective, the core may also be utilized as a quarternary recording device supporting four stable states that may be controllably switched using a short field or current pulse.

When an electrical current is passed through the magnetic vortex, the domain configuration and location of the vortex core will be modified. However, deconvoluting the effects of the adiabatic, non-adiabatic torques, as well as residual Oersted fields is complicated as the individual effects are small. Separating these effects is necessary for an accurate determination of β. Previously, the most accurate reported values of β were taken using X-ray measurements of the displacement of a vortex core by a DC current pulse in circular magnetic discs. By measuring the displacement for the two chiralities of the vortex core, a value of β can be extracted. Due to the spatial resolution limits of the techniques involved, the relatively small displacement, and pinning effects from spatial inhomegneities, the error in these measurements is about 50% the measurement itself [52]. A similar measurement was recently performed using scanning electron microscopy with polarization analysis, producing a similar result with significantly greater precision [65]. The method demonstrated in this chapter differs in that it utilizes a dynamic approach in TEM, resulting in larger displacements and, therefore, smaller relative errors, as well as the improvements resulting from the high spatial resolution of

TEM [66]. Additionally, it has been previously shown that for resonant excitations driven by only moderate excitation fields or currents, pinning effects can be ignored [67,68], further reducing effects that can lead to misinterpretation of β.

4.2 Introduction to resonant vortex dynamics

When a magnetic vortex is perturbed from its equilibrium position and allowed to relax, it will undergo damped precessional motion about its new equilibrium position, as described in figure 4.1. The characteristic frequency of this damped motion is determined by the details of the potential well that the vortex resides in, which for most geometries and small perturbations can be modeled as approximately harmonic. Therefore, the damping behavior resembles that of a damped harmonic oscillator [69,70]. The exact details of the local potential depends on material parameters and the energy cost associated with small displacements about equilibrium. When the core is driven by a time varying excitation set to this characteristic frequency, the core will undergo high amplitude periodic motion. This frequency is known as the resonance frequency, and the dynamics here are known as resonant dynamics. A variety of analytical models exist that may be used to predict the resonance frequency of a magnetic vortex in either a square- or circular-disc. For example, in a circular disc with small vortex displacements, a side-charge free model can be used, from which it the resonant frequency can be determined [70]. In this model,

$$\omega_0 = 2\gamma M_s \left[4\pi F_v(\zeta) - 0.5\left(\frac{E_l}{R}\right)^2\right], \quad (4\text{-}2)$$

where γ and M_s are the usual constants $F_v(\zeta)$ is a function of the discs aspect ratio ζ, E_l is the material's exchange length, and R is the disc radius. For arbitrary shapes, micromagnetics may be used to determine the resonance frequency. First, a pulse field is used to displace the vortex core from equilibrium. Subsequently, the vortex is allowed to relax. The vortex precesses about the new equilibrium point in a decaying orbit at the characteristic frequency of the particular

disc. The frequency at which this orbit decays is the eigenfrequency for the vortex (Figure 4.1). For the work shown in this section, we focus on the dynamics of a driven vortex in a square disc.

In a square disc, if the vortex is driven by solely an external field, the orbit will be circular at the resonant frequency, or elliptical along the x- or y- axis, depending on the chirality and whether the excitation is over or under the resonant frequency (Fig. 4.2). The situation becomes more complicated when a spin polarized current is utilized, and determining orbit properties via micromagnetics becomes prohibitively time consuming. However, the symmetry of the problem has allowed for development of an analytical model that reproduces micromagnetic results reasonably well, and can be used to rapidly calculate orbit trajectories for given experimental parameters [71,72].

Assuming a rigid vortex core (reasonable for moderate to even large displacements, with velocity $\vec{v}$, material thickness t, polarity p, and magnetization saturation M_s, the vortex motion can be described by the Thiele equation [73], which has been expanded by Thiaville to include the influence of spin polarized currents [74], as

$$\vec{F} + \vec{G} \times \left(\vec{v} + b_j \vec{j}\right) + D\left(a\vec{v} + \beta b_j \vec{j}\right) = 0, \quad (4\text{-}3)$$

where $\vec{F}$ is the force on the core due to external and stray fields, $\vec{G} = -\left(\frac{2\pi M_s \mu_0 tp}{\gamma}\right)\hat{e}_z$ is the gyrovector, $b_j = P\mu_b / \left[eM_s(1+\beta^2)\right]$ is the coupling constant between the magnetization and the spin polarized current, P is the spin polarization, β the degree of non-adiabaticity associated with the spin torque, $\vec{j}$ the current, and $D = -\frac{\pi M_s \mu_0 t \ln\left(\frac{l}{a}\right)}{\gamma}$ the simplified dissipation with $\frac{l}{a}$ being a geometric parameter dependent upon the side length l and thickness of the square.

For the square structure, assuming small displacements, Krüger *et al.* determined that the confining potential may be modeled as

$$E_s = \frac{1}{2} m\omega_r^2 (X^2 + Y^2), \qquad (4\text{-}4)$$

where X and Y define the vortex core position [71]. The following derivation is performed assuming the current flow is spatially uniform along the length of the sample. However, inhomegeneities in the current flow along the z-direction, typical in normal device geometries, result in an extraneous Oersted field that must be accounted for. By exploiting the symmetry in the domain structure of a square element, the Zeeman energy resulting from the field can be approximated as

$$E_z = \frac{\mu_0 M_s Hltc}{2}\left[\left(\frac{l}{2} + X\right) - \left(\frac{l}{2} - X\right)\right]. \quad (4\text{-}5)$$

These two energies can be used to determine the force on the vortex core, as $\vec{F} = -\vec{\nabla}(E_s + E_z)$. Inserting the above into the modified Thiele equation, the equations of motion for the vortex are found to be

$$\begin{pmatrix} \dot{X} \\ \dot{Y} \end{pmatrix} = \begin{pmatrix} -\Gamma & -p\omega \\ p\omega & -\Gamma \end{pmatrix} \begin{pmatrix} X \\ Y \end{pmatrix} + \begin{pmatrix} \frac{p\omega\Gamma}{\omega^2+\Gamma^2}\frac{\mu_0 M_S Hltc}{G_0} - b_j j - \frac{\Gamma^2}{w^2+\Gamma^2}\frac{\beta-\alpha}{\alpha} b_j j \\ \frac{-\omega^2}{\omega^2+\Gamma^2}\frac{\mu_0 M_S Hltc}{G_0} + \frac{\Gamma^2}{w^2+\Gamma^2}\frac{\beta-\alpha}{\alpha} b_j j \end{pmatrix}. \qquad (4\text{-}6)$$

Assuming harmonic excitations (i.e. $H(t) = H_0 e^{i\Omega t},\ j(t) = j_0 e^{i\Omega t}$, with Ω the driving frequency), and ignoring exponentially damped terms (since we only care about the steady state orbit here), the time dependent position of the magnetic vortex core is

$$\begin{pmatrix} X \\ Y \end{pmatrix} = \frac{-e^{i\Omega t}}{\omega^2 + (i\Omega + \Gamma)^2} \begin{pmatrix} \left(\tilde{H} + \frac{\Gamma\beta}{\omega\alpha}\tilde{j}\right)\omega + \left(\frac{\Gamma}{\omega}\tilde{H} + \tilde{j}\right) i\Omega \\ \tilde{j}\omega p - \left(\tilde{H} + \frac{\Gamma}{\omega}\frac{\beta-\alpha}{\alpha}\right) i\Omega p \end{pmatrix}, \qquad (4\text{-}7)$$

where $\tilde{H} = \frac{\gamma H_0 lc}{2\pi}$ and $\tilde{j} = b_j j_o$.

From here, it is easily seen that if $\omega = \Omega$, the orbit is circular, while if $\omega \neq \Omega$, the orbit is elliptical, with the degree of ellipticity increasing as the frequency moves further off resonance. Furthermore, off resonance, the orbit amplitude significantly decreases. More importantly, this relation shows a dependence of the orbit size on the degree of non-adiabaticity. The direction of

this dependence varies on the chirality of the vortex core, either adding to the magnitude of the displacement, or subtracting from it. Calculated trajectories, as well as fully simulated micromagnetics of current driven vortex motion are shown in figure 4.2. It can clearly be seen that the analytic model well reproduces the results from micromagnetics.

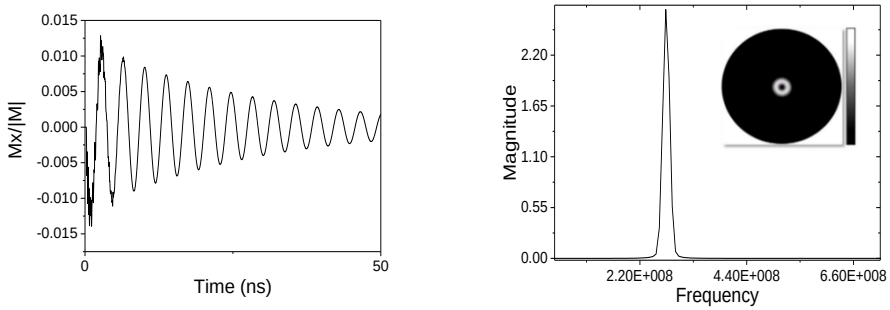

Figure 4.1 – Left: Magnetization of 1μm permalloy disc following a 5 Oe field pulse showing the characteristic damped response. Right: FFT of the magnetization response. The frequency indicated is the resonance frequency for the disc. The inset shows the time averaged z-component of the magnetization when excited at the given resonance frequency.

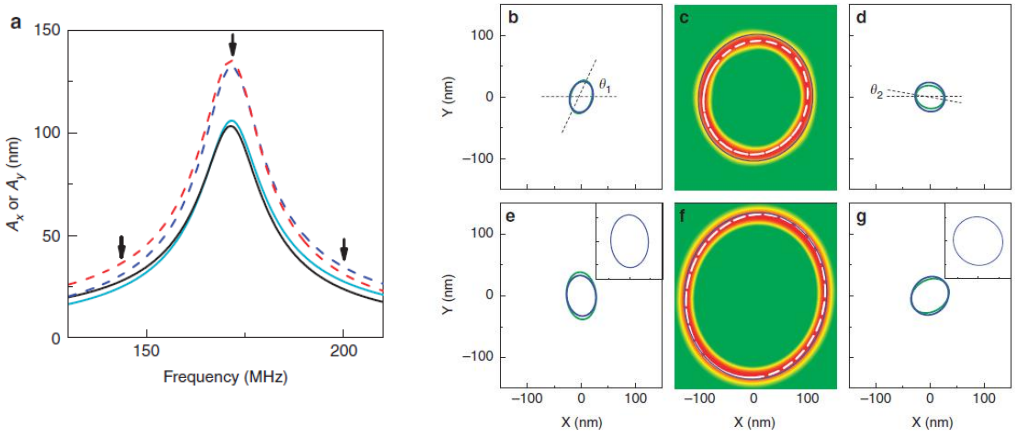

Figure 4.2 - (a) Simulated orbit amplitude versus frequency for CW (solid) and CCW (dashed) chiralities. Both A_x (blue and cyan) and A_y (red and black) are shown. (b-g) Orbit paths corresponding to the frequencies marked in (a), for positive polarities. The blue lines indicate trajectories obtained from the analytical model, while green lines are from micromagnetics. (c,f) are the results of fully 3D micromagnetic simulations at resonance showing the thickness averaged z-component of the magnetization, the peak z-component (white dashed line) and analytic model (blue). The insets show the resulting trajectories if spin torque contributions are ignored. These models assume a current density of $7.7 \times 10^{10} A/m^2$, an Oersted field of $1.7\ Oe$, a spin polarization of 0.6, a damping parameter of $\alpha = 0.016$, and $\beta = 10\alpha$.

4.3 High Frequency measurements in TEM

In order to measure the non-adiabatic contribution to magnetic vortex orbits, and hence the magnitude of the non-adiabatic spin torque parameter, it is necessary to directly image the trajectory with high resolution *in situ*. To do this, we make use of a new TEM sample holder designed at Brookhaven National Laboratory in combination with high frequency signal generation (figure 4.3). While many previous sample holders allow for application of quasi-static or low frequency electrical currents to a given sample, because the vortex gyrotropic mode is on the order of 100's of megahertz to a gigahertz, a holder specifically designed to allow such high frequencies with minimal waveform loss is necessary. The custom holder in this work has been modified with a vacuum compatible SMA feedthrough, which is connected to a copper coplanar waveguide on the vacuum side of the TEM holder. A sample is prepared on a Si_3N_4 membrane via electron beam lithography and electron beam evaporation. In order to allow for electrical connections to be made to the silicon nitride, either the sample is deposited on-top of a fabricated microwave stripline (typically made of a thin layer of Au or Cu) for Oersted field excitations, or, for spin torque induced excitations, is patterned in-line with a stripline in which the element forms electrical continuity with two Au or Cu arms (figure 4.4). 50μm x 50μm contact pads for the striplines are fabricated away from the thin window on the bulk Si_3N_4 in order to prevent breaking of the window. For spin-torque excitations, first, the Py elements are patterned and deposited, as well as alignment marks which are then used for the second step. In the second step, after using the marks to align the beam, two electric contacts are patterned which overlap opposite edges of the elements by 250nm in order to ensure a continuous electrical pathway. Finally, a 50-100nm thick electrode layer is deposited. For Oersted field driven excitations, the process is reversed – first the contact pads and alignment marks are

patterned and deposited, and then magnetic elements are deposited on top of the striplines. In this case, there is no gap in the electrical contact pads, and it forms one continuous strip. Wedge wire bonding using aluminum wire is then used to provide electrical connections between the coplanar waveguide and the striplines.

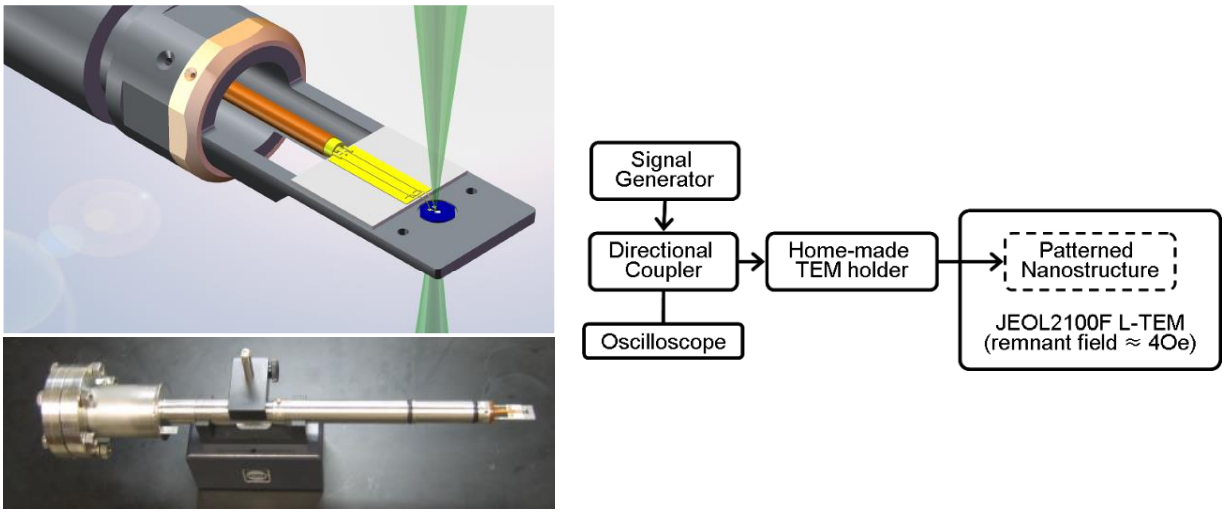

Figure 4.3 - Left top: Schematic diagram of the sample holder endpiece. The green cone represents the electron beam. Bottom: Photograph of the sample holder. Right: Electrical schematic of the excitation scheme.

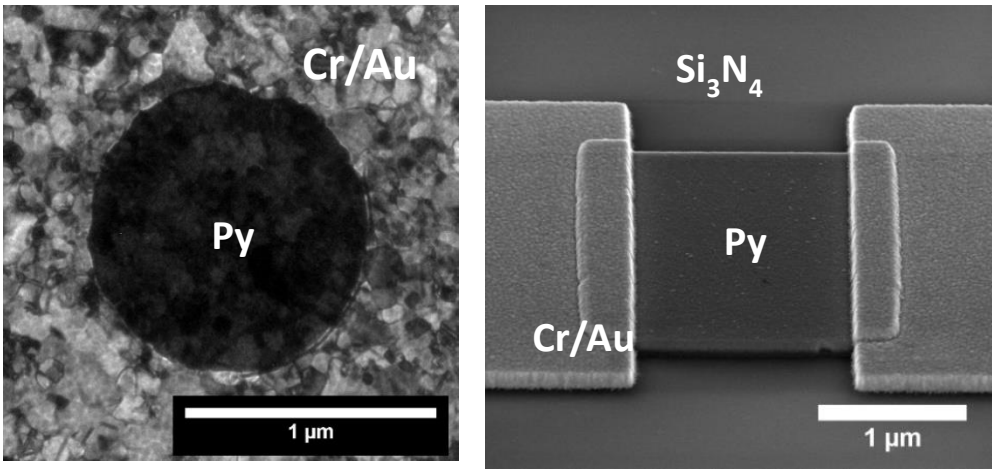

Figure 4.4 - Left: Typical TEM image of a Py element used for purely Oersted field excitation. The Py element is on top of an Au stripline (with a 2nm Cr seed layer). Right: Typical spin torque geometry. The Py forms the connection between two Au contacts.

4.4 General resonance behavior and the determination of α

To determine the effects of non-adiabatic spin torque on vortex behavior, and obtain a more accurate value for this important parameter, we performed measurements of the resonance curve of a vortex in a 2μm x 2μm x 50nm Py structure exhibiting a magnetic vortex domain (Figure 4.5) such that experimental results could be compared to the analytical model described previously. This allows for not only the determination of β, but also validation of off-resonant phenomena, as this has never previously been explored due to the lack of spatial resolution afforded by other measurement techniques. Because the typical TEM is limited to about 30ms time resolution, an image gives the trace of the average magnetization distribution over this given time window, as opposed to truly dynamic imaging. For dynamic excitations of magnetic vortices, what is therefore observed is the trace of the total orbit of the core over the given acquisition time. This is shown schematically in Fig. 4.6.

A resonance sweep taken at a current density of $7.7 \times 10^{10} A/m^2$ for a vortex of CCW chirality is shown in Fig. 4.7. Far below resonance, the core orbit is relatively small, elliptical, and tilted off-axis. As resonance is approached, the vortex orbit grows in size. We identify the resonance frequency as the frequency at which the orbit reaches it's maximize size. Typically, images are taken every 5 MHz. Beyond this point, the orbit begins to again develop an ellipticity, and the orbit size shrinks until the vortex returns to a static point. Fig. 4.8 shows the resonance curve given at this frequency. Initially no oscillations are observed, followed by a jump to an orbit radius of approximately 15nm. This jump is attributed to depinning from a local defect, as modulation in local structure can result in pinning potentials on the order of a few eV. The growth in orbit then continues until approximately 180MHz, where it again decreases. A final drop from approximately 15nm to 0nm again is ascribed by defect pinning effects. From

the linewidth of the resonance curve, the damping parameter may be identified without any a priori assumptions. The lack of a necessity to assume values for many material parameters is one of the strengths of this technique. As the measured of α is both a result of intrinsic phenomena of a material, but also may be impacted by extrinsic factors such as local microstructure and geometric effects, having the ability to determine α for an individual nanomagnetic element is essential to properly identify the ratio of β/α. For the specific sample shown here, we find that $\alpha = 0.016 \pm 0.001$, slightly larger than the typical value of $\alpha = 0.01$ but within the range of previously measured values in patterned magnetic permalloy elements found in the literature. This indicates that extrinsic factors may play a significant role in the damping phenomena within patterned magnetic media.

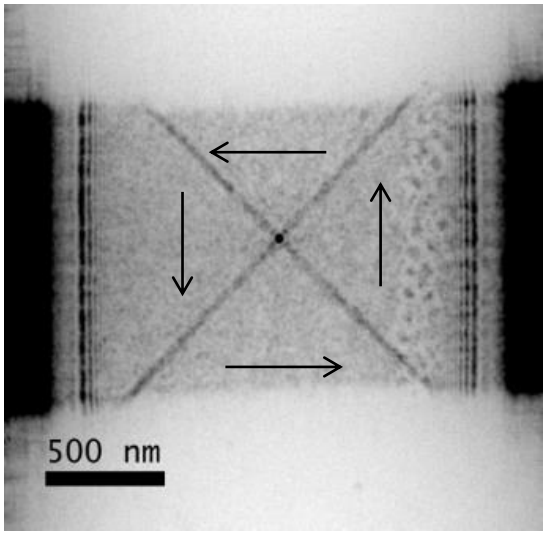

Figure 4.5 - Lorentz image of the structure for spin-torque excitation with no applied current. The arrows indicate the direction of the magnetization

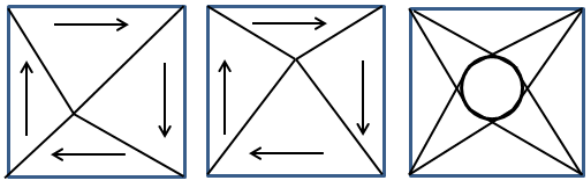

Figure 4.6 - Image formation of a vortex orbit in TEM. The two images on the left show the vortex positions at two points in time. In TEM, since the acquisition time is much longer than the time necessary for the vortex to complete a full cycle, the average is seen, resulting in the typical elliptical contrast at the disc center, as well as contrast resulting from the averaged 90-degree domain wall oscillations.

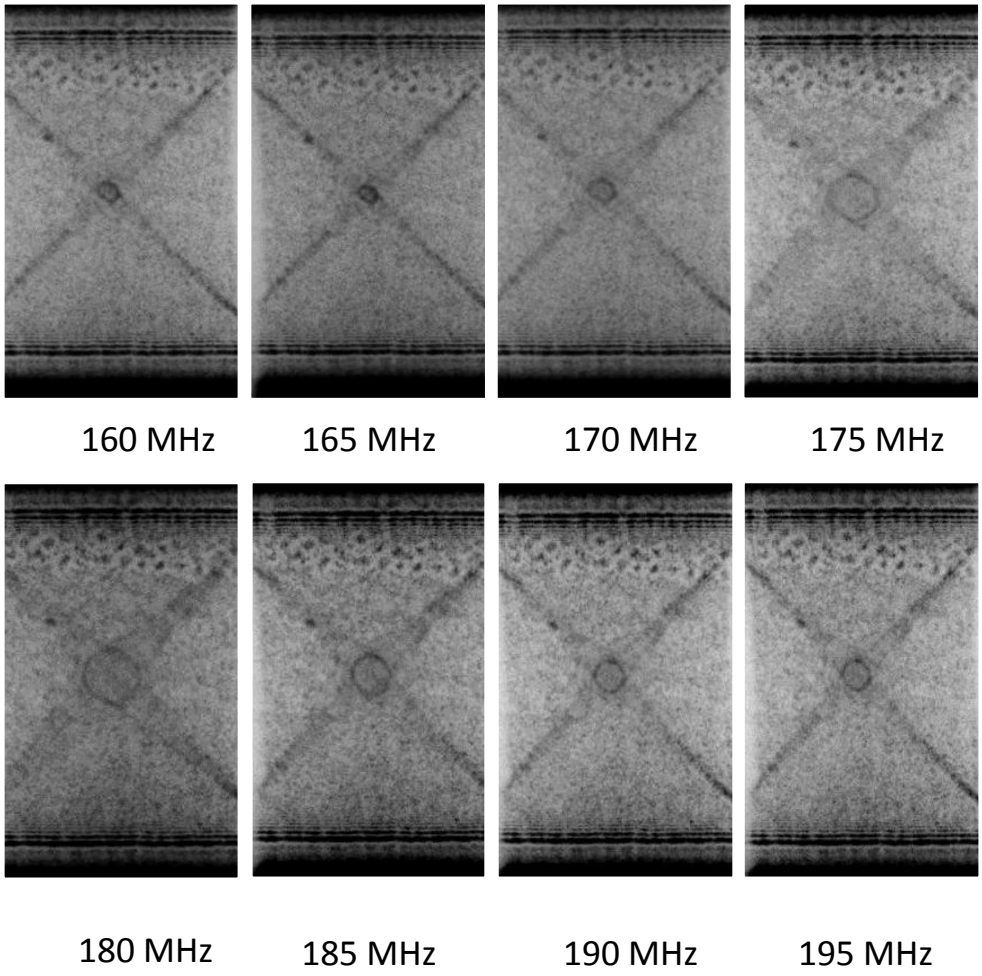

Figure 4.7 - Frequency sweep of a CCW magnetic vortex through resonance at $7.7 \times 10^{10} A/m^2$. The current is applied along the horizontal direction, at 5 μm defocus. The increase of orbit amplitude near resonance (approximately 180 MHz) is apparent.

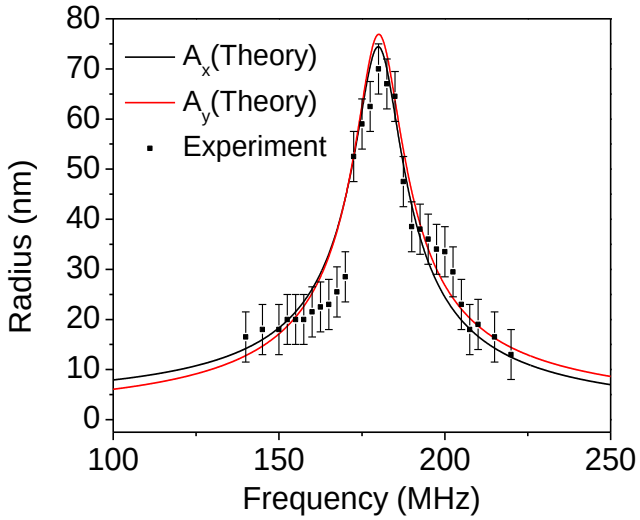

Figure 4.8 - Resonance curve for the sweep given in Fig. 4.7. The solid lines give fitted curves from the analytic model, which match well with experimental data. From here, the damping parameter may be extracted by the linewidth of the fitted curves. The jumps in amplitude from 0nm to approximately 15nm both before and after resonance is attributed depinning from local defects. Similarly, the jump from 30nm to 50nm is also attributed to defect pinning effects.

4.5 Determination of β

In structures exhibiting a magnetic vortex state, the displacement resulting from a spin polarized current is the result of both adiabatic and non-adiabatic contributions, as well as the Oersted field generated by the imbalanced current flow through the sample. In case of a DC current pulse, the adiabatic contribution results in displacement of the core along the direction of the current flow, while the non-adiabatic and Oersted field contributions are orthogonal to the current flow [72]. To separate the non-adiabatic and Oersted field contributions, vortex displacements of the vortex core for both chiralities may be utilized, as the non-adiabatic contributions will either add to Oersted field displacement or subtract from it, depending on the chirality and the nature of the imbalanced current flow. For the geometry used in our work, a CW chirality results in a larger displacement. This is schematically shown in Fig. 4.9.

In order to obtain our measurement for β, we carefully tuned the frequency over a range of 100MHz – 250MHz to obtain the largest amplitudes at multiple excitations currents. Currents were limited such that the orbits were large enough to overcome any obvious pinning effects, while being less than 6.5% of the total edge length of the structure in order to prevent non-linear effects. An example showing the size differences for CW and CCW orbits, taken at $1.0 \times 10^{11} A/m^2$, is shown in Fig. 4.10. The difference in orbit sizes is a result of the direction of the non-uniform current flow within the element. The larger CW orbit could indicate a greater current along the base of the element, although numerical simulations show a nearly uniform current flow in the horizontal plane and suggest that the Oersted field is actually a result of the vertical current flow at the sample edges.

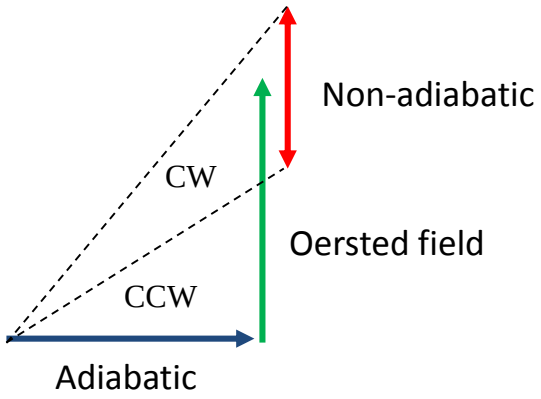

Figure 4.9 - Schematic showing how the three contributions to the vortex displacement add together. By looking at the two different chiralities, it is possible to separate the non-adiabatic and Oersted field contributions. The dashed lines show the total displacement for each chirality.

From the analytic model, it is apparent that the difference of the orbit amplitudes for CW and CCW chiralities squared is $A_{CW}^2 - A_{CCW}^2 \cong |D/G|(\tilde{H}\tilde{j}\beta/\Gamma)$, which depends on both H_0 and β, while $A_{CW}^2 + A_{CCW}^2 \cong (\tilde{H}^2 + \tilde{j}^2)/2\Gamma$, which only depends on H_0. Therefore the sum and differences of the resonant amplitudes squared can be used to extract both the Oersted field and non-adiabatic spin torque contributions to the resonant motion. To obtain a more accurate value, we extract these parameters from the slope of resonant amplitudes for both CW and CCW chiralities (Fig. 4.11). From the experimental results, and assuming a spin polarization of $P = 0.6$, we determine $\beta = 0.15 \pm 0.02 = (9.2 \pm 0.8)\alpha$. It must be noted that while this value of the polarization is a commonly used value for permalloy, there is some variation in experimental measurements [75–77]. Without any assumptions of the spin polarization, we may put a bound on the non-adiabatic spin torque over a range of polarizations, and this gives a minimum bound of $\beta = 7\alpha$ (Fig. 4.12). Furthermore, we find an Oersted field generated by the current to be equal to $H_0 = 1.66 \times 10^{-11} \pm 0.03 \times 10^{-11}$ Oe·m^2/A.

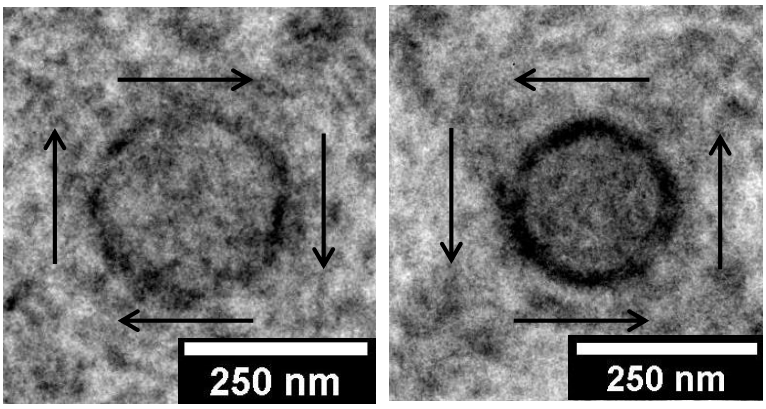

Figure 4.10 - Resonant orbits shown for both CW (left) and CCW (right) chiralities taken at a current density of $1.0 \times 10^{11} A/m^2$ and at 170MHz.

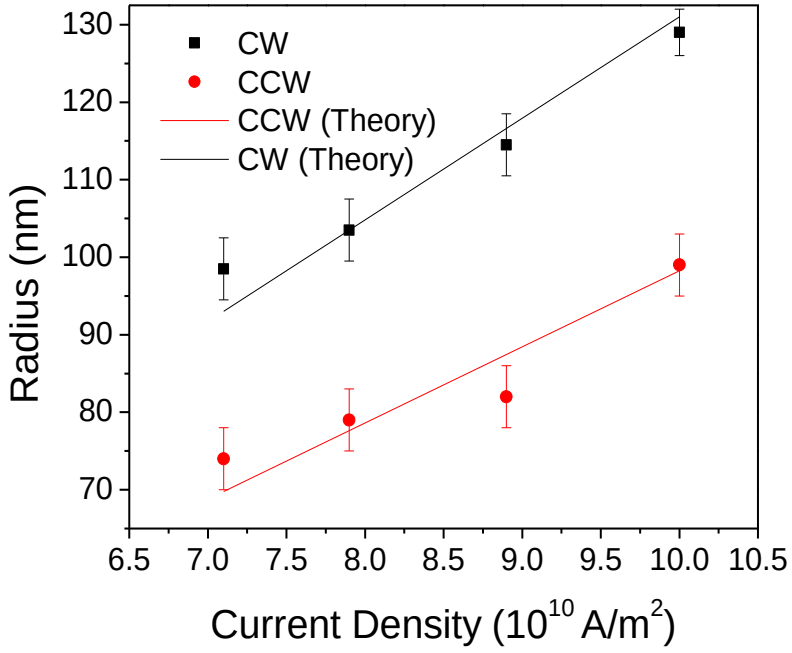

Figure 4.11 - Orbit amplitudes versus current density, with fitted lines determined from the analytic model.

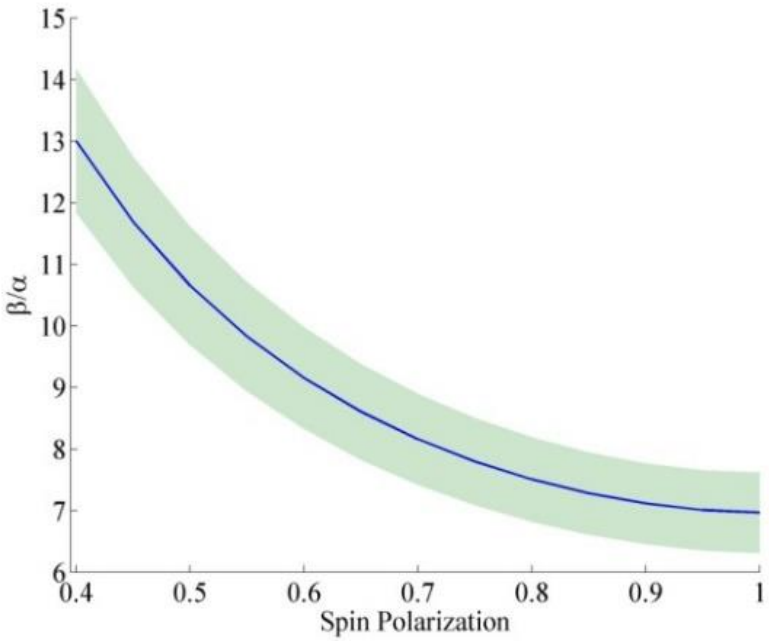

Figure 4.12 - Ratio of β over the full range of possible spin polarizations. A minimum of $P = 0.4$ is determined from the literature.

4.5 Off-resonance effects

An additional advantage of the high resolution afforded by in-situ TEM is the ability to probe the subtle changes in orbit behavior off resonance. As was previously mentioned, off-resonant orbits are elliptical, and the direction of the ellipticity will change depending on whether the frequency is above or below the resonance value. In purely field driven excitations, the tilt occurs such that the orbit is rotated 90 degrees at the crossover from over- to under-resonance. The addition of spin-transfer torque effects further complicates this matter, as they mix with the field effects, leading to off-axis rotations that vary with frequency. These effects have been imaged for the first time in TEM, shown in Fig. 4.13. Furthermore, we are able to compare these results to the analytic model, as shown in Fig. 4.14. The fits agree well with experimental values, and this is the first time models of off-resonance behavior have been validated in real systems. It should be further noted that while off-resonant effects are strongly influenced by defect pinning, in systems lacking pinning, it should be possible to determine the spin polarization directly from the tilt of the orbit as it is highly influenced by the degree of spin polarization.

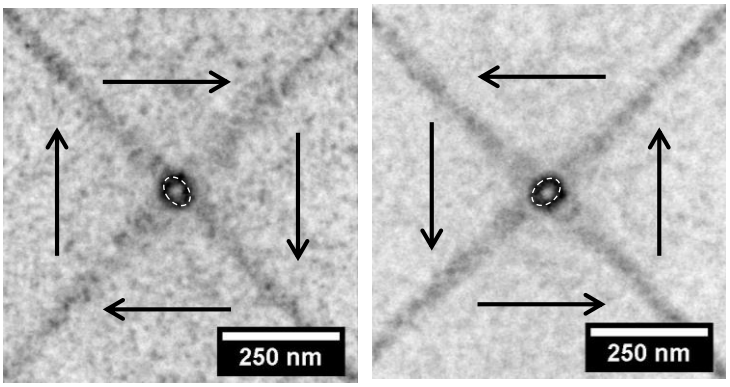

Figure 4.13 - Off resonant vortex orbits taken at a current density of $7.9 \times 10^{10} A/m^2$. The dashed line is a guide to the eye. Clearly different tilts are observed for the different chiralities, as predicted by micromagnetic simulations and the analytic model used in this work.

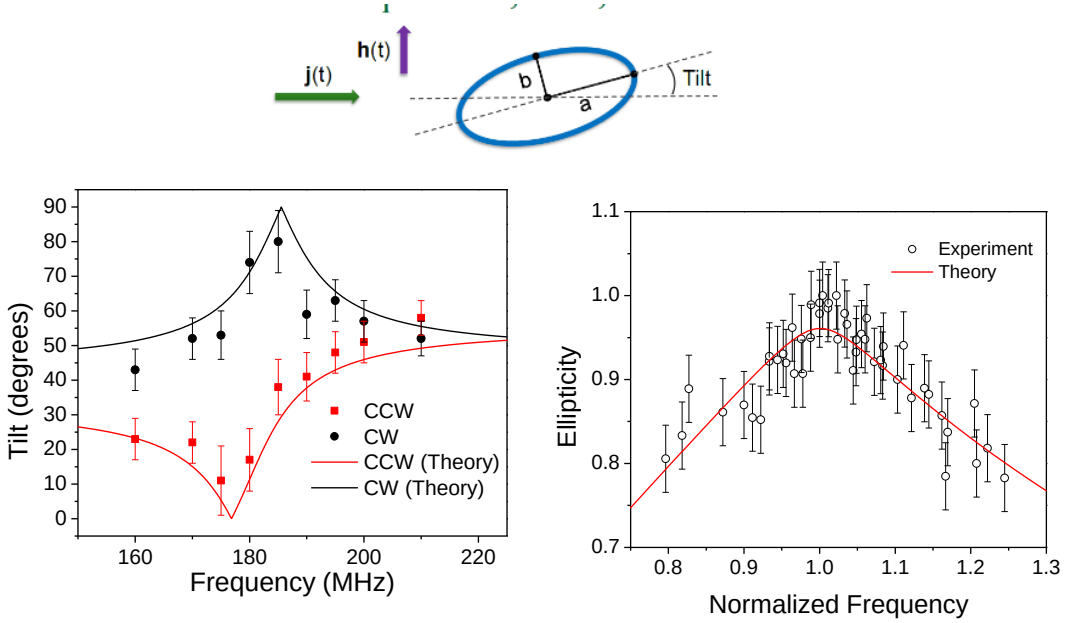

Figure 4.14 - Top: Tilt is defined as the tilt of the long axis away from the current flow direction. Bottom left: Tilt vs. frequency taken at $7.9 \times 10^{10} A/m^2$. Bottom right: Ellipticity vs. the normalized frequency.

4.6 Summary and future prospects

In summary, we utilized the spatial resolution afforded by TEM in combination with *in situ* dynamic vortex excitations to determine key parameters that determine both on-resonance and off-resonance magnetic vortex behavior. By determining the linewidth of the orbit, we measured the damping parameter independently of the non-adiabatic spin-torque parameter, β. β was measured by comparing the dissimilar vortex orbital amplitudes for CW and CCW chiralities at various current densities, and fitting the obtained data to an analytic model. Furthermore, the magnitude of the residual Oersted field associated with the imbalanced spin current was measured. This imbalance is found to be a result of vertical charge current flow at the sample edges, and should be contact pad geometry dependent. Off-resonant effects were measured for the first time as well. These effects included a tilt of the orbit as well as enhanced ellipticity, which becomes more significant the further the frequency is from resonance. By comparing the ellipticity and tilts to those predicted by analytic models, we were able to validate the models for off-resonant phenomena, something has been previously lacking.

Open questions remain, particularly pertaining to the unusually high value of α determined in this work. One possible cause could be from sample geometry, with enhanced damping being a result of spin wave excitation and reflection. Furthermore, it is possible that damping processes are fundamentally different for spin torque and Oersted field driven excitations, and this could be further explored using dynamic excitations in TEM. A further, more mundane explanation points towards defects leading to the appearance of increased damping.

In order to probe the scaling of non-adiabatic torques on the domain wall width, more work is also needed in structures with varying vortex sizes. Since the vortex core width is related to, among other things, the exchange length of a given material, by varying materials with different exchange lengths compared to that of Py, such as Co and CoFeB, additional light could be shed on this dependence.

Chapter 5. Dynamics of exchange coupled vortices in extended permalloy ellipses

5.1 Introduction to coupled vortex dynamics

5.1.1 Overview of coupling methods

One avenue currently being extensively researched for potential applications in devices ranging from low linewidth spin torque oscillators to magnetic based memory is that of coupled vortex systems. In these systems, the dynamics heavily influence the lineshape of the resonant orbit, as well as modify the resonance frequency. Understanding the details of these coupled dynamics are essential to the proper design of systems in which the coupling is tuned to produce a desired device functionality, but is also necessary for understanding the dynamics of densely packed vortex arrays, critical in a variety of systems, as vortex dynamics deviate from the typical models assuming single vortex motion or only weakly coupled dynamics.

The coupled behavior depends strongly on the exact mechanism of the coupling. Recently studied systems have focused on three primary means of achieving this – indirect exchange mediated by RKKY coupling across interfaces, dipolar coupling in which edge charges produce long range fields that couple spatially disparate vortex cores, and direct exchange coupling in systems where two vortices share an intermediary magnetic domain. These various methods relying on exchange coupling (indirect and direct) will be discussed briefly below.

5.1.2 Indirect exchange coupled vortex oscillations

Indirect exchange coupling occurs in multilayer magnetic materials in which a non-magnetic metal is sandwiched between two magnetic materials, and is mediated by the Ruderman-Kittel-Kasuya-Yosida (RKKY) interaction [78]. This interaction strength is material dependent but results in an effective oscillatory energy linking the magnetic states in two magnetic materials, and has been used extensively in giant magnetoresistance based devices. Typically, the strength of this interaction is measured with ferromagnetic resonance experiments. Depending on the non-magnetic spacer layer thickness, this coupling can be either ferromagnetic or antiferromagnetic, although strong antiferromagnetic coupling has only recently been observed in granular nanostructured materials, a result of the non-uniform crystal orientation, as well as structure and surface inhomogeneities. The strength of the interaction decays exponentially with the spacer thickness, and is therefore only relevant to spacer layers of up to a few nanometers (figure 5.1). However, this method of coupling has received a great deal of attention due to the fact that antiferromagnetic coupling in patterned materials with controllable shape anisotropy, in theory, can be used to nucleate and manipulate stable magnetic quasiparticles that are difficult to control in bulk systems such as skyrmions, magnetic bubbles, and merons. In these systems, dipole interactions must also be taken into account, and for larger spacer layers can completely dominate RKKY coupling.

For the strong coupling limit, the combination of dipole and RKKY interactions can result in linewidth narrowing in dual vortex systems as well as mode-locking vortices of dissimilar resonant modes into a single characteristic mode similar to that of a single layer film of equivalent thickness (figure 5.2), and could lead to the creation of magnetic vortex oscillators with tunable spectral characteristics that maintain rigidity in perpendicular structures [63].

While interlayer exchange coupling can be used to create strongly coupled vortex pairs, as well as allow for antiferromagnetic coupling, which is not possible with dipole or direct exchange coupling, it is also limited by the short range nature of the RKKY interaction.

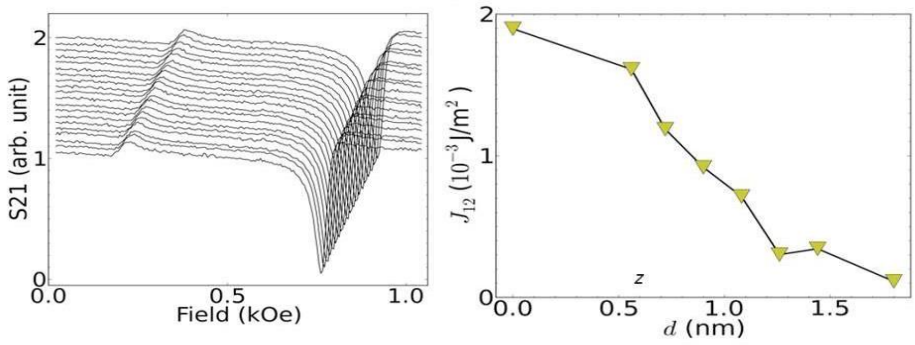

Figure 5.1 - Left: Typical FMR spectra for interlayer exchange coupled Py/Cu/Py films. Right: The extracted coupling strength vs. the Cu layer thickness. Beyond 1.5nm, the coupling is approximately 0.

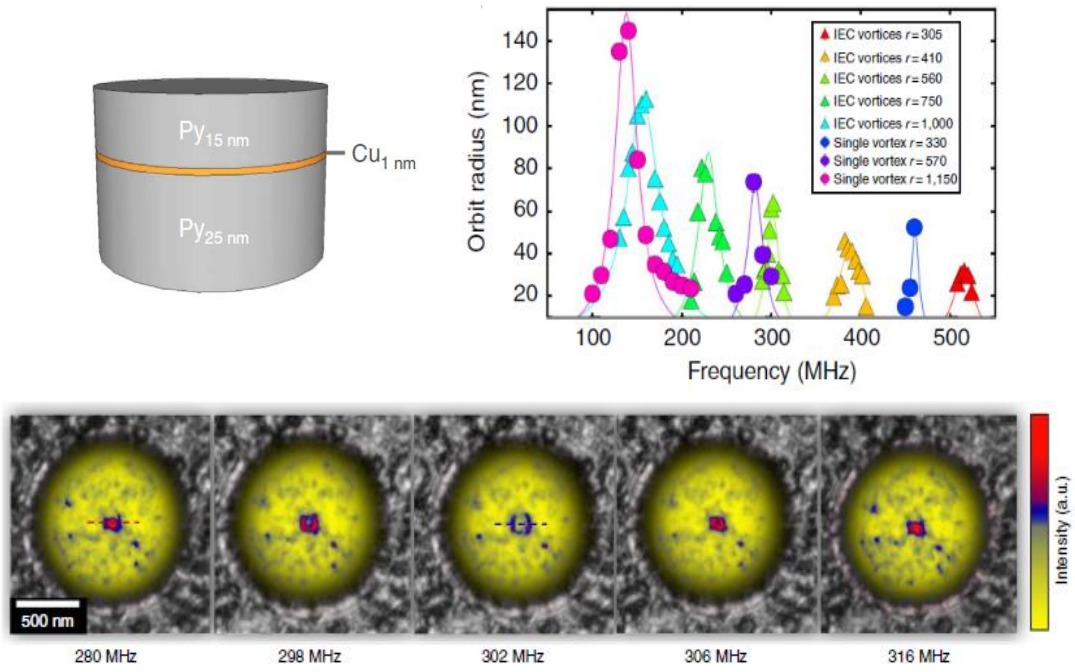

Figure 5.2 - Top left: Schematic of a typical RKKY coupled structure, showing two Py layers of different thickness and a 1nm Cu spacer. Top right: Orbit radius vs. Frequency for IEC coupled (triangles) and single vortex (circles) systems. Both systems show only one mode. The IEC system is slightly upshifted in frequency with a somewhat small amplitude. Bottom: Frequency sweep of a 560nm radius IEC system showing one peak centered at 302MHz.

5.1.3 Dipolar coupled vortex oscillations

In discs that are spatially separated by either vacuum or non-magnetic materials for distances much longer than the exchange length, coupling is most often mediated through long range dipolar interactions. Much work has focused on the coupling phenomena in disparate discs that are laterally separated, i.e. discs at the same height but with a narrow vacuum gap between them on the order of 100 nm [79–81]. Either a spin current is directly applied to one of the discs, or else a microwave stripline is placed over the top of the disc. When driven at resonance, both vortices are excited, one a direct result of either the driving field or current, and the other due to the creation of edge charges created by the displaced vortex, leading to a periodically oscillation dipole field that can excited the neighboring disc. Depending on the relative combination of chiralities and polarities, different frequency combinations can be generated, and mode splitting can occur. Such systems have been studied extensively for logic device applications, and recently, proof-of-concept devices have been fabricated and studied in a not-gate architecture [62].

5.1.3 Direct exchange coupled vortex oscillations

The role of direct exchange coupling of magnetic vortices has been demonstrated in extended permalloy elements, in which two vortices share a single, central magnetic domain [82–84]. When excited near resonance, this central domains size is changed as the vortices precess, and the change depends on the relative combination of the constituent vortices polarities, as the direction of the oscillations is polarity dependent, i.e. whether the vortex moves clockwise or counterclockwise when excited. Because this heavily modifies the local potential

landscape when excited, this leads to a mode splitting between the two states where $p_1 p_2 = -1 \; and \; p_1 p_2 = 1$, unlike in conventional single vortex states where the oscillation modes are degenerate. However, previous studies in these systems were limited to a very narrow response regime, for low in-plane applied fields. This coupling outside of this region will be discussed extensively in the following section.

5.2 Orbit deformations of exchange coupled magnetic vortices in extended Py discs

5.2.1 Motivation

Previous studies on the gyrotropic behavior of direct exchange coupled magnetic vortices have been limited to the linear field response regime, where the magnetic vortex positions, as well as magnetization, varies linearly with an applied field [82,83,85]. Furthermore, real space imaging of direct exchange coupled multi-vortex excitations has been lacking due to the limited resolution of available techniques. This section focuses on the behavior of such strongly coupled vortex pairs in permalloy ($Ni_{80}Fe_{20}$) mesoscopic discs in which the coupling energy becomes dominant and the vortex response to an increasing DC field is no longer linear. Understanding this regime is essential for the development of vortex based spintronic systems in which the ability to densely pack large sets of magnetic vortices imposes a limitation to the ultimate device density. By applying an in-situ field and directly imaging the response of magnetic vortices to both the static as well as an additional AC field, we find that two energetically degenerate pathways towards vortex annihilation exist, and that the vortex orbits are heavily influenced by the complex potential landscape. Lorentz TEM coupled with micromagnetic simulations allow us to study these orbits in real space, and link the vortex behavior to this landscape.

5.2.2 Experimental and simulation details

Extended permalloy discs ranging from (2μm - 3μm) x 1μm x 40nm were fabricated on top of 100nm thick Si_3N_4 membranes using standard electron beam lithography and deposition

techniques. For quasistatic reversal measurements, elements were deposited directly on top of the membrane. For dynamic measurements, first, 30nm Au striplines were deposited on the surface of the membranes, followed by patterning and deposition of the 40nm thick Py elements (Fig. 5.3). A 3nm Cr layer was deposited on the backside of the membrane to prevent charging. Simulations were carried out using 5nm x 5nm x 40nm cells on a 2μm x 1μm x 40nm Py rectangle using the standard material parameters for Py. For simulations of the hysteresis behavior, a damping of 0.5 was chosen, while for dynamic simulations, a value of 0.01 was chosen in order to accurately capture the dynamic response. For initial simulations, a two vortex state with $p_1 = p_2 = +1$ was seeded. Then a field was applied along the y-axis in increasing steps of 3 Oe until the magnetization was completely saturated along the y-axis. At each step, the magnetization configuration was saved to be used as input for the dynamic simulations. In order to determine the resonance frequency at various field values, the relaxed stable state was excited by a pulsed field. The frequency of the decayed magnetization oscillations was then identified as the resonance frequency. The disc was then excited by a 3Oe AC magnetic field set to this frequency. The steady state vortex oscillations were recorded and compared to experimental results.

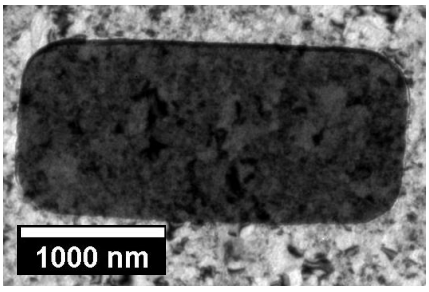

Figure 5.3 - In-focus image of a typical 40nm Py disc on top of a 30nm Au stripline for high frequency measurements.

5.2.3 Existence and mapping of degenerate annihilation pathways

In the system studied in this work, the central magnetization domain lies along the positive y direction. Due to the residual out-of-plane field in the microscope, both vortex polarities are fixed with $p_1 = p_2 = +1$. When a field is applied antiparallel to the central domain, the magnetization response can be broken into three regions. First, the magnetization in the y-direction follows the field. This is the result of a shrinking of the central domain, in which the magnetic vortex separation along the long axis of the structure decreases and the coupling increases. The response of M_y is approximately linear with the field, and no noticeable change in M_x occurs. As the vortices are displaced closer together, the central domain size further shrinks, and the change in energy accelerates. At large enough fields, the response is no long linear with field, and the vortices move off-axis in order to minimize further increases in the energy. This leads to a tilting of the magnetization and an increase in $|M_x|$, in addition to a continued change in M_y along the field direction, albeit at a different slope. Finally, vortex annihilation at the edges occurs and an s-state is present before complete transformation into a single domain state along the field direction (figure 5.4). During the second stage, due to the symmetric energy landscape of system, two energetically degenerate vortex annihilations pathways exist, which lead to diverging values of M_x depending on which pathway is followed. These stable pathways were mapped using micromagnetic simulations (figure 5.5) and experimentally verified in Lorentz TEM. In order to observe both stable vortex states for a given H_y, a 2um x 1um x 40nm thick permalloy rectangle was fabricated on an electron transparent Si_3N_4 membrane and imaged in a JEOL 3000F TEM with a calibrated out-of-plane magnetic field in the specimen area. The sample was then tilted about the y-axis within the field in order to apply a field along the y-

direction and obtain states in which the vortices were moved off-axis. While the specific annihilation pathway of the vortex depends on the local microstructure in the vicinity of the transition from linear to non-linear response fields, a small field along the x-direction was able to drive the vortex between degenerate pathways. Following application of the in-plane field, it is removed by removing the residual tilt along the x-axis. Both vortex configurations shown in figure 5.6 are without an applied field along the elements long axis, demonstrating the ability to controllably access both ground states. The off axis motion of the core with increasing field is a direct result of the increasing energy associated with further decreases in separation of the vortices beyond the linear field limit. The region where the energy penalty increases and results in the off-axis motion is immediately at the transition from linear to non-linear field response.

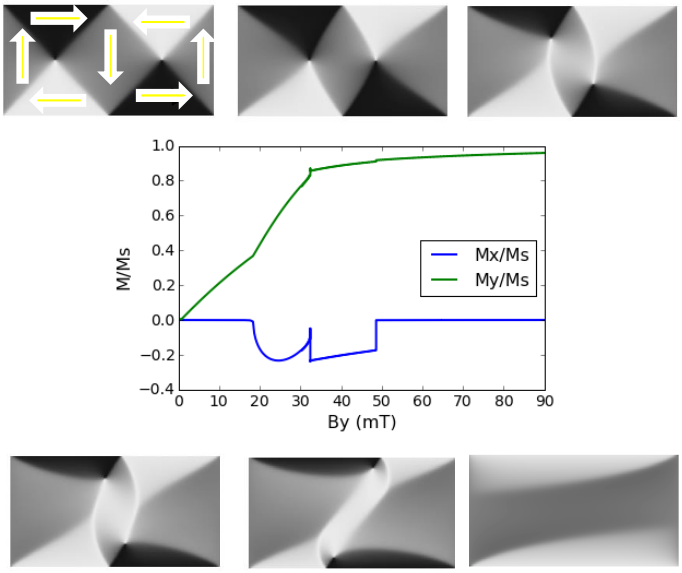

Figure 5.4 - Simulated magnetization response to an applied field antiparallel to the central domain. The simulated profiles show the x-component of the magnetization as the in-plane field is increased anti-parallel to the central domain.

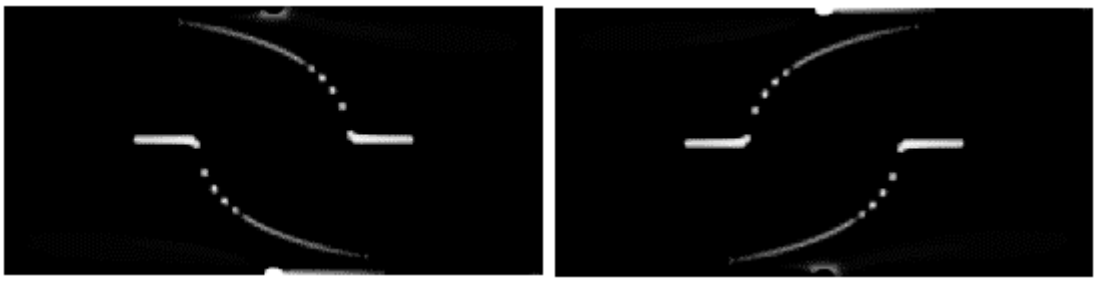

Figure 5.5 - Degenerate annihilation pathways traced for a 2.0μm x 1μm x 40nm Py structure calculated via micromagnetics. The color indicates the z-component of the magnetization, with white indicated a larger positive value, and black being 0.

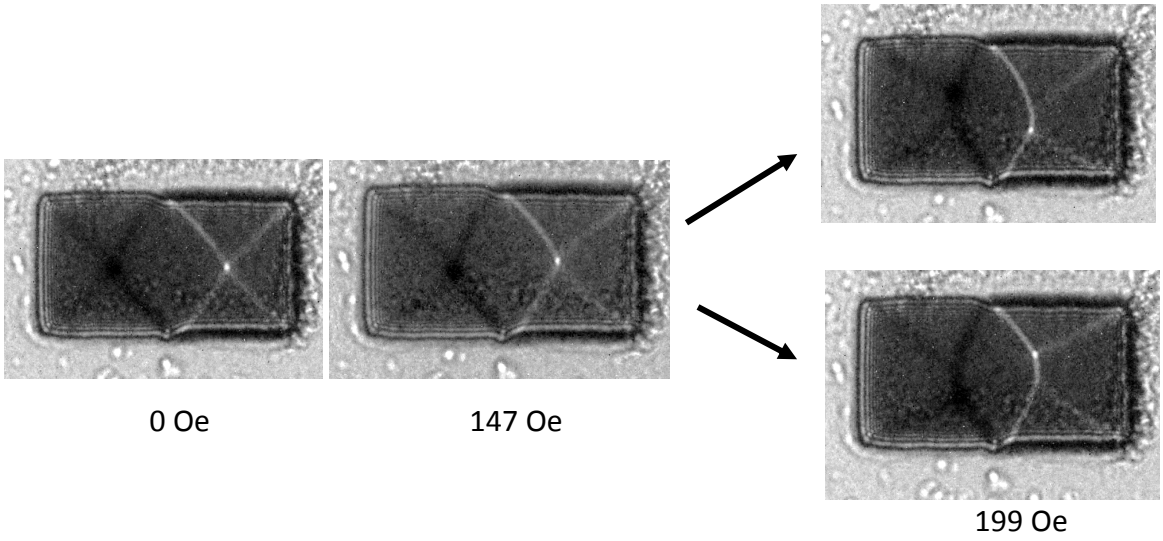

Figure 5.6 - Lorentz images showing the magnetic configuration for 3 different applied field values. The images on the right show the degenerate pathways for the same disc under the same applied field, after application of a small x-field is applied to the top image. The field is then removed, and only the field in the y-direction remained, indicating that both core locations are stable.

5.2.4 Real space dynamics of vortex pairs

When a magnetic state lying along one of the points of the hysteresis loop is perturbed by a small field pulse, both vortices begin to oscillate about the equilibrium position. For this system, with both polarities being equal, the oscillations occur in the same direction, but 180

degrees out of phase. When the vortices are separated by large spatial differences, the effect of their coupling, and mutual oscillations, does not play a significant role. When the spacing decreases, however, the coupling will have profound influences on the vortex dynamics. As the vortices move closer together, small changes in vortex positions lead to larger changes in the system energy associated with further displacement towards each other. This is also the cause of the off-center vortex motion seen during reversal.

At zero applied field, the vortices lie approximately one fourth of the structure length from the short edges. The vortex oscillations at resonance are elliptical, with larger oscillations along the short axis direction, and smaller along the long axis. This is a result of the local confining potential due to the shared central domain. Similar behavior is observed in micromagnetic calculations, shown in figure 5.7.

Following observations at zero field, the sample was tilted such that the core was displaced towards the sample edge (figure 5.7). It is known from previous work in uncoupled systems that a vortex displaced towards the edge will tend to follow an orbit shaped similarly to the edge structure [86,87]. This is a result of the local potential no longer being a simple harmonic potential, but further requiring care to be taking in accounting for higher order contributions. In this case, the orbit may be slightly asymmetric, with the side closer to the edge being slightly flatter than the side closer to the interior of the structure. Simulations also indicated that oscillations in M_x decrease as the core approaches the edge of the structure. This behavior is qualitatively confirmed experimentally.

Finally, when the field is applied opposite the central domain, the central domain shrinks, and the cores move together. As the core approaches the non-linear response regime, the potential can no longer be described as harmonic or quartic as is the case in edge potentials.

While there is little net change to oscillations about the short axis direction, oscillations in M_y change drastically. When the core approaches the transition from linear to non-linear regimes, the side of the core closest to center of the element encounters a sharp potential that is significantly larger than the vortex energy. This leads to a flat vortex oscillation on the side of the boundary. Meanwhile, the opposite side of the orbit still appears as is typically expected for periodic vortex motion, indicative of the rapidly changing potential near the transition regime. This is the first observation of stable vortex dynamics in which the orbit can no longer able to be described by a simple combination of harmonic and quartic potentials. After application of a 194 Oe field, the inner vortex edge is no longer flat. Instead the M_x oscillations are larger than in the 0 field case, and it follows a curved, non-uniform trajectory (figure 5.8). In order to explain this, micromagnetic simulations were run with the vortex displaced just beyond the onset of the non-linear field regime. We find that this behavior can be explained by the existence of degenerate annihilation pathways. For large enough excitations, the vortex is driven between the degenerate paths. This results in a curved trajectory similar to that seen in experiment. It should be noted that for large core displacements, while qualitative aspects of the vortex path are in agreement with experiment, the orbits predicted by micromagnetics exhibit much smaller oscillations away from the sharp inner potential.

Further vortex displacement leads to the vortex moving along one of the degenerate pathways (figure 5.9). At this point, the orbit size dramatically shrinks, and it tilts off axis. The region in the center is clearly energetically inaccessible, as evidenced by the sharp flatting of the orbit along the inner path. The outside still maintains the expected elliptical trajectory. Further displacements lead to annihilation of the vortex, and no more useful information can be obtained from the resonance experiments.

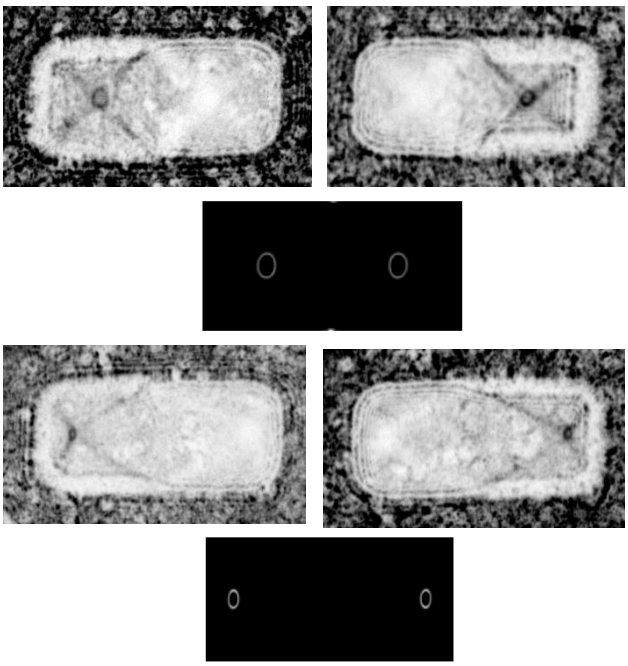

Figure 5.7 – Top: Vortex oscillations shown for no in-plane field. Bottom: Vortex oscillations with a field applied parallel to the central domain such that both cores are displaced towards the disc boundary. Simulated trajectories are also shown.

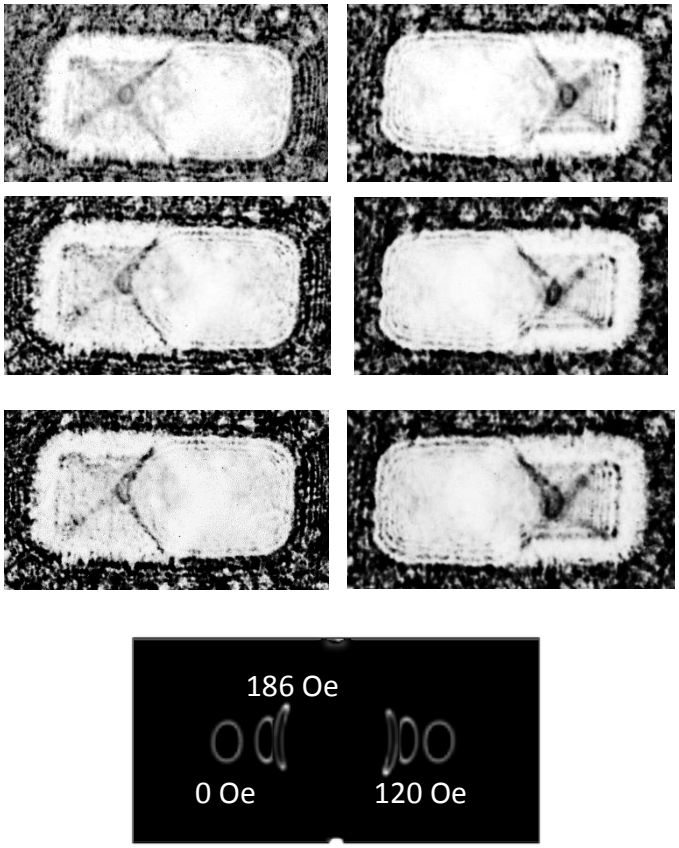

Figure 5.8 – Top: Experimental images corresponding to applied fields of 73 Oe, 152, and 176 Oe showing changes to the vortex orbit. Bottom: Simulated core trajectories at the indicated fields.

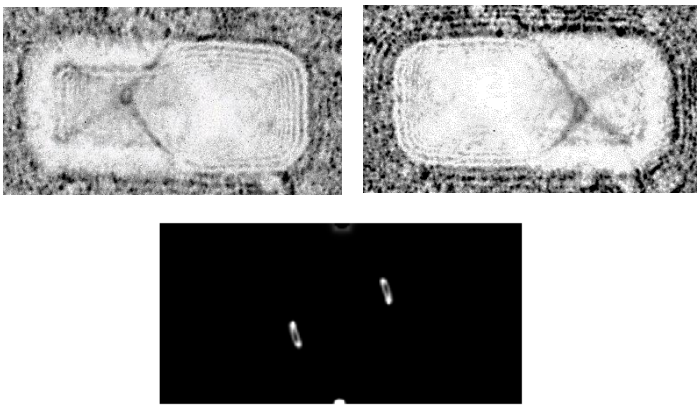

Figure 5.9 – Top: Off axis orbits taken at 207 Oe. Bottom: Simulated trajectories at a 195 Oe applied field.

5.2.5 Discussion

When the magnetic vortices in exchange coupled systems are displaced such that the separation between them remains large, the typical elliptical trajectories are observed, i.e. for no displacement at equilibrium. Furthermore, the vortex orbit decreases and is compressed at sample boundaries, in good agreement with previous studies that the potential is quartic near structure edges. However, when the separation is decreased by introduction of an in-plane field such that the coupling strength is enhanced, the coupling heavily influences the vortex behavior. At the transition region where the static vortex response transitions from linear to non-linear, these changes result in very different dynamic behavior on each side of the transition. Immediately before the transition, a hard potential results in a flat orbit edge on the inner boundary. Immediately following the transition, the vortex orbit is highly non-linear, with a concave inner vortex edge and enhanced oscillations along M_x. This behavior is explained by resonant driving between the two energetically equivalent ground states observed in the static reversal measurements. Further vortex displacements result in tilted orbits with a flat inner edge and a significantly decreased orbit amplitude, a result of the hard inner boundary discussed previously.

5.2.6 Summary

This work demonstrates the non-linear effects on vortex orbits directly relating to the strongly anharmonic potentials present in direct exchange coupled multi-vortex systems through the use of experimental observations with Lorentz TEM and micromagnetic simulations. Furthermore, resonance excitation was used to drive magnetic vortices between spatially separated ground states in order to amplify vortex oscillations and has been observed experimentally for the first time. The understanding of the large changes in orbit shape and size resulting from coupling could prove important in the development of memory or logic devices which rely on multi-vortex interactions, or in arrays where magnetic vortices are densely packed

Chapter 6. Conclusion

6.1 Synopsis

In this thesis, the ordering processes and magnetization dynamics within patterned nano-magnetic elements were studied using TEM techniques such that the local behavior of the magnetic structure could be studied in real space with high spatial resolution. This work focused on two systems – artificial spin ices, and magnetic vortices in both coupled and uncoupled geometries.

In the artificial square spin ice systems, it was found that the switching process begins with the nucleation and subsequent propagation of ice rule violating defects within the lattice. The defect interactions play a key role in the development of ordering within the system. Statistical analysis of defect populations and system correlations showed the emergence of a highly frustrated state for low magnetizations with only local ground state correlations. This state is explained via a strong influence of charge ordering, which ultimately limits the maximum defect density within the lattice during a reversal cycle. By comparing experimental results with numerical simulations based on a point dipole model, it was found that the system can successfully be modeled as an array of dipolarly interacting Ising spins. Furthermore, a new, simple method to achieve a high degree of local ground state ordering was proposed by simply applying a decaying AC field along the (11) symmetry axis of the system.

Further work clarified the role of non-adiabatic spin torque in resonant excitations of magnetic vortex cores as well as measured the magnitude of this effect with the greatest

precision to date. By using a newly designed TEM sample holder, it was possible to directly apply sub-GHz excitations, *in situ*, and determine the vortex response to spin polarized currents tuned to the vortex resonance mode. By fitting the linewidth of the vortex orbit to numerical models, the damping parameter was determined to be $\alpha = 0.016$. Furthermore, the orbit amplitude for clockwise and counterclockwise chiralities was found to be significantly different at resonance. This is a due to the fact that the non-adiabatic torque will add to Oersted field contributions in the case of a CW trajectory, while subtracting from Oersted contributions in a CCW trajectory. By comparing the amplitude at resonance for both chiralities at identical current densities, and fitting to the analytic model with an assumed spin polarization of $P = 0.06$, the Oersted field resulting from the imbalanced current flow was found to be $H_0 = 1.66 \times 10^{-11} \pm 0.03 \times 10^{-11}$ Oe·m^2/A, while the non-adiabatic spin torque parameter was found to be $\beta = 0.15 \pm 0.02 = (9.2 \pm 0.8)\alpha$. Furthermore, even without any assumptions of the spin polarization, a firm lower bound of $\beta = 7\alpha$ can be set. Finally, off-resonance effects were measured for the first time, and an elliptical, off-axis orbit was found, with both the ellipticity and axial tilt varying with frequency. These results, along with full 3D micromagnetic calculations, were used to verify the validity of the analytic model for dynamic vortex trajectories.

Finally, the effect of direct exchange coupling of neighboring magnetic vortices on both the reversal behavior and resonant dynamics in multi-vortex systems was studied via a combination of direct imaging using Lorentz TEM and time resolved micromagnetic calculations. In the dual vortex coupled system, it was found that the coupling leads to degenerate annihilation pathways when a field is applied anti-parallel to the shared domain such that the magnetization response is no longer linear. These pathways are characterized by off-axis

vortex motion. This process is a result of a minimization of the exchange penalty associated with further vortex displacements. Furthermore, deformations in vortex orbits give insight into the local energy landscape. At structure edges, the vortex behavior is as expected from previous works. However, in the non-linear displacement regime, the orbits become flat on one side before moving off-axis. This cannot be explained by the simple model used for edge potentials, and indicates the presence of an energetically inaccessible region. Furthermore, once off axis, resonance may drive the vortex between degenerate ground states, and this is observed experimentally and confirmed with micromagnetic calculations. If the driving field is below that required to drive the vortex between ground states, a flat inner orbit edge is seen. This flattened edge can be used to directly map regions that are energetically inaccessible to the vortex core. Results of interlayer exchange coupled vortices were also presented.

6.2 Future outlook

As the integration of spin based technologies into commercial devices becomes increasingly common, new methods for control of the fundamental magnetic elements composing them will need to be developed to overcome the fundamental limitations imposed by current methods, i.e. Oersted field based. The use of spin-transfer torque currently shows a great deal of promise, but is fundamentally hampered by the high current densities necessary to drive significant changes in magnetic structure which results in high power use and generation of heat. To overcome this, methods based on electric field control without direct current flow are the subject of intense study, but are relatively new and poorly understood.

The most well understood of these electric field based techniques is the use of multiferroic heterostructures, consisting of a magneto-elastic surface layer on-top of a ferroelectric substrate. The magneto-elastic layer responds to strain generated by changes in the ferroelectric under-layer. For materials such as PMN-PT and PZT, which can produce extremely large strains when exposed to electric fields, this can result in a rotation of the magnetization in a magnetic thin film [88]. The effects are even more profound in patterned nanomagnets, in which the domain structure can be controllably modified and, in single domain magnets, reversibly switched. Furthermore, it has been found that in various ferroelectric structures exhibiting stripe domain structures, the ferroelectric domain structure can be imprinted in the magnetic structure, and could prove useful in the creation of artificial magnonic crystals with tunable properties.

Other techniques rely on the generation of pure spin currents, in which the transfer of spin angular momenta is transported typically by magnons, and no charge current is necessary.

These effects include the Spin Hall, Rashba, and Spin Seebeck effect. These techniques, although in their infancy, potentially could lead to current free manipulation of magnetic materials. Coupling the Spin Seebeck Effect in a magnetic material to a non-magnetic material with large spin orbit coupling, such as platinum, could also be used to generate power, although at the current time this effect is much too weak to be integrated into real devices.

Furthermore, as devices are continually miniaturized, measurement techniques capable of detecting small, dynamic changes in magnetization states are necessary. With arguably the best current spatial resolution, TEM is one of the most promising techniques. However, it is hampered by fundamental limits of current microscopes. Possibly the most important of these limitations are the sample requirements, the time resolution, and the projection problem, the result of the fact that TEM is a transmission technique and results in an averaged view of a three dimensional structure. While the sample requirements cannot be changed, clever design of samples and specimen holders can alleviate some of this issue. On the other hand, the projection problem and temporal limitations require modifications to the imaging process or microscope design.

In order to obtain structural information of three dimensional structures, tomography is often used in which a tilt series of images is taken, and then alignment and reconstruction of the images can be used to obtain a 3D map of the system of interest. At this point, standard tomography in TEM is well developed and in common use [89]. Phase reconstruction tomography, in which the magnetic induction is mapped in three dimensions, is only beginning to achieve functional use. The basic idea is to combine either electron holography or TIE and regular tomography concepts to reconstruct the 3D phase map. However, this is a complicated endeavor, mainly a because the image alignment issues associated with standard TIE and

electron holography are amplified in the case where many additional images are needed at different tilt angles. First results from this technique has been demonstrated within the last few years, but the ultimate level of precision obtainable is still in doubt [90].

Temporally resolved dynamics are another area in which TEM is lacking in current capabilities. Large efforts are focused on overcoming this limitation. In the majority of TEM's, the limitations are related to the speed of the detector, most often a CCD. A CCD is based on charge accumulation and amplification, and is a relatively slow process compared to photodiode methods used in photon based techniques such as full field XMCD and MOKE. To circumvent this issue in TEM, a few different methods are being developed. The method most widely used is the stroboscopic pump-probe technique. A laser is used to activate a photocathode, and is timed with a periodic excitation. The constraint is that the process needs to be repeatable, with many laser pulse/excitation processes performed in order to obtain sufficient contrast, but this method does allow time resolutions limited by the electronics and laser pulse length, which can be less than a picosecond, while maintaining a high spatial resolution. The second technique is based on a single shot approach. In this approach, a specified delay time between a laser excitation and the specified sample excitation is set. The laser pulse is used to produce a very large number of electrons per pulse, orders of magnitudes more than in the stroboscopic approach. In this way, non-repeatable processes may be studied in a truly dynamic manner. One example of such a microscope, the so called "Dynamic TEM," can be found at Lawrence Livermore National Laboratory, which can produce images at around 20nm spatial resolution with 15ns time resolution [91]. Recently, the first Lorentz images were taken using dynamic TEM methods using an instrument at the California Institute of Technology, showing the propagation of a magnetic domain wall after depinning due to application of an Oersted

field [92]. It should be noted, however, that the magnetic imaging resolution was significantly lower than the 20nm spatial resolution that is typical for in-focus images, and much work still needs to be done.

Other techniques are also being further developed in which dynamic processes may be studied with high spatial resolution. Perhaps most common, XMCD in a pump-probe set-up has been used to study a variety of dynamic processes with time resolutions significantly faster than any conventional TEM techniques, limited by the incident photon bunch width [93]. It also has the advantage that it allows for element specific imaging. However, the spatial resolution is still limited to less than that of current dynamic TEM techniques. In the end, it is apparent that there may not be only one technique that is capable of fulfilling all requirements necessary to fully understand spin behavior at the nanoscale, and continued development in instrumentation, across multiple techniques, will be required to continue advancing our understanding of complex spin systems.

Bibliography

[1] M. N. Baibich, J. M. Broto, A. Fert, F. N. Van Dau, and F. Petroff, Phys. Rev. Lett. **61**, 2472 (1988).

[2] G. Binasch, P. Grünberg, F. Saurenbach, and W. Zinn, Phys. Rev. B **39**, 4828 (1989).

[3] T. Shinjo, Science (80-.). **289**, 930 (2000).

[4] Y. Aharonov and D. Bohm, Phys. Rev. **115**, 485 (1959).

[5] A. K. Petford-Long and M. De Graef, in *Charact. Mater.* (John Wiley & Sons, Inc., 2002).

[6] V. Volkov and Y. Zhu, Ultramicroscopy **98**, 271 (2004).

[7] M. Beleggia, M. A. Schofield, V. V Volkov, and Y. Zhu, Ultramicroscopy **102**, 37 (2004).

[8] S. Pollard, V. Volkov, and Y. Zhu, Phys. Rev. B **85**, 1 (2012).

[9] M. Malac, M. Beleggia, M. Kawasaki, P. Li, and R. F. Egerton, Ultramicroscopy **118**, 77 (2012).

[10] M. Malac, M. Beleggia, R. Egerton, and Y. Zhu, Ultramicroscopy **108**, 126 (2008).

[11] S. Pollard, M. Malac, M. Beleggia, M. Kawasaki, and Y. Zhu, Appl. Phys. Lett. **102**, 192401 (2013).

[12] V. V Volkov, D. C. Crew, Y. Zhu, and L. H. Lewis, Rev. Sci. Instrum. **73**, 2298 (2002).

[13] P. Rai-Choudhury, *Handbook of Microlithography, Micromachining, and Microfabrication: Microlithography* (IET, 1997).

[14] A. Tonomura, *Electron Holography*, 2nd ed. (1999), pp. 55–59.

[15] C. N. Yang and R. L. Mills, Phys. Rev. **96**, 191 (1954).

[16] A. Tonomura, Rev. Mod. Phys. **59**, 639 (1987).

[17] P. J. Grundy and R. S. Tebble, Adv. Phys. **17**, 153 (1968).

[18] S. D. Pollard and Y. Zhu, Microscopy **62 Suppl 1**, S55 (2013).

[19] W. E. and R. E. Siday, Proc. Phys. Soc. Sect. B **62**, 8 (1949).

[20] C. G. Kuper, Phys. Lett. A **79**, 413 (1980).

[21] P. Bocchieri, A. Loinger, and G. Siragusa, Nuovo Cim. A **51**, 1 (1979).

[22] P. Bocchieri and A. Loinger, Nuovo Cim. A **47**, 475 (1978).

[23] S. M. Roy, Phys. Rev. Lett. **44**, 111 (1980).

[24] A. Tonomura, N. Osakabe, T. Matsuda, T. Kawasaki, J. Endo, S. Yano, and H. Yamada, Phys. Rev. Lett. **56**, 792 (1986).

[25] P. A. M. Dirac, Proc. R. Soc. London. Ser. A **133** , 60 (1931).

[26] P. A. M. Dirac, Phys. Rev. **74**, 817 (1948).

[27] K. A. Milton, Reports Prog. Phys. **69**, 1637 (2006).

[28] M. B. and G. G. and M. R. M. and B. P. and L. P. and F. P. and P. S.-L. and G. S. and M. S. and V. T. and S. Zucchelli, EPL (Europhysics Lett. **12**, 613 (1990).

[29] L. D. C. Jaubert and P. C. W. Holdsworth, Nat Phys **5**, 258 (2009).

[30] T. Fennell, P. P. Deen, a R. Wildes, K. Schmalzl, D. Prabhakaran, a T. Boothroyd, R. J. Aldus, D. F. McMorrow, and S. T. Bramwell, Science **326**, 415 (2009).

[31] C. Castelnovo, R. Moessner, and S. L. Sondhi, Nature **451**, 42 (2008).

[32] S. T. Bramwell, S. R. Giblin, S. Calder, R. Aldus, D. Prabhakaran, and T. Fennell, Nature **461**, 956 (2009).

[33] D. J. P. Morris, D. a Tennant, S. a Grigera, B. Klemke, C. Castelnovo, R. Moessner, C. Czternasty, M. Meissner, K. C. Rule, J.-U. Hoffmann, K. Kiefer, S. Gerischer, D. Slobinsky, and R. S. Perry, Science **326**, 411 (2009).

[34] C. Castelnovo, R. Moessner, and S. L. Sondhi, Annu. Rev. Condens. Matter Phys. **3**, 35 (2012).

[35] R. F. Wang, C. Nisoli, R. S. Freitas, J. Li, W. McConville, B. J. Cooley, M. S. Lund, N. Samarth, C. Leighton, V. H. Crespi, and P. Schiffer, Nature **439**, 303 (2006).

[36] Y. Qi, T. Brintlinger, and J. Cumings, Phys. Rev. B **77**, 94418 (2008).

[37] Z. Budrikis, J. P. Morgan, J. Akerman, A. Stein, P. Politi, S. Langridge, C. H. Marrows, and R. L. Stamps, Phys. Rev. Lett. **109**, 37203 (2012).

[38] Z. Budrikis, P. Politi, and R. L. Stamps, Phys. Rev. Lett. **107**, 217204 (2011).

[39] S. A. Daunheimer, O. Petrova, O. Tchernyshyov, and J. Cumings, Phys. Rev. Lett. **107**, 167201 (2011).

[40] J. P. Morgan, J. Akerman, A. Stein, C. Phatak, R. M. L. Evans, S. Langridge, and C. H. Marrows, Phys. Rev. B **87**, 24405 (2013).

[41] A. Schumann, B. Sothmann, P. Szary, and H. Zabel, Appl. Phys. Lett. **97**, 22503 (2010).

[42] J. P. Morgan, A. Stein, S. Langridge, and C. H. Marrows, Nat Phys **7**, 75 (2011).

[43] U. B. Arnalds, A. Farhan, R. V Chopdekar, V. Kapaklis, A. Balan, E. T. Papaioannou, M. Ahlberg, F. Nolting, L. J. Heyderman, and B. Hjorvarsson, Appl. Phys. Lett. **101**, 112404 (2012).

[44] S. Ladak, D. E. Read, G. K. Perkins, L. F. Cohen, and W. R. Branford, Nat Phys **6**, 359 (2010).

[45] E. Mengotti, L. J. Heyderman, A. F. Rodriguez, F. Nolting, R. V Hugli, and H.-B. Braun, Nat Phys **7**, 68 (2011).

[46] C. Phatak, A. K. Petford-Long, O. Heinonen, M. Tanase, and M. De Graef, Phys. Rev. B **83**, 174431 (2011).

[47] S. D. Pollard, V. Volkov, and Y. Zhu, Phys. Rev. B **85**, 180402 (2012).

[48] L. A. S. Mól, W. A. Moura-Melo, and A. R. Pereira, Phys. Rev. B **82**, 54434 (2010).

[49] Z. Budrikis, P. Politi, and R. L. Stamps, Phys. Rev. Lett. **105**, 17201 (2010).

[50] G. S. D. Beach, M. Tsoi, and J. L. Erskine, J. Magn. Magn. Mater. **320**, 1272 (2008).

[51] D. C. Ralph and M. D. Stiles, J. Magn. Magn. Mater. **320**, 1190 (2008).

[52] L. Heyne, J. Rhensius, D. Ilgaz, A. Bisig, U. Rüdiger, M. Kläui, L. Joly, F. Nolting, L. J. Heyderman, J. U. Thiele, and F. Kronast, Phys. Rev. Lett. **105**, 187203 (2010).

[53] E. R. Lewis, D. Petit, L. O'Brien, A. Fernandez-Pacheco, J. Sampaio, A.-V. Jausovec, H. T. Zeng, D. E. Read, and R. P. Cowburn, Nat. Mater. **9**, 980 (2010).

[54] I. M. Miron, T. Moore, H. Szambolics, L. D. Buda-Prejbeanu, S. Auffret, B. Rodmacq, S. Pizzini, J. Vogel, M. Bonfim, A. Schuhl, and G. Gaudin, Nat. Mater. **10**, 419 (2011).

[55] Y. Tserkovnyak, A. Brataas, and G. E. W. Bauer, J. Magn. Magn. Mater. **320**, 1282 (2008).

[56] G. Meier, M. Bolte, R. Eiselt, B. Krüger, D.-H. Kim, and P. Fischer, Phys. Rev. Lett. **98**, 187202 (2007).

[57] E. Martinez, L. Lopez-Diaz, O. Alejos, and L. Torres, Phys. Rev. B **77**, 144417 (2008).

[58] J. Leliaert, B. Van de Wiele, A. Vansteenkiste, L. Laurson, G. Durin, L. Dupré, and B. Van Waeyenberge, J. Appl. Phys. **115**, 17D102 (2014).

[59] J. Leliaert, B. Van de Wiele, A. Vansteenkiste, L. Laurson, G. Durin, L. Dupré, and B. Van Waeyenberge, Phys. Rev. B **89**, 064419 (2014).

[60] J. Leliaert, B. Van de Wiele, A. Vansteenkiste, L. Laurson, G. Durin, L. Dupré, and B. Van Waeyenberge, J. Appl. Phys. **115**, 233903 (2014).

[61] H. Jung, Y.-S. Choi, K.-S. Lee, D.-S. Han, Y.-S. Yu, M.-Y. Im, P. Fischer, and S.-K. Kim, ACS Nano **6**, 3712 (2012).

[62] H. Jung, K.-S. Lee, D.-E. Jeong, Y.-S. Choi, Y.-S. Yu, D.-S. Han, A. Vogel, L. Bocklage, G. Meier, M.-Y. Im, P. Fischer, and S.-K. Kim, Sci. Rep. **1**, 59 (2011).

[63] J. F. Pulecio, P. Warnicke, S. D. Pollard, D. A. Arena, and Y. Zhu, Nat. Commun. **5**, 3760 (2014).

[64] J. F. Pulecio, S. D. Pollard, P. Warnicke, D. A. Arena, and Y. Zhu, Appl. Phys. Lett. **105**, 132403 (2014).

[65] S. Rößler, S. Hankemeier, B. Krüger, F. Balhorn, R. Frömter, and H. P. Oepen, Phys. Rev. B **89**, 174426 (2014).

[66] S. D. Pollard, L. Huang, K. S. Buchanan, D. A. Arena, and Y. Zhu, Nat. Commun. **3**, 1028 (2012).

[67] R. L. Compton, T. Y. Chen, and P. A. Crowell, Phys. Rev. B **81**, 144412 (2010).

[68] R. Compton and P. Crowell, Phys. Rev. Lett. **97**, 2 (2006).

[69] S. Kasai, Y. Nakatani, K. Kobayashi, H. Kohno, and T. Ono, Phys. Rev. Lett. **97**, 107204 (2006).

[70] V. Novosad, F. Y. Fradin, P. E. Roy, K. S. Buchanan, K. Y. Guslienko, and S. D. Bader, Phys. Rev. B **72**, 24455 (2005).

[71] B. Krüger, A. Drews, M. Bolte, U. Merkt, D. Pfannkuche, and G. Meier, Phys. Rev. B **76**, 224426 (2007).

[72] B. Krüger, M. Najafi, S. Bohlens, R. Frömter, D. P. F. Möller, and D. Pfannkuche, Phys. Rev. Lett. **104**, 077201 (2010).

[73] A. Thiele, Phys. Rev. Lett. **30**, 230 (1973).

[74] A. Thiaville, J. Appl. Phys. **95**, 7049 (2004).

[75] S. Kasai, P. Fischer, M.-Y. Im, K. Yamada, Y. Nakatani, K. Kobayashi, H. Kohno, and T. Ono, Phys. Rev. Lett. **101**, 237203 (2008).

[76] M. Zhu, C. L. Dennis, and R. D. McMichael, Phys. Rev. B **81**, 140407 (2010).

[77] J.-Y. Chauleau, H. G. Bauer, H. S. Körner, J. Stigloher, M. Härtinger, G. Woltersdorf, and C. H. Back, Phys. Rev. B **89**, 020403 (2014).

[78] M. A. Ruderman and C. Kittel, Phys. Rev. **96**, 99 (1954).

[79] Y. M. Luo, C. Zhou, C. Won, and Y. Z. Wu, J. Appl. Phys. **116**, 213909 (2014).

[80] A. Vogel, T. Kamionka, M. Martens, A. Drews, K. W. Chou, T. Tyliszczak, H. Stoll, B. Van Waeyenberge, and G. Meier, Phys. Rev. Lett. **106**, 137201 (2011).

[81] J. Shibata, K. Shigeto, and Y. Otani, Phys. Rev. B **67**, 224404 (2003).

[82] S. Jain, V. Novosad, F. Y. Fradin, J. E. Pearson, V. Tiberkevich, A. N. Slavin, and S. D. Bader, Nat. Commun. **3**, 1330 (2012).

[83] S. Jain, H. Schultheiss, O. Heinonen, F. Y. Fradin, J. E. Pearson, S. D. Bader, and V. Novosad, Phys. Rev. B **86**, 214418 (2012).

[84] K. S. Buchanan, P. E. Roy, M. Grimsditch, F. Y. Fradin, K. Y. Guslienko, S. D. Bader, and V. Novosad, Nat. Phys. **1**, 172 (2005).

[85] K. S. Buchanan, P. E. Roy, M. Grimsditch, F. Y. Fradin, K. Y. Guslienko, S. D. Bader, and V. Novosad, Nat. Phys. **1**, 172 (2005).

[86] A. Bisig, J. Rhensius, M. Kammerer, M. Curcic, H. Stoll, G. Schütz, B. Van Waeyenberge, K. W. Chou, T. Tyliszczak, L. J. Heyderman, S. Krzyk, A. von Bieren, and M. Kläui, Appl. Phys. Lett. **96**, 152506 (2010).

[87] D. Bedau, M. Kläui, M. T. Hua, S. Krzyk, U. Rüdiger, G. Faini, and L. Vila, Phys. Rev. Lett. **101**, 256602 (2008).

[88] J. L. Hockel, S. D. Pollard, K. P. Wetzlar, T. Wu, Y. Zhu, and G. P. Carman, Appl. Phys. Lett. **102**, 242901 (2013).

[89] P. A. Midgley and R. E. Dunin-Borkowski, Nat. Mater. **8**, 271 (2009).

[90] C. Phatak, Y. Liu, E. B. Gulsoy, D. Schmidt, E. Franke-Schubert, and A. Petford-Long, Nano Lett. **14**, 759 (2014).

[91] J. S. Kim, T. Lagrange, B. W. Reed, M. L. Taheri, M. R. Armstrong, W. E. King, N. D. Browning, and G. H. Campbell, Science **321**, 1472 (2008).

[92] H. S. Park, J. S. Baskin, and A. H. Zewail, Nano Lett. **10**, 3796 (2010).

[93] P. Fischer, IEEE Trans. Magn. **51**, 1 (2015).